



Design of Porous Materials for Electrochemical Applications

Sunpet Assavapanumat

► To cite this version:

Sunpet Assavapanumat. Design of Porous Materials for Electrochemical Applications. Other. Université de Bordeaux; Vidyasirimedhi Institute of Science and Technology, 2020. English. NNT : 2020BORD0092 . tel-02982697

HAL Id: tel-02982697

<https://theses.hal.science/tel-02982697>

Submitted on 28 Oct 2020

HAL is a multi-disciplinary open access archive for the deposit and dissemination of scientific research documents, whether they are published or not. The documents may come from teaching and research institutions in France or abroad, or from public or private research centers.

L'archive ouverte pluridisciplinaire **HAL**, est destinée au dépôt et à la diffusion de documents scientifiques de niveau recherche, publiés ou non, émanant des établissements d'enseignement et de recherche français ou étrangers, des laboratoires publics ou privés.

THÈSE EN COTUTELLE PRÉSENTÉE

POUR OBTENIR LE GRADE DE

DOCTEUR DE

L'UNIVERSITÉ DE BORDEAUX

ET DU VIDYASIRIMEDHI INSTITUTE OF SCIENCE AND

TECHNOLOGY

ÉCOLE DOCTORALE SCIENCES CHIMIQUES

SPÉCIALITÉ : Chimie-Physique

Par Sunpet Assavapanumat

Design de Matériaux Poreux pour des Applications Électrochimiques

sous la direction de Prof. Dr. Alexander Kuhn
et de Asst. Prof. Dr. Chularat Wattanakit

Soutenue le : 10.08.2020

Membres du jury :

M. HAPIOT, Philippe

M. INAGI, Shinsuke

M. KUHN, Alexander

Mme. WATTANAKIT, Chularat

Mme. HANNONGBUA, Supa

M. FLOOD, Adrian Evan

Research director, Institute of Chemical Sciences Rennes

Associate Professor, Tokyo Institute of Technology

Professor, Institute des Sciences Moléculaire

Assistant Professor, Vidyasirimedhi Institute of Science and technology

Professor, Kasetsart University

Professor, Vidyasirimedhi Institute of Science and technology

Rapporteur

Rapporteur

Directeur de thèse

Directeur de thèse

Examineur

Examineur

Titre : Design de Matériaux Poreux pour des Applications Electrochimiques

Résumé : Le développement de matériaux poreux est l'un des sujets de recherche les plus fascinants notamment grâce à ces nombreuses applications allant de l'analyse chimique à la séparation et la catalyse. Parmi l'énorme quantité de matériaux poreux différents, les métaux nanoporeux sont le meilleur choix en raison de leurs propriétés intrinsèques telles qu'une grande surface active, un grand volume de pores et une grande accessibilité pour les molécules qui doivent diffuser au sein de la matrice où des sites catalytiquement actifs sont localisés. Afin de synthétiser de tels matériaux, une approche « template » est généralement utilisée pour générer des structures poreuses uniformes, y compris des « templates » durs et mous, qui dépendent de la forme de ces moules. Dans la présente thèse, l'élaboration de diverses électrodes métalliques poreuses via une approche de « template » souple et leurs applications potentielles dans le domaine de l'analyse énantiosélective, de la synthèse et de la séparation seront discutées. Plusieurs métaux à empreinte chirale seront présentés tels que le platine et le nickel dont la surface électroactive est significativement augmentée. Par la suite, ces métaux mésoporeux à empreinte chirale peuvent être utilisés pour améliorer les performances électrochimiques de différents systèmes allant de la synthèse électrochimique de composés chiraux à la séparation chirale ou encore des actionneurs, dont l'importance est grande pour des applications pharmaceutiques. La première partie du présent travail est consacrée à l'élaboration de métaux à empreinte chirale pour la synthèse asymétrique. Les surfaces actives du matériau d'électrode préparés présentent une sélectivité étonnamment élevée en terme de synthèse chirale lorsqu'elles sont combinées avec le concept d'électrochimie pulsée. La deuxième partie du manuscrit est consacrée à l'utilisation de composés naturels énantiomériquement purs pour faciliter la séparation des deux énantiomères d'un mélange racémique en appliquant un potentiel à la matrice métallique afin de contrôler les interactions électrostatiques entre les composés chiraux et les surfaces d'intérêt. Dans les conditions les plus appropriées, une séparation complète des deux énantiomères peut être observée. La troisième partie de cette thèse porte sur la détection chirale pour laquelle un film hybride de Pt imprimé chirale et de polypyrrole est utilisé comme actionneur sélectif dans des conditions d'électrochimie bipolaire. Les

propriétés synergiques des deux matériaux, l'activation sans fil et la reconnaissance chirale, ont été combinées avec succès pour l'analyse chirale sans fil.

Outre la conception et l'application de films métalliques chiraux mésoporeux, le dernier chapitre démontre l'élaboration de métaux structurés hiérarchiquement, contenant des caractéristiques macro et mésoporeuses, obtenus en utilisant simultanément des approches de « template » durs et mous pour l'électrocatalyse de la formation d'oxygène en milieu basique. Des nanofeuilles de nickel multiporeuses ont été préparées via un processus d'électrodéposition en deux étapes en présence de billes de silice et de surfactant comme moules pour contrôler respectivement la structure macro- et mésoporeuse. L'effet synergique résultant des cavités macroporeuses et mésoporeuses combinées permet un réglage fin des propriétés structurales, des performances électrocatalytiques et de la stabilité du matériau pour l'électrolyse de l'eau.

En conclusion, nos résultats ouvrent des perspectives intéressantes pour le développement de nouveaux matériaux poreux qui présentent un intérêt potentiel pour diverses applications, telles que l'analyse chirale, la synthèse asymétrique, la séparation chimique, ainsi que la conversion et le stockage d'énergie.

Mots clés : Impression moléculaire; Métaux mesoporeux; Reconnaissance chirale; Enantiosélectivité; Enantioaffinité; Porosité hiérarchique; Electrocatalyse

Title : Design of Porous Materials for Electrochemical Applications

Abstract : The development of porous materials has been one of the most fascinating research topics in the frame of a wide variety of applications ranging from chemical analysis to separation and catalysis. Among the huge amount of different porous materials, nanoporous metals are one of the most interesting candidates because of their outstanding properties such as a high surface area, a large pore volume and a high accessibility for guest molecules, which have to diffuse into the internal matrix where catalytically active sites are located. In order to synthesize such materials, a templating approach, including hard and soft templating is typically used

to generate uniform porous structures, depending on the shape of the templates. In the present dissertation thesis, the elaboration of various porous metal electrodes via a soft templating approach and their potential applications in the field of enantioselective analysis, synthesis and separation are discussed. Several chiral imprinted metals such as platinum and nickel with a significantly increased internal electroactive surface area are studied. Subsequently, these chiral imprinted mesoporous metals can be used to improve the electrochemical performance with respect to several tasks, including electrochemical synthesis of chiral compounds, chiral separation and actuation, which are important for pharmaceutical applications. The first part of the present work is devoted to the elaboration of chiral imprinted metals for asymmetric synthesis. The prepared electrode surfaces show a surprisingly high selectivity in terms of chiral synthesis when they are combined with the concept of pulsed electrochemistry. The second part of the manuscript is dedicated to their use for the separation of racemic mixtures with the opportunity to fine-tune the separation efficiency by applying a potential to the metal matrix in order to adjust the electrostatic interactions between the chiral compounds and the designer surfaces. Under the most suitable conditions, complete baseline separation of both enantiomers can be observed. The third part of this thesis deals with chiral detection, for which a hybrid film of chiral imprinted Pt and polypyrrole is used as a selective actuator under bipolar electrochemical conditions. The synergistic properties of both materials, wireless actuation and chiral recognition, have been successfully combined for wireless chiral analysis.

Apart from the design and application of chiral mesoporous metal films, the last chapter is dedicated to the elaboration of hierarchically structured metals containing macro- and mesoporous features, obtained by using simultaneously hard and soft templating approaches for electrocatalytic oxygen evolution in basic media. Multiporous nickel nanosheets were prepared via a two-step electrodeposition process in the presence of silica beads and surfactant as templates to control the macro- and mesoporous structure, respectively. The resulting synergistic effect of combined macroporous and mesoporous cavities allows fine tuning structural properties, electrocatalytic performance and stability for water splitting applications.

In conclusion, our findings open interesting perspectives for development of new porous materials, which are of potential interest for various applications, such as

chiral analysis, asymmetric synthesis, chemical separation, as well as energy conversion and storage.

Keywords : Molecular imprinting; Mesoporous metals; Chiral recognition; Enantioselectivity; Enantioaffinity; Hierarchical porosity; Electrocatalysis

Université de Bordeaux

Bordeaux INP, Site ENSCBP, 16 avenue Pey Berland 33607 France

Acknowledgements

First of all, I would like to express my sincere gratitude to Prof. Alexander Kuhn, my supervisor in France for his patience, motivation and immense knowledge. His guidance helped me during all the time of my research and writing of this thesis. Moreover, I would like to express my greatest gratitude and deepest appreciation to my co-supervisor, Asst. Prof. Dr. Chularat Wattanakit, for her valuable advice, support, discussion and precious opportunity to be a part of the AMPM group. I appreciate all she has done for me and the great attitude to drive the research forward. I would like to gratefully thank to the opportunity from both advisors to be part of Franco-Thai exchange program. In addition, I cannot find the words that can express the deepest respect to both supervisions. Without both supervisors, I would not be able to finish my Ph.D.

I would like to take this opportunity to thank also all members of the jury for having accepted to evaluate my thesis and for their useful comments and suggestions, particularly Prof. Dr. Adrian Evan Flood, Prof. Dr. Supa Hannongbua, Assoc. Prof. Dr. Shinsuke Inagi and Prof. Dr. Philippe Hapiot for accepting the invitation as examiners of this jury.

I appreciatively thank to Prof. Dr. Neso Sojic, who gave me the very nice suggestion to use the optical fiber-equipped microscope and Asst. Prof. Dr. Adeline Perro for advanced scientific support concerning the microfluidic device.

My special grateful thanks to Dr. Thitaya Yutthalekha, who taught me since I began the preparation process for chiral imprinted electrodes and the characterization with electrochemical techniques. Cheerful thanks to Dr. Anawat Thivasasith for kind suggestions and support for the activities on the campus. I gratefully thank Dr. Thidararat Imyen for game gambling to cheer me up during my time in VISTEC. I would like to specially thank Dr. Gerardo Salinas, Dr. Bhavana Gupta, Dr. Lin Zhang and Dr. Camille Colin for creating a good atmosphere in the NSysA's lab and all their advice. Special thanks to Alice Dauphin for being a funny person and kindly helping me to check the

French abstract and summary. My appreciation to Patrick Garrigue, Dr. Stéphane Reculosa, Dr. Bertrand Goudeau and Véronique Lapeyre for their skillful special support with respect to experimental setups and characterization techniques.

I would express thanks to all members in the laboratories in VISTEC, Thailand and France for all kind help, encouragement, and very nice atmosphere, deserved as a importance factor for my Ph.D. thesis, especially, Dr. Saros Salakhum and Sirawit Shetsiri, who are one of my best friends. In addition, I would like to warmly thank to Marisa Ketkaew and Sopon Butcha for their great support and nice contributions in this thesis.

I would like to acknowledge the financial support and characterization equipment from Vidyasirimedhi Institute of Science and Technology (VISTEC). In addition, the nice experience in France was supported by Campus France and the French Embassy in Thailand with a Ph.D. cotutelle scholarship in 2016. Many thanks go also to the permanent staff and scientists in VISTEC and NSysA, who hearty helped for training how to use the instruments, setting-up the experiments and discussing the results. All this work would not have been possible without the support from the bilateral PICS program of CNRS, Thailand Research Fund (TRF) (MRG6180099), the Office of Higher Education Commission (OHEC) and TTSTF research project supported by Thailand Toray Science Foundation. In addition, this work has been partially supported by the National Nanotechnology Center (NANOTEC), NSTDA, Ministry of Science and Technology, Thailand, through its program of Research Network NANOTEC (RNN). S.A. is grateful to Campus France, the French Embassy in Thailand, and VISTEC. The project has also been partially funded by the European Research Council (ERC) under the European Union's Horizon 2020 research and innovation program (grant agreement no. 741251, ERC Advanced Grant ELECTRA).

Last but not least, I would like to especially recognize my parents and my brothers for true love, great support, warm caring and their kind teaching of life. Their devotion is endless and invaluable.

Without all the people mentioned above, I would not have been able to achieve this big step of my life.

Sunpet Assavapanumat

10 August 2020

Contents

	Page
Abstract	i
Acknowledgement	v
List of Tables	xii
List of Figures	xiii
List of Schemes	xxv
List of Abbreviations	xxviii
General introduction	1
I. Design of mesoporous metals	1
<i>I.I Fundamentals of the soft templating approach</i>	4
<i>I.II Development of mesoporous metals via the soft templating approach</i>	8
<i>I.III Chiral imprinted mesoporous metals</i>	14
II Design of macroporous metals	16
<i>II.I Fundamentals of the hard templating approach</i>	17
<i>II.II Langmuir-Blodgett technique</i>	19
III Multiporous metals	20
Chapter 1 Highly enantioselective synthesis of chiral compounds on chiral encoded mesoporous metals surfaces	26
1.1 Introduction	26
1.2 Experimental section	38
<i>Chemicals</i>	38
<i>Substrate-cleaning</i>	38
<i>Electrodeposition of chiral imprinted mesoporous platinum</i>	38
<i>Electrodeposition of chiral encoded mesoporous nickel</i>	39
<i>Electrode characterization</i>	40

Contents (Cont.)

	Page
<i>Enantioselective electrosynthesis of chiral compounds</i>	40
1.3 Results and discussion	41
<i>Characterization</i>	41
<i>Enantioselective recognition of chiral compounds at chiral imprinted mesoporous metals surfaces</i>	49
<i>Asymmetric synthesis of chiral compounds at chiral imprinted mesoporous metal surfaces</i>	50
1.4 Conclusion	58
Chapter 2 Electrochemically fine-tuning of the enantioaffinity of chiral imprinted platinum surfaces for chiral discrimination and separation	58
2.1 Introduction	59
2.2 Experimental section	62
<i>Chemicals</i>	62
<i>Gold-coated glass substrate cleaning</i>	63
<i>Electrodeposition of chiral imprinted mesoporous platinum microchannels</i>	63
<i>Electrode characterization</i>	64
<i>Potential tuning on chiral imprinted platinum surfaces for chiral separation</i>	64
2.3 Results and Discussion	65
<i>Characterization of chiral encoded mesoporous platinum films</i>	65
<i>Enantioselective recognition of chiral compound at chiral imprinted mesoporous metals surfaces</i>	69
<i>Chiral discrimination and separation</i>	72

Contents (Cont.)

	Page
2.4 Conclusion	79
Chapter 3 Advanced design of chiral imprinted platinum-polypyrrole hybrid films for enantioselective actuators of mandelic acid	81
3.1 Introduction	79
3.2 Experimental section	85
<i>Chemicals</i>	85
<i>Gold-coated glass substrate cleaning</i>	85
<i>Chiral encoded mesoporous platinum using mandelic acid as a template</i>	85
<i>Hybrid PPy-chiral platinum</i>	86
<i>Electrode characterization</i>	86
<i>Enantioselective actuator</i>	87
3.3 Results and Discussion	87
<i>Chiral encoded mesoporous platinum characterization</i>	89
<i>Chiral actuator</i>	91
3.4 Conclusion	95
Chapter 4 Hierarchical macro- and mesoporous nickel nanosheets for oxygen evolution reaction	97
4.1 Introduction	97
4.2 Experimental section	101
<i>Chemicals</i>	101
<i>Mesoporous nickel nanosheets (Meso-Ni) deposition</i>	101
<i>Macroporous nickel (Macro-Ni) deposition</i>	101
<i>Hierarchical macro- and mesoporous nickel nanosheets (Hi-Ni) deposition</i>	102
<i>Electrochemical characterization</i>	102

Contents (Cont.)

	Page
<i>Surfactant assembly study</i>	103
4.3 Results and Discussion	103
<i>Electrode fabrication</i>	103
<i>Porous electrode characterization</i>	106
<i>Electrocatalytic oxygen evolution reaction (OER)</i>	113
4.4 Conclusion	120
Chapter 5. Thesis Perspectives	121
Resumé	125
Summary	129
References	133
Author's Biography	157

List of Tables

Table		Page
4.1	Experimental and theoretical roughness factor of various fresh and used nickel electrodes taken before and after performing OER at different applied potentials.	111
4.2	OER onset potentials and corresponding Tafel slopes of various nickel electrodes measured by LSV in N ₂ saturated 1 M KOH electrolyte at a scan rate of 5 mVs ⁻¹ .	115

List of Figures

Figure		Page
i.i	Synthetic approaches for generating mesoporous metals via a) soft-templating and b) hard-templating. The image is adapted from Ref [17].	3
i.ii	Phase diagram for binary systems (Brij56+water). Phase notation: S-solid, L ₁ -micellar solution, I ₁ -micellar cubic phase, H ₁ -hexagonal phase, V ₁ -cubic phase, L _α -lamellar phase and L ₂ -inverse micellar solution. The image is reproduced from Ref [19].	5
i.iii	Mechanisms using soft templates to obtain mesoporous metals via cooperative assembly (top) and liquid crystal templating (bottom) taken from Ref. [23].	7
i.iv	Illustration of the surface morphology and mesoporous structure of Ni particles prepared using a) and c) Sodium borohydride (SBH); b) and d) Dimethylamineborane (DMAB). Images were taken from Ref [30]	10
i.v	Schematic illustration of the formation steps of evaporation-induced self-assembly. The image is taken from Ref. [23]	13
i.vi	Preparation scheme of chiral imprinted mesoporous platinum on a gold substrate. a) self-assembly of a lyotropic liquid crystal and chiral templates, b) electrodeposition of platinum covering the lyotropic liquid crystal and chiral molecules, c) obtained final chiral cavities after template and surfactant removal, taken from [2].	16
i.vii	Preparation scheme of porous materials via hard templating, taken from Ref [23].	17

List of Figures (Cont.)

Figure		Page
i.viii	Illustration of substrate coating via Langmuir-Blodgett (LB) technique: (a) molecular structure of an amphiphilic molecule, (b) LB film preparation, (c) surface pressure of LB film during compression and (d) multilayer coating of a substrate. The images are taken from Ref [55].	20
i.ix	SEM characterization of multiporous Cu after selective dealloying: (a) SEM image with 1 μm of scale bar and (b) high magnification SEM image with 200 nm scale bar. The images were taken from Ref [58].	21
i.x	Illustration of hierarchical porous material preparation demonstrating a combination of hard and soft templating methods, taken from Ref [23].	23
i.xi	Illustration of preparation steps of multiporous Pt electrodes obtained by combining hard and soft templating approaches, taken from [42].	24
1.1	Adsorption phase diagram of <i>R,R</i> tartaric acid on 2-dimensionally anisotropic Cu(110) surfaces as a function of temperature and coverage. Taken from Ref [74]	28
1.2	Orito-type reactions, taken from Ref [91]	29
1.3	a) Ball model of a) fcc(531) and fcc(463), taken from Ref [94]	31
1.4	Structure prediction of Au_5 with various possible configurations, depicted from Ref [95]	32
1.5	Interaction between the chiral template and Brij C10. a) L-DOPA (I), the oxidized form of L-DOPA (II), and the Brij C10 (III). b) The illustration of a column of aggregated Brij C10, depicted from [2].	35

List of Figures (Cont.)

Figure		Page
1.6	Synthesis scheme of mandelic acid: a) hydrogenation of phenyl glyoxylic acid (PGA) to chiral mandelic acid (MA), (b) R-MA chiral cavity, (c) S-MA chiral cavity, (d) adsorption of PGA in R-MA cavity and (e) selective electroreduction of PGA to R-MA, taken from Ref [3]	37
1.7	Structural characterization of chiral imprinted mesoporous platinum electrodes: a) and b) cross section SEM images of chiral imprinted platinum electrodes with injected charge densities of 2 and 8 C cm ⁻² , scale bar of 10 μm. The insert illustrates the mesoporous structure of the platinum matrix, scale bar of 20 nm; (c) thickness of the platinum film as a function of the deposition charge density and (d) cyclic voltammetry of flat platinum (red) and a chiral-encoded mesoporous platinum film with an injected charge density of 8 C cm ⁻² (blue) in 0.5 M H ₂ SO ₄ at a scan rate of 100 mVs ⁻¹ ; H _a (hydrogen adsorption) and H _d (hydrogen desorption).	44
1.8	Cyclic voltammograms of non-imprinted mesoporous platinum (blue) and chiral imprinted mesoporous platinum (black) obtained with a deposition charge density of 8 Ccm ⁻² , recorded in 0.5 M H ₂ SO ₄ at a scan rate of 100 mVs ⁻¹ in the range from -0.25 to 1.25 V vs Ag/AgCl.	45

List of Figures (Cont.)

Figure		Page
1.9	Structural characterization of chiral imprinted mesoporous nickel electrodes: a) and b) top view and cross section SEM images of a chiral imprinted nickel electrode with an injected charge density of 4 C cm^{-2} , scale bar of $10 \text{ }\mu\text{m}$ and $1 \text{ }\mu\text{m}$, respectively; the insert illustrates the mesoporous structure of the nickel matrix, scale bar of 50 nm ; (c) relative surface area and thickness of nickel film as a function of the deposition charge density and (d) cyclic voltammograms of flat nickel and chiral-encoded mesoporous nickel films with various charge densities in 1 M KOH at a scan rate of 100 mVs^{-1} .	46
1.10	SEM images of mesoporous nickel electrodes imprinted with S-PE obtained with various injected charge densities: (a-b) 1 C cm^{-2} ; (c-d) 2 C cm^{-2} with a scale bar of $10 \text{ }\mu\text{m}$ (top view) and $1 \text{ }\mu\text{m}$ (cross-section).	47
1.11	Investigating template removal of the prepared electrodes; a) and b) absorption spectra of the washing solutions when cleaning chiral platinum and nickel electrodes, respectively and c) different pulse voltammetry (DPV) of the cleaned electrode in pure supporting electrolyte (red curve) compared to a non-imprinted electrode (black curve) and an electrode in S-PE solution (blue curve).	48
1.12	DPV of electrooxidation of (R)-phenyl ethanol (red) and (S)-phenyl ethanol (blue) in 50 mM HCl as a supporting electrolyte with different electrodes: a) non-encoded mesoporous platinum; b) and c) chiral mesoporous platinum encoded with (R)-PE and (S)-PE, respectively. All electrodes were prepared using a charge density of 2 Ccm^{-2} and a PE/PtCl_6^{2-} ratio of 0.05 for encoding the electrode.	49

List of Figures (Cont.)

Figure		Page
1.13	DPV of electrooxidation of (R)-phenyl ethanol and (S)-phenyl ethanol in 50 mM HCl supporting electrolyte with different electrodes: a) non-encoded mesoporous nickel; b) and c) chiral mesoporous nickel encoded with (S)-PE and (R)-PE, respectively.	50
1.14	Cyclic voltammograms of flat electrodes obtained at a scan rate of 100 mVs ⁻¹ under various conditions: a) flat platinum electrode in 1 M NH ₄ Cl (black) and 43 mM acetophenone (blue); b) flat nickel electrode in 1 M NH ₄ Cl (red) and 10 mM acetophenone (blue).	53
1.15	Standard chromatograms of the prochiral acetophenone (black), and the products (R)-PE (red) and (S)-PE (blue).	54
1.16	Results of the asymmetric synthesis when using chiral imprinted platinum electrodes: a) HPLC chromatograms of the electrosynthesis products obtained with (S)-PE imprinted electrodes in 10 mM acetophenone and 1 M NH ₄ Cl at a potential -0.45 V vs Ag/AgCl for different pulse durations. The peak retention times of 13.5 and 14.5 min correspond to (R)-PE and (S)-PE, respectively. b) Histogram summarizing the enantiomeric excess (%ee) for various pulse times. Colour codes present the different conditions of enantiomeric synthesis: classic electrosynthesis (orange); 60s pulses (pink) 30s pulses (red); 10s pulses (blue) 2s pulses (black).	55

List of Figures (Cont.)

Figure		Page
1.17	Circular dichroism (CD) spectra of the products obtained from electroreduction of acetophenone using a mesoporous platinum matrix imprinted with (R)-PE (blue) and (S)-PE (red) for a pulse time of 5s.	55
1.18	Chiral synthesis using chiral imprinted nickel as working electrode: a) and b) HPLC chromatograms of electrosynthesis products from 10 mM acetophenone and 1 M NH ₄ Cl as a supporting electrolyte with (a) a constant applied potential of -0.55 V vs Ag/AgCl and (b) potential pulses	56
1.19	Mechanical stability of chiral encoded mesoporous nickel electrodes in supporting electrolyte with and without an applied potential of – 0.55 V vs Ag/AgCl.	58
2.1	a) and b) SEM images of L-Trp encoded mesoporous platinum deposited with 8 Ccm ⁻² as top view and cross section, respectively; scale bars are 100 and 20 μm. c) TEM image of the platinum film; scale bar 50 nm. d) Cyclic voltammograms of various platinum electrodes in 0.5M H ₂ SO ₄ at 100 mVs ⁻¹ in the range of -0.25 to 1.25 V vs. Ag/AgCl. Key: flat platinum (red) and Trp-encoded mesoporous platinum, deposited with a charge of 2 (green), 4 (blue), and 8 Ccm ⁻² (purple).	67
2.2	Surface enhancement factor and deposit thickness as a function of injected charge density during the electrodeposition of the mesoporous metal.	68
2.3	Absorption spectra of supernatant during the washing process after 30 (red) min and 60 min (green).	69

List of Figures (Cont.)

Figure		Page
2.4	Differential pulse voltammetry (DPV) of various platinum electrodes in 4 mM L-Trp (red) and D-Trp (blue) using 50 mM HCL as supporting electrolyte (green is measured in supporting electrolyte only); (a) a flat platinum electrode, (b) L-Trp encoded mesoporous platinum, (c) D-Trp encoded mesoporous platinum and (d) L-Trp encoded mesoporous platinum after erasing the chirality by running a CV in 0.5 M H ₂ SO ₄ between -0.25 and 1.25 V vs Ag/AgCl.	70
2.5	Differential pulse voltammetry (DPV) of various platinum electrodes in 4 mM L-DOPA (red) and D-DOPA (blue) using 50 mM HCL as supporting electrolyte; (a) a flat platinum electrode, (b) L-Trp encoded mesoporous platinum, (c) D-Trp encoded mesoporous platinum and (d) L-Trp encoded mesoporous platinum after erasing the chirality by running a CV in 0.5M H ₂ SO ₄ between -0.25 and 1.25 V vs Ag/AgCl.	71
2.6	(a) Electrodeposition of a narrow strip of tryptophan encoded mesoporous platinum on a gold-coated glass. (b) Two plates prepared in this way are placed face to face and kept separated at a distance of 65 μm by positioning double sided tape along both sides of the metal deposit. This also allows to seal the channel. (c) Global view of the final microfluidic device for chiral separation.	74
2.7	Absorption and fluorescence spectra of 1 mM tryptophan dissolved in water.	75

List of Figures (Cont.)

Figure		Page
2.8	Electrochromatography of racemate Trp solutions with fluorescence detection at the microchannel outlet by an optical fiber for a L-Trp imprinted platinum layer. a) No applied potential; (b) 200 mV vs Ag; and (c) 300 mV (fresh).	76
2.9	Electrochromatography of racemic Trp solutions with fluorescence detection at the microchannel outlet by an optical fiber for a L-Trp imprinted platinum layer. a) D-Trp; and b) L-Trp.	77
2.10	Electrochromatography of racemic Trp solutions with fluorescence detection at the microchannel outlet by an optical fiber for a L-Trp imprinted platinum layer. a) freshly prepared layer of chiral platinum film; and b) after 1 month.	77
2.11	Record of the fluorescence signal at the microchannel outlet during tyrosine separation with a) no potential and b) +300 mV vs Ag applied to the L-Trp imprinted mesoporous platinum.	78
2.12	Separation of Naproxen enantiomers on an L-Trp-encoded platinum film at a) no applied potential b) +300 mV and c) +400 mV vs. Ag	79
3.1	SEM images of the hybrid chiral imprinted Pt–PPy film at different positions. (a and d) top and side view of the chiral-encoded platinum layer, (b and e) top and side view of the Pt–PPy junction (inset: EDS map), (c and f) top and side view of the PPy film.	90
3.2	SEM image of the bottom face of the free-standing hybrid Pt–PPy material.	91

List of Figures (Cont.)

Figure		Page
3.3	Differential pulse voltammetry of R-MA imprinted Pt-PPy in 50 mM R-MA (blue) and S-MA (red) using 50 mM HCl as supporting electrolyte.	92
3.4	(a) Bending as a function of time for non-imprinted Pt-PPy in 50 mM R-MA (blue) and S-MA (red) using 50 mM HCl as supporting electrolyte. (b) Images of non-imprinted hybrid PPy-Pt during chiral analysis in R-MA (top) and S-MA (bottom) at the beginning (green) and after 15 min (red).	93
3.5	Bipolar electrochemical actuation of hybrid chiral Pt-PPy in 50 mM R-MA (blue) and S-MA (red) using 50 mM HCl as supporting electrolyte. Relative bending measured as a function of time for (a) R-MA imprinted Pt-PPy and (b) S-MA imprinted Pt-PPy. The pictures on the right have been taken after 6 min of applied potential. The green line indicates the initial position of the actuator, whereas red corresponds to its final position.	95
4.1	SEM image of a substrate coated with silica beads by using the Langmuir-Blodgett technique.	105
4.2	Chronoamperometric curve recorded during potentiostatic nickel electrodeposition through the first five half-layers of the colloidal silica-bead template (particle size of 920 nm diameter).	105

List of Figures (Cont.)

Figure		Page
4.3	Scanning electron microscope (SEM) images of Macro-Ni obtained by the electroreduction of nickel salt in the void space of three half-layers of the colloidal silica template composed of beads with a diameter of about 920 nm (a: top view, scale bar 1 μm ; b: top view, scale bar 100 nm; c: cross section, scale bar 10 μm); Meso-Ni obtained by electrodepositing nickel with a charge of 5 C cm^{-2} (d: low magnification, scale bar 100 nm; e: high magnification, scale bar 100 nm; f: cross section, scale bar 10 μm); Hi-Ni obtained by the electrodeposition of Meso-Ni inside the macropores (920 nm diameter) with a thickness of three half-layers (g: top view, scale bar 1 μm ; h: top view, scale bar 100 nm; i: cross section, scale bar 10 μm).	107
4.4	Chronoamperometric curve at a constant potential of -0.1V (vs Ag/AgCl) in 0.5 M NaCl supporting electrolyte to evaluate the surface coverage of self-assembled surfactant on the electrodes obtained by applying different deposition potentials: 0.1 V (orange), 0V (green), -0.25V (blue), -0.75 V (brown) and bare Au electrode (red).	108
4.5	EDS mapping of Hi-Ni: Red spots indicate the nickel distribution on the prepared electrode in and around one macropore.	109
4.6	Thin film X-ray diffraction patterns of Macro-Ni (blue), Meso-Ni (red) and Hi-Ni (black) having a comparable film thickness of 1.2, 1.3 and 1.4 μm , respectively.	110

List of Figures (Cont.)

Figure		Page
4.7	(a) Cyclic voltammograms of a three half-layer hierarchical nickel electrode (Hi-Ni) measured in N ₂ -saturated 1 M KOH with varying scan rates in the range of 0 to 100 mV s ⁻¹ . (b) Plot of capacitance current density as a function of scan rate in order to determine the electroactive surface.	111
4.8	Roughness factor as a function of film thickness of Hi-Ni.	113
4.9	Linear sweep voltammogram (LSVs) for various nickel electrodes measured in N ₂ -saturated 1 M KOH electrolyte at a scan rate of 5 mVs ⁻¹ ; (a) Effect of the types of nickel electrodes on OER activity: flat Ni (red), Meso-Ni (blue), three half-layer Macro-Ni (yellow), and three half-layer Hi-Ni (green); (b) Effect of the number of electrodeposited macroporous layers on OER activity: one half-layer Hi-Ni (orange), three half-layer Hi-Ni (green), and five half-layer Hi-Ni (black).	115
4.10	Tafel plots measured in N ₂ -saturated 1 M KOH solutions calculated from LSVs for (a) various types of nickel electrodes; Meso-Ni (blue), three-half layer Macro-Ni (yellow), and three half-layer Hi-Ni (green), (b) various Hi-Ni electrodes prepared with different number of deposited half-layers; one half-layer Hi-Ni (orange), three half-layer Hi-Ni (green), five half-layer Hi-Ni (black).	117

List of Figures (Cont.)

Figure		Page
4.11	Chronoamperometry in 1 M KOH with various nickel electrodes at two different applied potentials; (a, b) Effect of the type of nickel on the electrocatalytic activity and stability, flat Ni (red); mesoporous Ni (blue); macroporous Ni (yellow) and hierarchical porous Ni (green) at an applied potential of 1.52 and 1.72 V (vs RHE), respectively. (c, d) Effect of the number of the deposited layers of hierarchical porous Ni on the electrocatalytic activity and stability; one half-layer (orange), three-half layer (green) and five-half layer (black) at a potential of 1.52 mV and 1.72 (vs Ag/AgCl), respectively	119
4.12	Surface morphology comparison of Meso-Ni at a) before and b) after catalytic testing.	120

List of Schemes

Scheme		Page
i.i	Illustration of the formation of platinum nanotubes prepared by various amphiphilic templating systems: A) Mixed C ₁₂ EO ₉ and Tween 60; B) single C ₁₂ EO ₉ surfactant forming cylindrical rod-like micelles; C) Possible pathway for the formation of metal nanotubes by the reduction of metals salts confined in the aqueous shell of mixed-surfactant cylindrical micelles. Image was taken from Ref [30].	9
1.1	Illustration of chiral imprinted mesoporous nickel film formation: a) the molecular structure of (R) and (S) phenylethanol; (b) the self-assembly of the lyotropic liquid crystal in the presence of Ni salt; (c) Ni electrodeposition in the presence of mesoporous template and chiral template; (d) the chiral imprinted mesoporous nickel after template removal.	42
1.2	Electrosynthesis of enantiomeric phenyl ethanol via hydrogenation of acetophenone: a) adsorption of the prochiral precursor in the imprinted cavity; b) selective hydrogenation of acetophenone inside the chiral cavity; c) chiral product obtained after hydrogenation; d) molecular desorption of phenylethanol from the cavity.	51
1.3	Comparison of the two strategies of enantiomeric synthesis. The prochiral precursor (yellow dots) enters the metal matrix and react with hydrogen (green dots). The products obtained from the electrosynthesis are (S)-PE (red dots) and (R)-PE (blue dots).	52

List of Schemes (Cont.)

Scheme	Page
2.1 Tryptophan-encoded mesoporous platinum preparation starting from the self-assembled lyotropic liquid crystal (red columns) interacting with chiral template on gold coated glass. Then platinum is electrodeposited through the template and in the last step the chiral template and surfactant are completely removed, leading to imprinted mesopores.	65
2.2 An illustration of the electrostatic interaction of deprotonated Trp with a cavity in a positively charged mesopore of the microchannel.	73
2.3 A hyphenated microfluidic electrochromatography device with an L-Trp-encoded mesoporous platinum film as a stationary phase. The electrochemical potential of the stationary phase is controlled by a potentiostat.	73
3.1 Preparation of a hybrid chiral Pt-PPy film a) gold substrate; b) chiral-imprinted Pt partially covering the gold coated glass slide; c) hybrid film on gold substrate; d) freestanding hybrid film after etching of the gold layer; e) tailored final geometry of the actuator f) enantioselective actuator mounted on a rubber support.	87
3.2 Illustration of the hybrid Pt-PPy film used for chiral recognition (a) Top view and (b) cross section of Pt-PPy (c) scheme of the bipolar electrochemical cell for chiral recognition of mandelic acid with the hybrid actuator.	89

List of Schemes (Cont.)

Scheme		Page
4.1	Schematic illustration of the synthesis of hierarchical macro- and mesoporous nickel deposited on a gold-coated glass slide using a colloidal crystal template: a) transfer of individual layers of silica beads onto the substrate by the LB technique; b) final silica beads template; c) electrodeposition of nickel; d) silica bead dissolution leads to Macro-Ni; e) electrodeposition of a mesoporous nickel film on the internal surface of Macro-Ni using a surfactant assembly as a template; f) Hi-Ni after the washing step.	104

List of Abbreviations

Symbols	Description
ACE	Acetophenone
Ag/AgCl	Silver/Silverchloride
atm	Atmospheric
CA	Cooperative assembly
CE	Counter electrode
CEMMS	Chiral encoded mesoporous metal surface
CMC	Critical micelle
CPP	Critical packing parameter
CV	Cyclic voltammetry
DOPA	3,4-dihydroxy phenylalanine
DPV	Different pulse voltammetry
e ⁻	Electron
EDS	Electron diffraction spectroscopy
%ee	Eanantiomeric excess
EISA	Evaporation induced self-assembly
EPC	Enantiomerically pure compound
g	Gram (s)
GC	Gas chromatography
h	Hour (s)
H ⁺	Proton
HER	Hydrogen evolution reaction
HPLC	High-performance liquid chromatography
K	Kelvin
LB	Langmuir-Blodgett
LCT	Liquid crystal templating
LIBs	Lithium ion batteries

List of Abbreviations (Cont.)

LLC	Lyotropic liquid crystal
LSV	Linear sweep voltammetry
μm	Micrometer
MA	Mandelic acid
MIP	Molecular imprinting polymer
MIT	Molecular imprinting technique
ml	Milliliter
MOF	Metal organic framework
nm	Nanometer
OER	Oxygen evolution reaction
ORR	Oxygen reduction reaction
PBUs	Primary building unit
PE	Phenyl ethanol
PGA	Phenyl glyoxylic acid
PPy	Polypyrrole
RE	Reference electrode
SBUs	Secondary building unit
SCs	Supercapacitors
SDAs	Structure directing agents
SEM	Scanning electron microscope
TEM	Transmission electron microscope
Trp	Tryptophan
vs	Versus
WE	Working electrode
XRD	X-ray diffraction

General Introduction

The development of porous materials is one of the most fascinating research topics for a wide range of applications, such as chemical analysis, separation technologies and catalysis. According to the classification of porous materials defined by IUPAC, they can be divided into three main categories depending on their pore size (diameter, d) namely microporous ($d < 2\text{nm}$), mesoporous ($2\text{ nm} < d < 50\text{ nm}$), and macroporous structures ($d > 50\text{nm}$). A very large variety of synthetic methods have been explored to synthesize porous materials. However, the lack of precisely controllable structures, their sometimes poor physical and chemical properties and instability can constitute main drawbacks.[8] Among various porous materials, porous metals are very attractive, because they provide high surface area, large pore volume and high accessibility of guest molecules to catalytically active metal sites.[9] Porous metals have been used for a wide range of potential applications, for instance electronic devices, magnetic recording media and metal catalysis. As mentioned above, there are several levels of porous metals including microporous, mesoporous and macroporous matrices. Among them, microporous structures often suffer from mass transport limitations inside the porous structures. To overcome this limitation, meso- and macroporous metals have been increasingly investigated for the advanced design of surface structures. Details concerning the preparation of such materials are explained in the following.

I. Design of mesoporous metals

Mesoporous metals refer to porous materials with a pore size in the range from 2 to 50 nm. As highlighted by the increase of publication numbers referring to the design of mesoporous metals, ordered mesoporous structures play an important role for a wide range of applications, such as chemical adsorption,[10] membranes,[11] energy conversion,[12] energy storage,[13] and especially catalysis because of their excellent physical properties including large specific

surface areas, a well-defined porous structure at the nanoscale, and high stability.[3] Due to these remarkable benefits of a mesoporous framework, the preparation of mesoporous metals has been extensively developed over the past decades, aiming to explore new structures and fine-tune their performance.

One of the popular approaches of mesoporous metal preparation is metal dealloying, which has been widely used to generate a mesoporous framework due to a simple manufacturing process.[14] In this case, many factors including the strategy for metal-removal (chemical and electrochemical leaching), operating temperature, concentration of solvent or supporting electrolyte and alloy composition, have been studied to control the structure of the final mesoporous metal. For example, in 2014 mesoporous Ni was successfully prepared via a one-step chemical/electrochemical dealloying of Ni combined with Mn using different conditions.[15] During the chemical dealloying process, the $\text{Ni}_{30}\text{Mn}_{70}$ alloy could be dissolved at room temperature in a weakly acidic solution. However, the dealloying process is very slow and a large amount of Mn still remains in the mesoporous alloy. In order to enhance the dissolution rate of Mn, the dealloying temperature was increased, resulting in the significant enhancement of the surface diffusivity of Ni adatoms and dissolution rate of Mn, and it subsequently promotes the formation of mesoporous Ni. However, the high dealloying temperatures also lead to the dissolution of Ni, resulting in a damage of the porous structures. Therefore, electrochemical dissolution was used as an alternative method for the selective dissolution of elements in bimetals by controlling the oxidation potential. In an electrochemical process, the applied potential can enhance the dissolution of Mn and interfacial diffusion of Ni for a rapid formation of mesoporous Ni. However, too high applied potentials can also lead to the dissolution of Ni, eventually resulting in the formation of cracked porous structures. Due to these intrinsic problems of the dealloying approach, a templating strategy can be used as an alternative strategy to generate mesoporous structures with a controllable pore diameter, structure and morphology.

Templating is used for generating bulk materials with the inverse structure of the original template. Generally, it can be divided into two major families: (i) soft template approach; (ii) hard template approach. Concerning the first one, amphiphilic molecules have been used to form a co-assembly of surfactant molecules and metal ions, leading to an ordered mesoporous structure after the removal of the template as shown in [Figure i.ia](#). This method has become a general synthetic pathway for producing ordered mesoporous metals because the structure can be easily controlled by concentration, temperature and molecular structure of the template molecules.

Concerning the hard-templating route, it is also known as “nanocasting”, which is another straightforward technique to obtain mesoporous structures. This technique is based on the use of solid templates, for instance carbon, anodic aluminium oxide and mesoporous silica nanoparticles ([Figure i.ib](#)) [16]. This approach has been used to prepare a wide range of materials, in particular highly crystalline and even single-crystal materials due to the resistance of the rigid template to high temperatures. The nanocasting pathway with hard templates opens up perspectives for the design of highly ordered porous materials with multifunctional composition, which are very difficult to obtain by a soft-templating approach

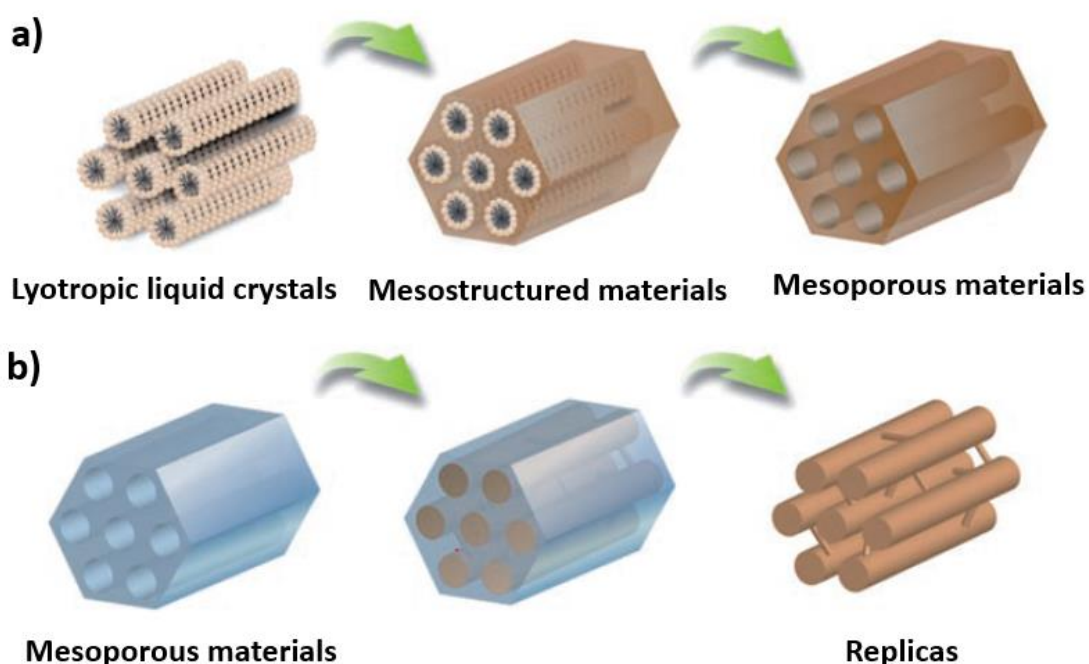


Figure i.i Synthetic approaches for generating mesoporous metals via a) soft-templating and b) hard-templating. The image is adapted from Ref [17].

However, the hard-template approach is considered as a more complex, expensive and industrially unfeasible method. Therefore, in order to circumvent these limitations of hard-templating, soft templating is often preferable and plays an important role in preparing mesoporous metals.

I.I Fundamentals of the soft templating approach

A soft-templating approach usually employs amphiphilic molecules, composed of hydrophilic and hydrophobic domains, forming self-assembled structures like micelles or lyotropic liquid crystals. Theoretically, the characteristics of amphiphilic molecules depend on their critical micelle concentration (CMC), which directly relates to the concentration of amphiphilic molecules, operating temperature and type of surfactant.[18] When the concentration of surfactant is at the CMC or above, it allows the surfactant to form a micellar structure, and when further increasing the concentration of amphiphilic molecules, a lyotropic liquid crystal (LLC) can be obtained. For example, in the case of Brij 56, when increasing the surfactant concentration above the CMC, the self-assembly of the LLC mesostructures is changing continuously from a micellar solution (L_1) through micellar cubic (I_1), hexagonal (H_1), bicontinuous cubic (V_1), lamellar (L_α), to inverse micellar (L_2) phases as illustrated in [Figure i.ii](#). In addition, the operating temperature is one of the most important parameters to generate micelles, and the self-assembly of surfactant doesn't occur if the temperature is below the Krafft point, because the surfactant can't dissolve under these conditions.

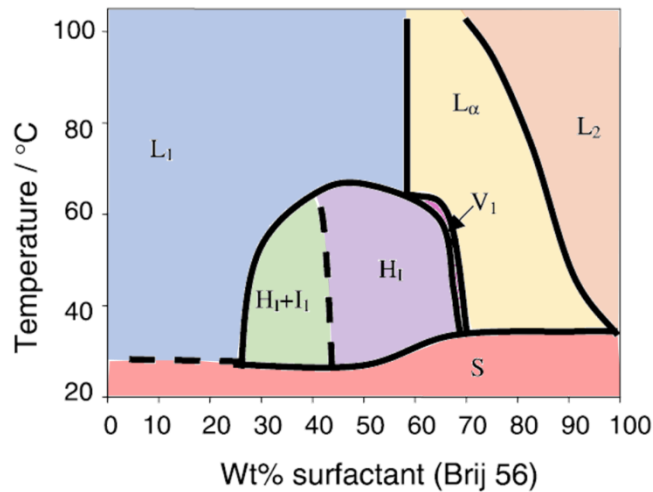


Figure i.ii Phase diagram for binary systems (Brij56+water). Phase notation: S-solid, L₁-micellar solution, I₁-micellar cubic phase, H₁-hexagonal phase, V₁-cubic phase, L_α-lamellar phase and L₂-inverse micellar solution. The image is reproduced from Ref [19].

The last key factor is the type of surfactant, which is defined by the polar head group. The corresponding four categories are cationic, anionic, non-ionic and amphoteric surfactants. These three most important factors, concentration, temperature and type of surfactant need to be optimized in order to form a well-defined mesoporous template.

The formation of a micelle/liquid crystalline phase is classically achieved by one of the four following approaches: (i) cooperative assembly (CA), (ii) true liquid crystal templating (LCT), (iii) evaporation-induced self-assembly (EISA), and (iv) evaporation-mediated direct template (EDIT) as shown in [Figure i.iii](#) and [i.v](#). Typically, the self-assembly of amphiphilic molecules is obtained by cooperative assembly (CA), which requires high temperatures to generate a micellar structure as shown in [Figure i.iiia](#). In the first step, a cluster of self-assembly is created via electrostatic interaction between the ionic surfactant and hydrolyzed sol-gel precursor.[20, 21] Subsequently, the assembled mesoporous structure is formed, and then hydrothermal synthesis is used to build the mesoporous material around the self-assembled mesostructures. After the template removal by washing or calcination, mesopores with a well-defined

structure are observed. However, it is essential that the interactions between the mesopore template and the matrix need to be considered, because if the mesoporous template is in the inappropriate condition, the precipitation of untemplated precursor may occur, or a disordered mesostructure can be formed.[20]

In order to overcome the above-mentioned problem, LCT has been chosen as an alternative strategy to generate mesoporous structures due to the rigid lyotropic liquid crystal formed at high concentrations of surfactant. In 1995, Attard et al. reported the formation of mesoporous silicas using the LCT strategy.[22] The resulting mesostructure is truly replicating the original architecture of the LLC template. This implies that the phase diagram of the combination of surfactant, silica and water at high surfactant concentration is similar to the well-known phase diagram of surfactant and water. **Figure i.iiib** displays the mechanism of self-assembly of LCT. The mesoporous structure is obtained when the surfactant is added to a solution to form the liquid crystal.[20] After achievement of the porous structure of the surfactant, a porous material can be prepared by (electro)chemical or thermal treatment. However, to form a self-assembled lyotropic liquid crystalline phase, a high concentration of surfactant is required, resulting in high viscosity of the solution. Hence, this high viscosity leads eventually to improper crystal growth with an inhomogeneous surface due to mass transport limitations in the viscous solution. Nevertheless, the preparation of various mesoporous metals, for example, platinum, iridium and nickel, is compatible with this technique.[1] In order to improve the above-mentioned limitation, true liquid crystal templating seems to be the most suitable approach for mesoporous metal and alloy synthesis.

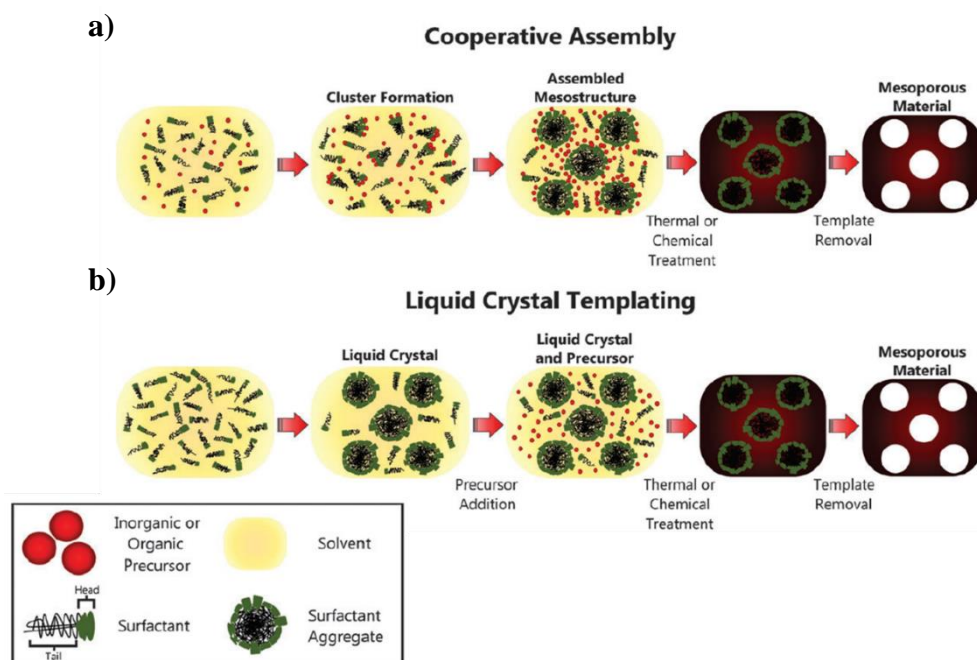


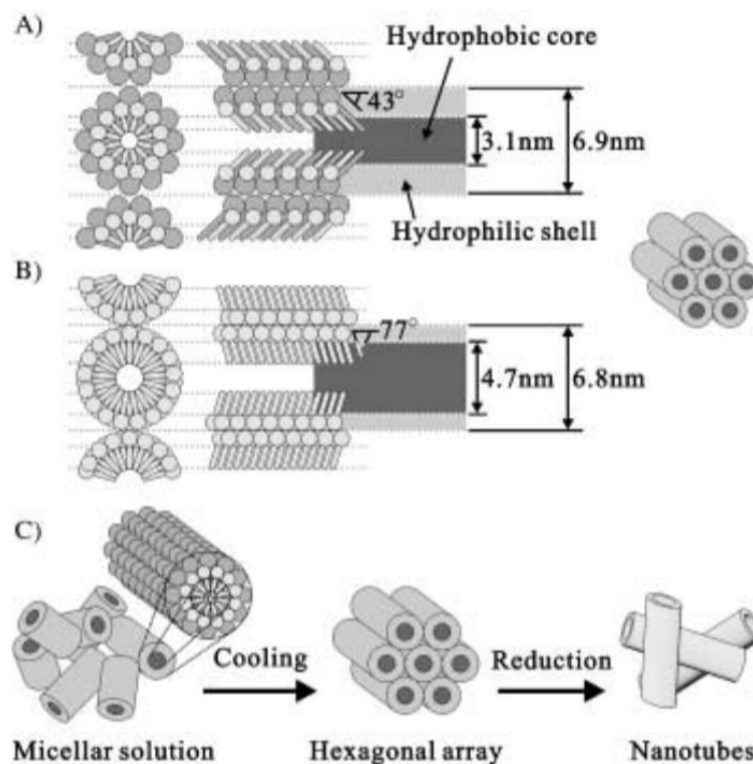
Figure i.iii Mechanisms using soft templates to obtain mesoporous metals via cooperative assembly (top) and liquid crystal templating (bottom) taken from Ref. [23].

In 1997, Attard and co-workers were the first group demonstrating the preparation of mesoporous Pt microparticles from LLCs, which is considered as the first true mesoporous metal.[24] The LLC mixtures were prepared by dissolving hexachloroplatinic acid (IV) hydrate (H_2PtCl_6) in the presence of nonionic surfactant $\text{C}_{16}(\text{EO})_8$ (EO =ethylene oxide). For Pt deposition, reducing agents were added to the LLCs. After the removal of the templates, mesoporous Pt microparticles with high surface areas were obtained. However, the uncontrollable reduction process may lead to a broad particle size distribution. However, platinum deposition can also be achieved by electrochemical reduction, for which a well-defined mesoporous structure can be observed by fine-tuning the potential.[1] The resulting mesoporous Pt films are mechanically robust, remarkably flat and shiny. Furthermore, mesoporous platinum films have a large active surface area with respect to commercial Pt black deposited from a conventional electroplating bath without adding any surfactants. With the electrochemical method, the thickness of the deposited films can be directly

controlled through the amount of deposited charge density during the reduction step. Moreover, the mesoporous channels are oriented in a perpendicular way with respect to the electrode surface. This is an important feature because such a pore configuration should increase the accessibility and enhance the efficiency of mass transport. The perpendicular orientation of the mesopores is driven by the electric field generated during the electrodeposition process and the polarity of the substrate. Therefore, the following aspects are important for the production of highly ordered mesoporous metals: (i) the stability of the mesophase in the presence of metal ions confined in the aqueous domain of the LLC (i.e., the formation of highly ordered LLCs); (ii) the reduction process of metal salts in the aqueous domain.

I.II Development of mesoporous metals via the soft templating approach

Due to the versatility of LLCs made from surfactants, soft templating is preferably used instead of a hard-templating. Since the discovery of mesoporous Pt particles and films in 1997, a lot of efforts have been devoted to an extension of this concept to other metals. For example, mesoporous Pd and Ru films have been generated by LLC-assisted electrodeposition.[25, 26] Moreover, alternative metals, which are earth-abundant, cheap and non-noble, such as Ni and Sn, have been also successfully obtained.[27, 28] The diameter of the mesopores and the template structure can be easily tuned by varying the molecular structure of the surfactant and by the addition of lipophilic substances. Other metal-based nanostructures, such as nanotubes, nanorods, nanosheets/plates, and nanoparticles, have been designed. For instance, the unique synthesis of Pt, Pd, and Ag nanotubes, with inner diameters of 3 to 4 nm and outer diameters of 6 to 7 nm, was demonstrated by chemical reduction of the corresponding metal salts in the presence of mixed LLCs of C₁₂(EO)₉ and Tween 60 (polyethylene glycol sorbitan monostearate) as shown in [Scheme i.i](#). [29]



Scheme i.i Schematic illustration of the formation of platinum nanotubes prepared by various amphiphilic templating systems: A) Mixed C₁₂EO₉ and Tween 60; B) single C₁₂EO₉ surfactant forming cylindrical rod-like micelles; C) Possible pathway for the formation of metal nanotubes by the reduction of metals salts confined in the aqueous shell of mixed-surfactant cylindrical micelles. Image taken from Ref [29].

The deposition rate is one of the most important factors to control the structure of mesoporous metals. Recently, the formation of highly ordered mesoporous Ni particles by autocatalytic chemical deposition under controlled bath conditions was proposed.[30] When sodium borohydride (SBH) was used as a reducing agent, a large number of metallic nuclei were immediately formed, and a disordered mesoporous structure was obtained. This relates to the fact that the particle growth was probably insufficient to generate a hexagonal structure in the LLCs as demonstrated in [Figure i.iv a\)](#) and [c\)](#). On the other hand, when dimethylaminoborane (DMAB) was used as a reducing agent, the deposition speed was significantly lower ([Figure i.iv b\)](#) and [i.iv d\)](#)). The metal

deposition led to the formation of spherical Ni particles, eventually resulting in the formation of an ordered mesostructure. Hence, in an electroless deposition system, the deposition rate can be controlled by the nature of the reducing agents. Similarly, for the electrochemical deposition, a slow deposition, controlled by a suitable potential is more appropriate. Attard and co-workers demonstrated the effect of the deposition rate on the order of the mesoporous structure. Mesoporous Pt films were deposited in the potential range from +0.1 to -0.3 V (vs. saturated calomel electrode, SCE). When Pt films were generated at a potential of -0.1 V versus SCE, their XRD patterns exhibited a sharp diffraction peak, corresponding to a periodic distance of 5.3 nm. However, for more negative deposition potentials the order of the mesoporous structure is gradually lost due to the fast deposition rate.

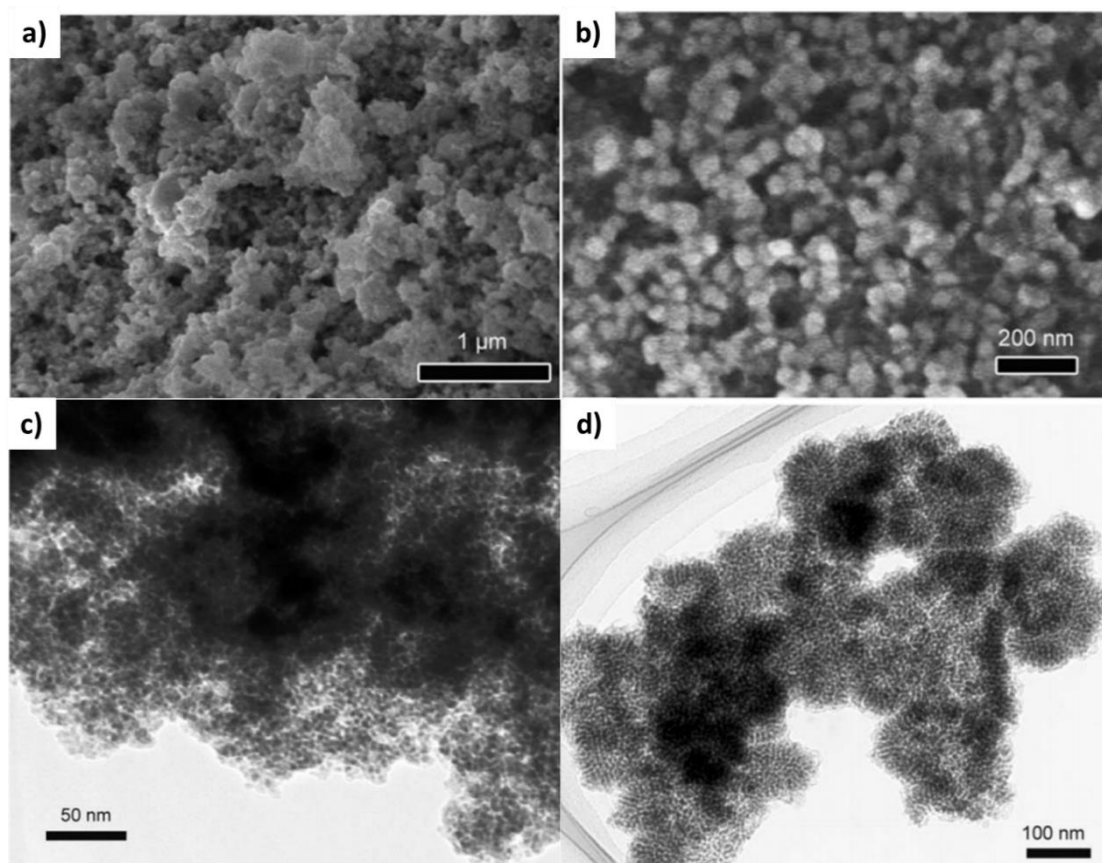


Figure i.iv Illustration of the surface morphology and mesoporous structure of Ni particles prepared using a) and c) sodium borohydride (SBH); b) and d) dimethylamineborane (DMAB). Images taken from Ref [30]

Apart from the deposition rate, which can control the mesoporous structure, the stability of the mesoporous framework is also an important point to be considered. All mesoporous metals except noble metals (e.g., Pt, Ru, and Au) are easily oxidized in oxygen atmosphere. For example, the surface of mesoporous Ni, prepared by electroless deposition, is easily oxidized in air, and therefore a reorganization of the metal atoms is observed. In order to prevent this effect, dehydrated solvents such as ethanol should be used during the removal of the templates. Therefore, the whole experimental procedure should be carried out under inert atmosphere to retain highly ordered mesoporous structures. Moreover, the thermal stability of mesoporous metals is quite low due to the mesoporous framework. In the case of Pt particles, when samples were irradiated by an electron beam for more than 10 min, metal crystals gradually grew, resulting in destroying the ordered mesoporous structures and formation of an aggregation of bulk metal. Therefore, during TEM observations, the power of the electron beam, which also produces a lot of heat, should be carefully considered.

The development of mesoporous alloy structures is also interesting for the advanced design of mesoporous materials. To date, there have been a few reports on the formation of mesoporous alloys, such as Pt/Pd,[31] Pt/Ni,[32] Ni/Co,[33] Pt/Ru,[34] and Te/Cd,[35] by the co-reduction of two metal species in the presence of LLCs. By simply controlling the bath conditions, the composition of the mesoporous framework can be varied. The excellent control of the composition of the framework is of considerable importance in terms of the design of functional mesoporous alloys. In the cases of mesoporous Pt/Pd, Te/Cd, and Ni/ Co, a phase separation of the bimetallic composition is observed at the pore wall. In contrast, the pore walls of mesoporous Pt/Ru and Pt/Ni are in a binary intermetallic state with a uniform dispersion of the constituting metals. A deeper understanding of the alloy composition at the pore wall is of considerable importance for the application of mesoporous alloys. It also provides new insights into the role of bath composition with respect to the grain growth of alloys in the restricted space of LLCs.

Although the use of LLCs is important for the production of mesoporous metal films and particles, the approach still suffers from some drawbacks because the LLCs method cannot uniformly generate a self-assembled structure on the micrometer scale due to the long non-polar tail of amphiphilic molecules. Recently, Yamauchi et al. proposed a convenient and novel pathway, namely evaporation-mediated direct templating (EDIT), for the fabrication of mesoporous metals in a confined area. The EDIT process involves the following two basic steps: i) the formation of the LLC template by solvent evaporation; (ii) the reduction of the metal species in the presence of the LLC. For example, the successful deposition of highly ordered mesoporous Pt inside a conducting micrometer sized channel was successfully reported.[36] A LLC precursor solution was prepared by mixing distilled water, surfactant, Pt species, and ethanol as a volatile solvent. The precursor solution was a homogeneous yellow solution with low viscosity. At this stage, the viscosity of the precursor solution became low with respect to that of general LLC template mixtures used in the previous system. Therefore, the precursor solution can be introduced efficiently into the microchannel channels due to capillary force. After the volatile solvent was perfectly evaporated, the LLCs including the Pt complexes, was formed entirely inside the microchannel. As a consequence, mesostructured Pt can be deposited only inside the channels. The use of lithography techniques allows a selective deposition of mesoporous Pt even only in a particular channel. Moreover, well-ordered Pt thin films with a macro–meso bimodal pore system were prepared by combining the EDIT method with a colloidal crystal-template process.[37]

However, the EDIT process is fundamentally different from the conventional evaporation-induced self-assembly (EISA) method employed for the formation of mesoporous films (e.g., silica). Evaporation-induced self-assembly (EISA) is based on the solvent evaporation generating a self-assembly of surfactant as shown in [Figure i.v](#). The solution of EISA is composed of a volatile solvent, a precursor and surfactant, and subsequently the solution is evaporated in order to increase the concentration of surfactant until reaching or being above CMC to form the lyotropic liquid crystalline phase.

The stage at which surfactant starts forming the micelle structure, is called “tunable steady stage”. If the solution is continuously evaporated, the liquid crystalline structure will finally “lock-in” as the final feature. Therefore, the structure of the surfactant state can be tuned by controlling the evaporation rate of a volatile solvent, which needs to be slow because a too fast evaporation may create a disordered mesoporous structure or the precipitation of unwanted solid.[20]

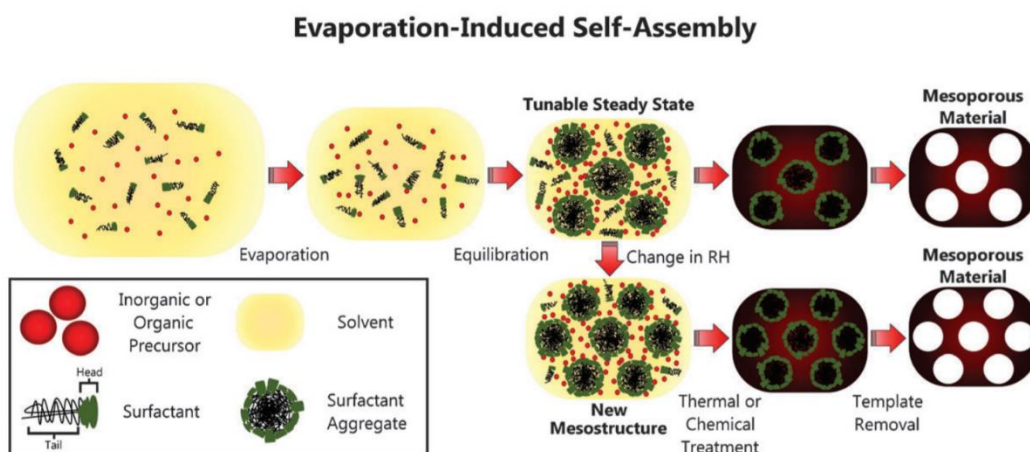


Figure i.v Schematic illustration of the formation steps of evaporation-induced self-assembly. The image is taken from Ref. [23]

In the EDIT system, a homogeneous precursor solution is initially prepared, and then preferential evaporation of ethanol accelerates the formation of LLC mesophases. During LLC formation, no reactions occur among metal species and it is reasonable to assume that these species are stabilized in the aqueous LLC domain. In contrast, in the EISA system, the polymerization of inorganic species occurs simultaneously during solvent evaporation, thus varying interactions between the inorganic species and surfactants are inevitable. Therefore, several types of phase transformation of mesoporous structures have often been observed in the films, depending on the experimental conditions. In the EDIT system, the final LLC mesophases after preferential evaporation of ethanol can be directly predicted by a phase diagram of ternary composition including surfactant, water and metal species, irrespective of the amount of ethanol. In the direct-template approach of LLCs, it is possible to

predict the final structures after metal deposition obtained from the original LLC mesophases. The LLC mesophases act as true templates, and thus, the final material is formed following the direct-template process induced by the LLC formed during solvent evaporation. Consequently, the EDIT system is quite different from the conventional EISA system. This concept has also been applied for the synthesis of mesoporous carbon materials obtained from soluble phenolic resin and triblock copolymers. The self-assembly of triblock copolymers is induced by solvent evaporation. At this stage, the triblock copolymers are assembled together with phenolic resin, and condensation of the latter does not occur. The polymerization is carried out in a subsequent thermopolymerization process.[38]

I.III Chiral imprinted mesoporous metals

Although there are several approaches, including cooperative assembly (CA), liquid crystal templating (LCT), evaporation-induced self-assembly (EISA) and evaporation-mediated direct templating (EDIT), widely used to generate the LLC phases, LCT has been one of the most popular methods to prepare mesoporous metal films due to its simplicity. Recently, mesoporous metals prepared by LCT have been widely used for many potential applications, for instance, catalysis, electrocatalysis, energy conversion and energy storage. One of the most promising applications is using mesoporous metals as electrocatalysts for pharmaceutical applications by encoding molecular information in the mesoporous metal matrices. Recently, chiral imprinted mesoporous metal surfaces were proposed by combining the self-assembly of amphiphilic molecules together with molecular chiral structures.[2] The mesoporous structure could be retained, even in the presence of chiral molecules in the plating solution. The mechanism of the self-assembly of polyethylene (10) cetyl ether (Brij C10) is represented in [Figure i.vi](#). It was found that the chiral imprinted mesoporous platinum films preferentially react with the initially imprinted chiral template molecule, whereas the reactivity was significantly lower for the opposite enantiomer. The high enantioaffinity might originate from the synergy between the high electroactive surface and the

enantioselectivity of the imprinted sites. This fascinating material can be used for various applications. For example, mesoporous platinum imprinted with mandelic acid (MA) was used as electrode for the chiral discrimination of 3,4-dihydroxyphenylalanine (DOPA). Interestingly, mesoporous platinum imprinted with R-MA preferentially reacts with L-DOPA and an analogous behavior has been observed when using electrodes imprinted with S-MA, which preferably convert D-DOPA. This confirmed the presence of chiral information in the encoded metal matrices, opening interesting perspectives for pharmaceutical applications. [39] Moreover, the footprints mimicking the chiral molecular structure can be used for enantioselective synthesis. Yutthalekha and co-workers reported the use of such designer materials for the enantioselective synthesis of MA by using MA imprinted mesoporous platinum.[3] Remarkably, under the most suitable conditions, the enantiomeric excess can reach 20 %ee.

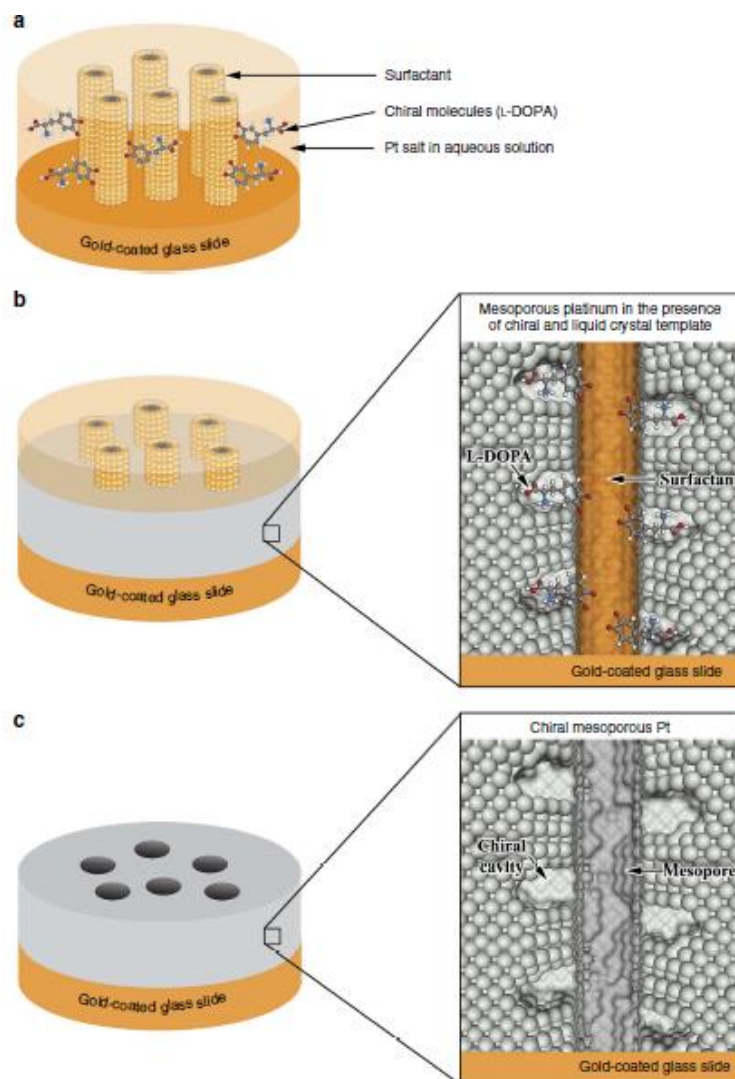


Figure i.vi Preparation scheme of chiral imprinted mesoporous platinum on a gold substrate. a) self-assembly of a lyotropic liquid crystal and chiral templates, b) electrodeposition of platinum covering the lyotropic liquid crystal and chiral molecules, c) obtained final chiral cavities after template and surfactant removal, taken from [2].

II. Design of macroporous metals

Apart from mesoporous metals, highly ordered macroporous metals have also played an important role in materials design over the past decades due to the good accessibility of the macroporous framework. Macroporous metals can't be prepared via soft templating because the LLC phases have lattice parameters in the range of 2–15 nm. Therefore, an alternative way with

complementary performance has been developed, namely the concept of hard templating.

II.I Fundamentals of the hard templating approach

Hard-templating is a powerful method that accurately replicates in the new material the inverse morphology of the template, which is the so-called “mold”. Porous materials at the nano- and micro-scale, are perfectly formed around the mold. For the hard templates, two crucial points need to be considered:[40] one is whether the mold can retain its ordered structure during the material synthesis; the second is whether the mold can be easily removed without destroying the replicated structure. In general, the procedure for synthesizing macroporous metals via the hard templating method is divided into four main steps: (i), the preparation of a precursor solution with suitable interactions between the precursor molecules and the mold surface; (ii) the precursor filling (**Figure i.vii left**) or coating (**Figure i.vii right**) by soaking in the precursor solution; (iii) the materials formation by chemical, electrochemical or thermal treatment; (iv) the removal of the template by chemical etching.[41-44] It is important to note that a suitable strategy for template removal is mandatory to avoid destroying the porous structure of the synthesized materials.

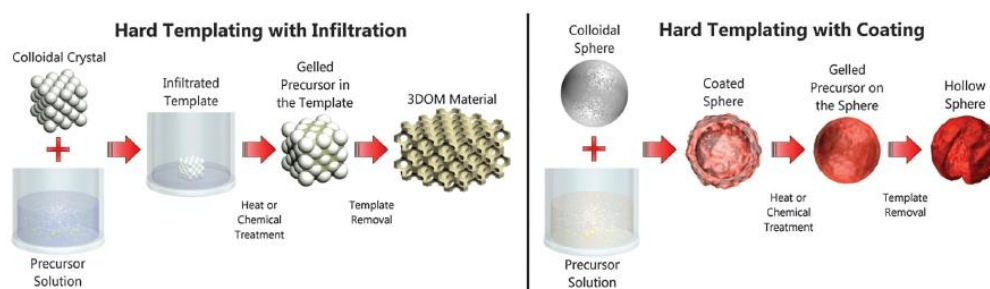


Figure i.vii Preparation scheme of porous materials via hard templating; taken from [23].

For the synthesis of macroporous materials via hard templating, various types of molds have been used, for example powders,[45] films,[46] fibers[47] and monolithic objects.[48] The hard template is universally classified into two different types; (i) *in-situ* templates and (ii) discrete particles. *In-situ* templates are generated by fine-tuning physical and chemical properties of templates, for

example salts,[49] carbon[50] and ice crystals.[51] A too high content of template during the synthesis process can lead to fragile or closed porous structures.[52] Therefore, discrete particles are often used for various applications due to their controllable structure and facile template removal. For example, anodic aluminum oxide (AAO),[46] polymer,[53] and silica spheres[45] are commercially used as molds for generating highly ordered porous structures. Polymer bead templates are prepared with various compositions to control the porous structure and particle distribution, however, polymer templates can easily decompose by dissolution in an organic solvent, and polymer templates often suffer from their soft structure, resulting in a destruction of the porous cavities due to swelling and shrinking phenomena.[17, 48] Therefore, rigid hard templates are often more advantageous. Carbon templates are widely used on a commercial scale due to several advantages, such as being cheap materials and a facile preparation procedure.[48] Silica is also a common material for hard templating due to its advantageous properties, such as robustness, tunable particle size, easily controllable morphologies and high stability under heat treatment. The synthesis of porous materials via a hard template approach opens up perspectives for the design of highly ordered porous materials with complex structures, which cannot be generated by using a conventional approach.

Typically, in order to prepare macroporous metals, uniform template films have been successfully coated on the substrate by a slow evaporation technique. The slow evaporation method relates to the sedimentation of spherical materials in a closed chamber, and subsequently the template particles will settle onto the substrate. After water is slowly evaporated over a period of 3-4 days, this allows the formation of close-packed templates. In 2003, Bartlett and co-workers have successfully synthesized two- and three-dimensional macroporous metals by this slow evaporation technique including Co, Fe, Ni and NiFe and studied their magnetic property compared to compact metals.[54]. The magnetic properties of macroporous films show an important coercivity enhancement compared to flat metal films. However, the disadvantages of the slow evaporation technique are a long operation time, as

well as uncontrollable thickness and homogeneity. To overcome these drawbacks, the Langmuir-Blodgett technique has been proposed as an alternative strategy to obtain highly uniform macroporous structures.

II.II Langmuir-Blodgett technique

The Langmuir-Blodgett (LB) technique is originally a powerful tool for preparing carefully controlled structures of organized molecular assemblies. Theoretically, the LB method offers the possibility to obtain highly ordered, well defined and controlled layer-by-layer deposition.[55] Generally, amphiphilic molecules, composed of two parts including hydrophilic and hydrophobic portions, have been used to modify the substrate surface (**Figure i.viii a**). Water insoluble amphiphilic molecules form a floating monolayer at the air-water interface as shown in **Figure i.viii b**. Subsequently, the floating layer is compressed to generate a homogeneous film by following the surface pressure at the water interface (**Figure i.viii c**). Finally, the Langmuir film can be transferred onto a solid substrate to create mono or multilayer LB films as shown in **Figure i.viii d**. A completely analogous concept can be used to transfer organized layers of amphiphilic particles instead of molecules. For instance, in 2011, Reculosa et al. have successfully prepared a macroporous gold electrode with a well-defined pore size and tunable thickness via the LB technique for electrocatalytic O₂ reduction. It was found that the electrocatalytic performance significantly improves compared to a flat electrode.[41, 56] The macroporous gold electrode exhibited outstanding properties, such as robustness, good mechanical stability and a high electroactive surface area, continuously increasing with the number of deposited layers. In another example, macroporous antimony electrodes were used for the detection of trace amounts of heavy metals.[57] Such electrodes allow a highly sensitive analysis of Cd(II) and Pb(II). Despite the good accessibility of the macroporous framework, the electroactive surface area is theoretically smaller compared to meso- and microporous electrodes with the same thickness. Therefore, in order to combine the advantages of the individual porosities, multiporous or hierarchical porous electrodes have been extensively studied and are also a focus of this thesis.

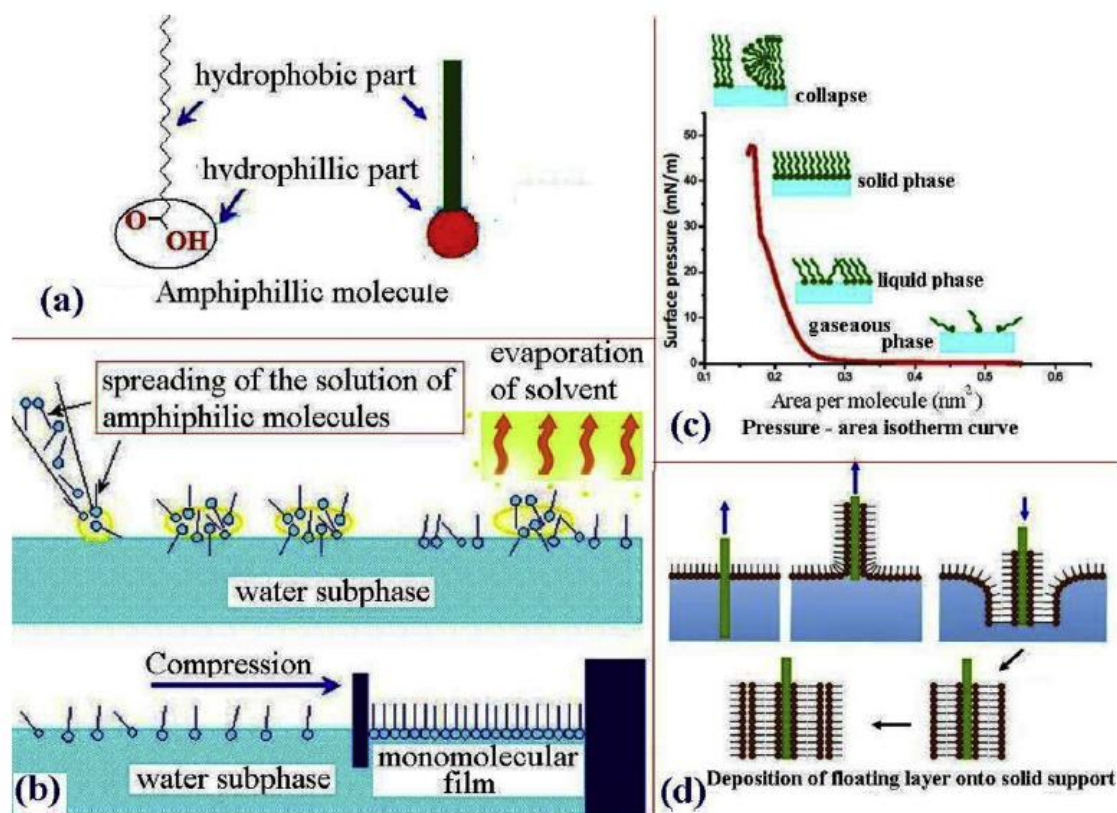


Figure i.viii. Illustration of substrate coating via the Langmuir-Blodgett (LB) technique: (a) molecular structure of an amphiphilic molecule, (b) LB film preparation, (c) surface pressure of LB film during compression and (d) multilayer coating of a substrate. The images are taken from Ref [55].

III. Multiporous metals

As already mentioned, using materials with a single type of pores can have some drawbacks and therefore alternative strategies have been proposed to circumvent these problems. Among them, the combination of various ranges of pore sizes to generate hierarchical porous materials is one of the most promising strategies. Hierarchical porous metals can be composed of dual porosities (micro-mesopores, micro-macropores and meso-macropores) or show multiple porosity (micro-meso-macropores). The simplest approach to obtain hierarchical porous metal is dealloying of bimetallic or trimetallic materials. Typically, electrochemical or chemical dealloying is used to obtain

porous structures. The selective dissolution of metals in alloys can be tuned due to their different standard redox potentials and chemical properties. For example, Qi and coworkers demonstrated an improved electrocatalytic performance and stability of hierarchical porous Cu and porous bimetallic Cu-Ti for hydrogen evolution reaction.[58] The electrocatalyst was prepared using three different components including Al, Cu and Ti. The three metals were combined via arc melting, and subsequently a spinning technique was used to remelt the alloy and rapidly quench it on a spinning metal roller. In order to generate hierarchical porous Cu, the trimetallic mixture was treated in a two-step dealloying process, by using basic and acid media. The additional porous framework (**Figure i.ix**) exhibits high electroactive surface area, leading to high electrocatalytic performance for hydrogen evolution in terms of activity, selectivity and stability.

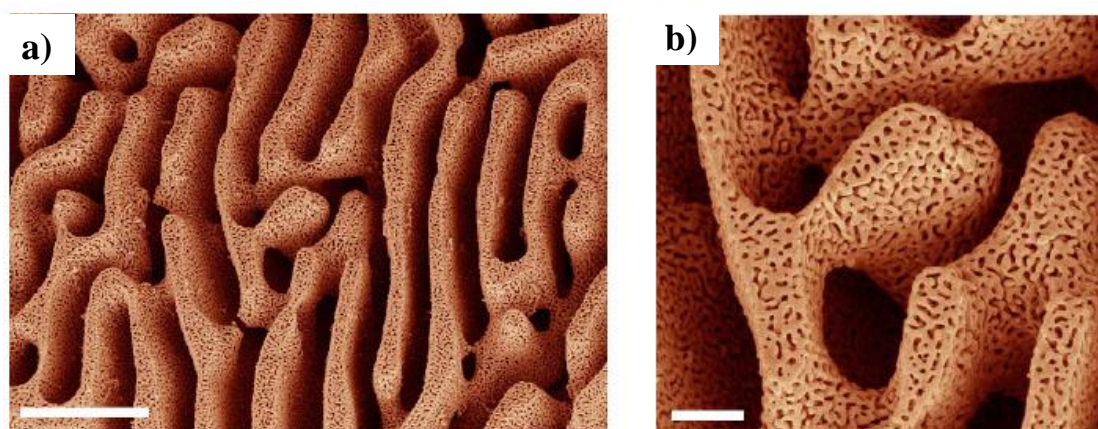


Figure i.ix SEM characterization of multiporous Cu after selective dealloying: (a) SEM image with 1 μm scale bar and (b) high magnification SEM image with 200 nm scale bar. The images were taken from Ref [58].

However, dealloying produces unordered multiporous structures with less control over the final morphology. Thus, the templating approach is an important alternative to prepare hierarchical porous metals. **Figure i.x** represents the general synthesis scheme of multiporous materials prepared by combining hard templating and soft templating approaches. However, when combining soft and hard templating, some additional steps are necessary. For

instance, when the evaporation-induced self-assembly is used for generating the soft template, solvent must be allowed to evaporate after infiltration into the macroporous template in order to generate the liquid crystalline phase. Furthermore, the self-assembly of soft template can be perturbed if the hard template is at the nano-scale, leading to different liquid crystalline structures. Various hard templates including biological samples, three-dimensionally ordered macroporous (3DOM) structures, porous foams, AAO membranes, and colloidal crystals have been widely used for forming hierarchical porous materials combined with a soft template. For example, multiporous TiO_2 was successfully prepared by using 3DOM as a mold, and pluronic P123 as a soft template.[59] Two different confinement effects were observed during the preparation process. First, the 3DOM template prohibited shrinking of the lyotropic liquid crystal, resulting in a larger mesopore diameter compared to normal flat TiO_2 as a substrate. Second, the orientation of the cubic mesoporous network changed from a mesoporous structure to a macroporous framework.[59] Porous foams are another option which can provide large inter-pore connections of up to 100 μm . Hierarchical 3DOM obtained from polyurethane (PU) and P123 was also used as multiporous template for the regrowth of bone tissue.[60] However, 3DOM and porous foam require too many preparation steps to generate highly-ordered porous molds. Therefore, a multiporous templating approach by using colloidal crystal templates is an interesting alternative method due to controllable pore size, good inter-macropore connection and a highly ordered macroporous network.

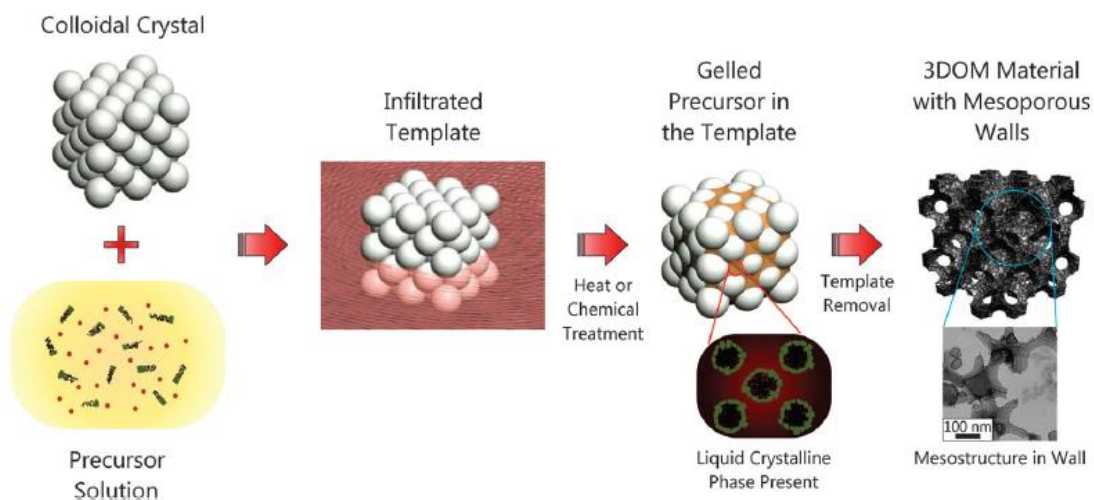


Figure i.x Illustration of hierarchical porous material preparation based on a combination of hard and soft templating methods, taken from Ref [23].

As mentioned above, the combination of micelles/lyotropic liquid crystals and silica beads is one of the simplest methods to create highly ordered multiporous metal, especially when using the LB technique for preparing the solid macroporous template. For example, Heim and coworkers reported the elaboration of an electrode with decorated macropores and mesopores for methanol oxidation and compared their efficiency with structures having a single porosity or a flat platinum electrode as shown in [Figure i.xi](#).^[42] The colloidal crystal template was established by using the LB technique. Sodium dodecyl sulfate (SDS) self-assembled under the influence of the potential applied during electrodeposition in order to generate the mesoporous structure. After template removal, highly ordered porous Pt electrodes were obtained. Interestingly, the electrocatalytic reaction with hierarchical porous platinum was very significantly improved after integrating multiporous functions with respect to flat electrodes. This confirmed the synergistic effect of a combination of mesopores and macropores.

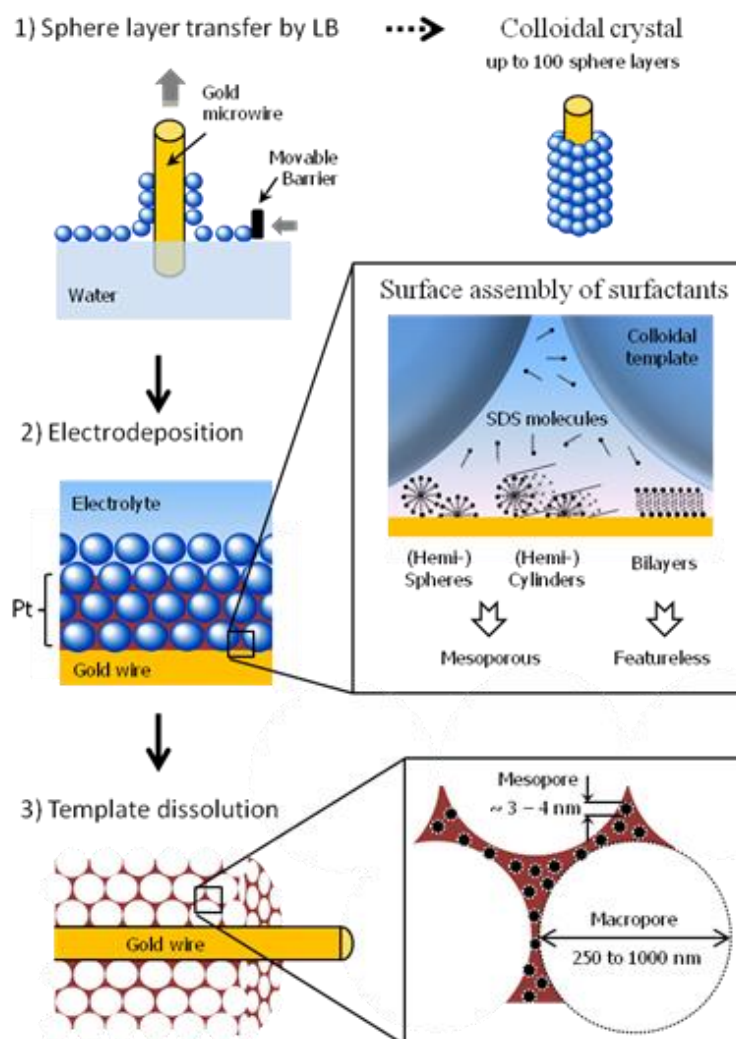


Figure i.xi Illustration of preparation steps of multiporous Pt electrodes obtained by combining hard and soft templating approaches, taken from [42].

All these promising previous results from the literature gave us a strong motivation to design, synthesize, characterize and use advanced porous materials for various potential applications. For the synthesis procedures, we focused on using both soft and hard templating approaches. Therefore, the objective of this thesis is to design and study the activity, selectivity and stability of various porous materials compared to typical flat matrices. Various materials and their applications have been investigated according to the following order:

Chapter 1 deals with the enantioselective synthesis of chiral compounds by using a molecular imprinting approach combining chiral information with mesoporous structures in metal matrices. To improve the efficiency of

enantioselective synthesis, the electrodes with chiral features are combined with pulsed electrochemistry to optimize the enantiomeric excess. Moreover, this chapter also focuses on non-noble, and earth-abundant metals to minimize the costs of the preparation. When using pulsed electrochemistry, the enantiomeric excess could be enhanced very significantly for both noble and non-noble metals.

Chapter 2 describes the fine tuning of the enantioaffinity of a chiral metal phase. With a suitable applied potential, a racemic solution can be completely separated inside a microfluidic channel when using chiral encoded mesoporous platinum as a stationary phase.

Chapter 3 presents the preparation of hybrid imprinted platinum-polypyrrole films as enantioselective actuators for the detection of mandelic acid enantiomers in the presence of an electric field. Under suitable conditions, the free-standing hybrid film shows more pronounced actuation in the presence of the “right” enantiomer compared to “wrong” configuration.

Chapter 4 illustrates the benefits of combining hard and soft templating methods to generate hierarchical meso-macroporous structures for the electrocatalytic oxygen evolution in basic media on a nickel electrode. The electrocatalytic performance and stability of the multiporous electrode was improved due to the synergy of both types of porosity.

Chapter 5 presents the conclusions and proposes perspectives with respect to four topics: (i) chiral imprinted metals for chiral synthesis; (ii) enantioseparation with chiral encoded metal phases; (iii) hybrid chiral imprinted platinum-polypyrrole; and (iv) multiporous electrodes for electrocatalytic applications.

Chapter 1

Highly enantioselective synthesis of chiral compounds on chiral encoded mesoporous metals surfaces

1.1 Introduction

Rational design and engineering of chiral surface properties has been one of the most fascinating topics in the modern chemical community to obtain enantiomerically pure compounds (EPC),[61, 62] owing to its significance in various fields ranging from surface science[63, 64] and materials engineering,[65] to molecular discrimination[2, 3, 39] and catalysis[66]. Until now, although there have been several strategies to obtain a pure single enantiomer, including asymmetric synthesis, crystallization and separation,[2, 3, 6, 67, 68] enantioselective synthesis is one of the most promising approaches due to its controllable and tuneable features which allow minimizing the formation of unwanted chiral compounds.[2, 3, 69-71] Ideally, enantioselective synthesis can perfectly produce one configuration of a chiral compound with very high purity, however, under real conditions, both enantiomers are produced with one being predominant. In recent decades, asymmetric synthesis has been widely studied with many kinds of chiral surfaces, obtained by molecular adsorption on metal surfaces, asymmetric binding or grafting on a metal surface, cutting single crystals along high Miller index planes, distortion of metal surfaces and molecular imprinting of metals.

Molecular adsorption on metal surfaces is the process where molecules are immobilized on metal surfaces. The most interesting feature of this strategy is that the asymmetric surface is easily generated by physical adsorption of chiral molecules on metal surfaces. Over the past decades, two heterogeneous catalysts for enantioselective synthesis via hydrogenation of α -keto esters on Pt catalyst and β -keto esters on supported Ni have received attention.[72, 73]

Interestingly, the highest chiral induction was obtained for the samples which were modified by chiral molecules compared to non-modified metal surfaces. For example, cinchona alkaloid was the most suitable molecular adsorbent on Pt surfaces,[72] while α -hydroxy acids and α -amino acids were widely used for modifying Ni surfaces,[73] even though it was not completely clear how the modifiers induce chirality at achiral surfaces.

The adsorption mechanism and behavior of molecularly modified metal surfaces was studied by using *R,R* tartaric acid as a modifier on 2-dimensionally anisotropic Cu (110).[74] *R,R* tartaric acid is a chemically versatile molecule, existing in three different forms: the neutral bi-acid form, the monotartrate and the bitartrate form which are a well-known modifiers for the enantioselective transformation of methyl acetoacetate to *R*-hydroxybutyrate.[75, 76] The effect of temperature and coverage on the configuration of surface molecules was investigated and allowed the establishment of an adsorption phase diagram on Cu (110), as illustrated in [Figure 1.1](#). The presence of functional groups of *R,R* tartaric acid on Cu (110) was confirmed by using *in-situ* Fourier transform reflection-absorption infrared spectroscopy (FT-RAIRS). At a very low adsorption temperature (83K), there was no change in the FT-RAIRS spectrum as a function of increasing coverage time, implying that *R,R* tartaric acid has a complex H-bonded crystalline structure, which could be formed via intermolecular hydrogen bonds between two acid groups. At 300K, the neutral bi-acid form and the monotartrate was observed on the Cu (110) surface, and subsequently the monotartrate was homogeneously adsorbed on the Cu surface after long exposure time. Two adsorbed species were observed by varying the coverage at 350 K. Monotartrate species are adsorbed on the Cu surface in the beginning and slowly change with time to bitartrate. When increasing the temperature above 405 K, the modifier was solely in the bitartrate form. These results allow elucidating the molecular mechanism of the interaction between the adsorbent and the metal surface, which is responsible for the chiral features of the asymmetric surfaces. However, the weak interactions between modifier and metal surface can lead to a loss of chiral information, and therefore the interactions between both elements need to be improved. Thus, the trend of

the development of asymmetric catalysts has moved towards using chiral metal complexes, as well as covalent binding and grafting approaches.

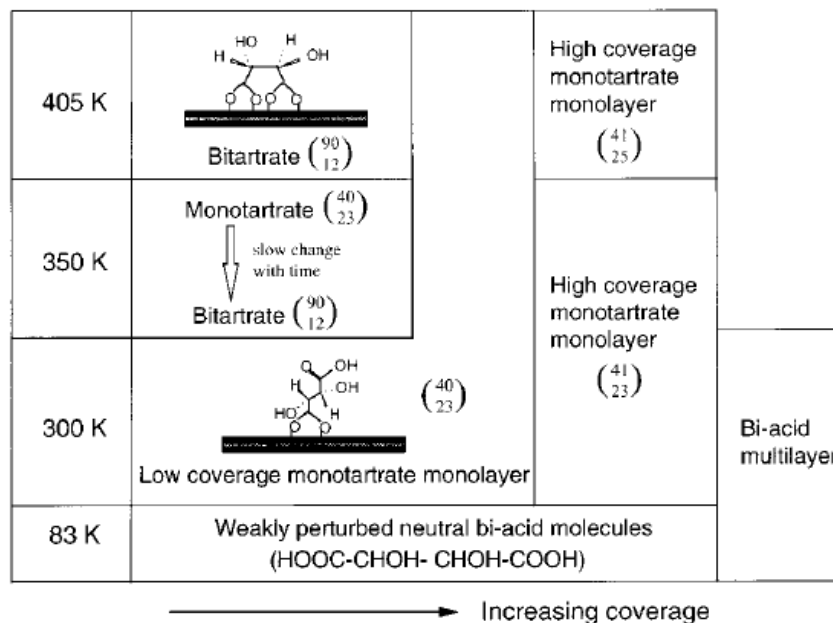


Figure 1.1 Adsorption phase diagram of *R,R* tartaric acid on 2-dimensionally anisotropic Cu(110) surfaces as a function of temperature and coverage. Taken from Ref [74].

Chiral metal complexes are the most interesting homogeneous catalysts, which have been widely used for asymmetric chemical transformation, including C-C bond formation with high efficiency and selectivity.[77] However, the application of these homogeneous catalysts is still limited when using them in large-scale industrial processes, due to the difficult catalytic removal from the reaction mixture.[78, 79] To overcome these drawbacks, large-scale synthesis normally requires heterogeneous catalysts, having several advantages such as easy catalyst removal, low cost, less metal impurities and a more straightforward scale-up including continuous flow systems.[80] One of the most common ways to improve chiral metal complexes is changing from homogeneous catalytic systems to a heterogeneous phase by binding or grafting of chiral ligands on inorganic support or metal surfaces.[81] Although this strategy has been extensively applied for several reactions, it often suffers from some limitations, for instance metal leaching, instability of the chiral ligand, fast deactivation and a complicated preparation process.

In order to solve the above-mentioned limitations, chiral molecules immobilized on metal nanoparticle surfaces have been developed because of promising advantages, for instance a large surface area, good activity and high selectivity towards the desired products.[82] Chiral nanoparticles have been successfully synthesized by combining chiral ligands and metal nanoparticles or by using chiral ligand-stabilized metal nanoparticles. The concept was first proposed in 1956 by using ligand-modified Pd as a catalyst for hydrogenation.[83] Furthermore, Orito and co-workers studied enantioselective hydrogenation of methyl pyruvate and methyl benzoylformate by using cinchonidine-modified Pt on carbon in 1979, as shown in **Figure 1.2**. [84] Although the first Orito-type reaction was reported more than 40 years ago, it is still an important topic of investigation because of its significance for the synthesis of intermediates of medical relevance. As a consequence, other types of chiral nanoparticle (NPs) catalysts have been studied, including nickel-boride NPs,[85] Pd NPs,[86] Ru NPs,[87] Ir NPs,[88] Rh NPs[89] and Fe NPs for asymmetric hydrogenation reactions.[90]

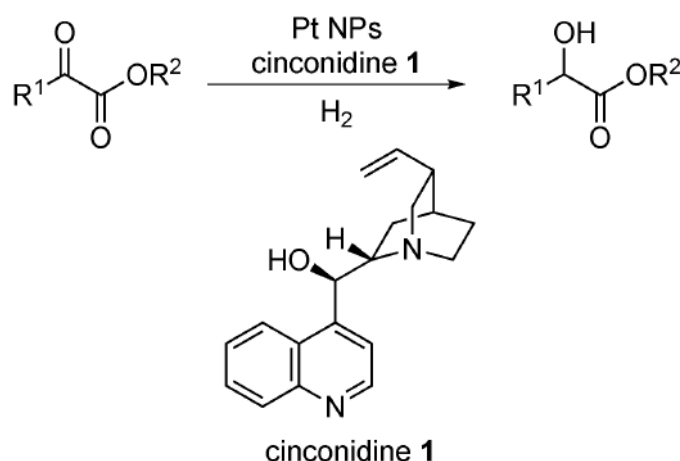


Figure 1.2 Orito-type reactions, taken from Ref [91].

However, some mechanisms of nanoparticle catalysis are also related to homogeneous catalysis due to partial metal dissolution which was observed during the catalytic processes, indicating that the active species is not simply a molecular metal complex. Even though the real structure of chiral ligand-

stabilized metal nanoparticles is still not clarified, several studies suggest that a redox event between reagent and nanoparticles might be the key factor to initiate nanoparticle catalysis.

Apart from the examples mentioned above using binding or grafting of chiral ligands, another way to develop enantioselective metal surfaces is by creating a really asymmetric metal environment by controlling the arrangement of kinks, steps and terraces of the metals. Kink sites on single crystal metal surfaces exhibit an asymmetric environment when the step length or faces at the outer surface are unequal. Therefore, it is possible to synthesize a single crystal with intrinsic handedness. Generally, in order to prepare asymmetric kink sites on a single-crystal metal, surfaces are cut under ultrahigh vacuum. The first study was reported by Gellman et al. in 1996.[92] Asymmetric Ag single crystals were prepared with both surface configurations; a Ag(643)^R surface and a Ag(643)^S surface, which are enantiomeric configurations of each other. The different configurations of the single crystal surfaces were investigated by desorption kinetics of (*R*)- and (*S*)-butanol. Unfortunately, the difference of desorption energy of chiral butanol on Ag(643)^R and Ag(643)^S is less than 0.1 kcal/mol. In order to better understand the difference in recognition behavior of two enantiomeric metal surfaces, Attard et al. studied the effect of an asymmetric Pt environment on *D*- and *L*-glucose oxidation. In comparison, Pt(531) exhibited a high diastereomeric excess of about 80%, as shown in **Figure 1.3a** whereas only 60% diastereomeric excess was observed in the case of Pt(643), as represented in **Figure 1.3b**. [93] This experiment is the first proof-of-concept that cutting metals allows discrimination of enantiomeric compounds. However, although the above-mentioned approach can be used to generate an asymmetric environment for chiral applications, the complex preparation and

uncontrollable number of active sites are quite limiting factors for practical applications.[93]

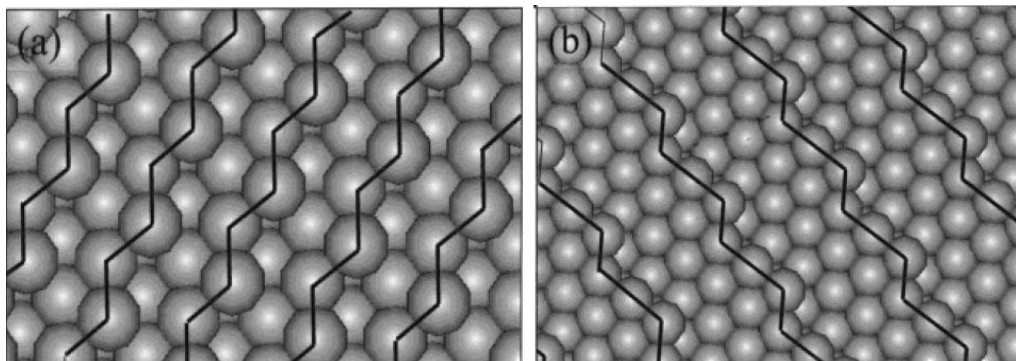


Figure 1.3 a) Ball model of a) fcc(531) and fcc(463), taken from Ref [94].

Apart from cutting high Miller index metal surfaces, asymmetric metals can be naturally generated by reorganization or distortion of the metal structures. Recently, extensive studies of the geometric structure and properties of bare gold have shown quite unique structures with fascinating properties. For instance, gold clusters with a small size like Au_n ($n < 6$) exhibit several low-energy configurations as shown in [Figure 1.4](#). [95] In the intermediate size range ($n = 12-55$), there are many topological low-symmetry configurations, in which the energy of the disordered configuration is between or below the lowest-energy configurations. [96] In this case, the distortion of the Au cluster structure depends on whether the reorganized structure allows to lower the cluster energy. In order to study the passivation of gold in thiol solution, methylthiol was used as a distortion agent. The structure of the Au cluster was distorted by introducing a strong covalent bond in the metallic cluster core. [97] Although these strategies present the advantage of a high surface area of the metal clusters and a facile synthesis, the structures and specific interactions between distortion agent and metal are limited.

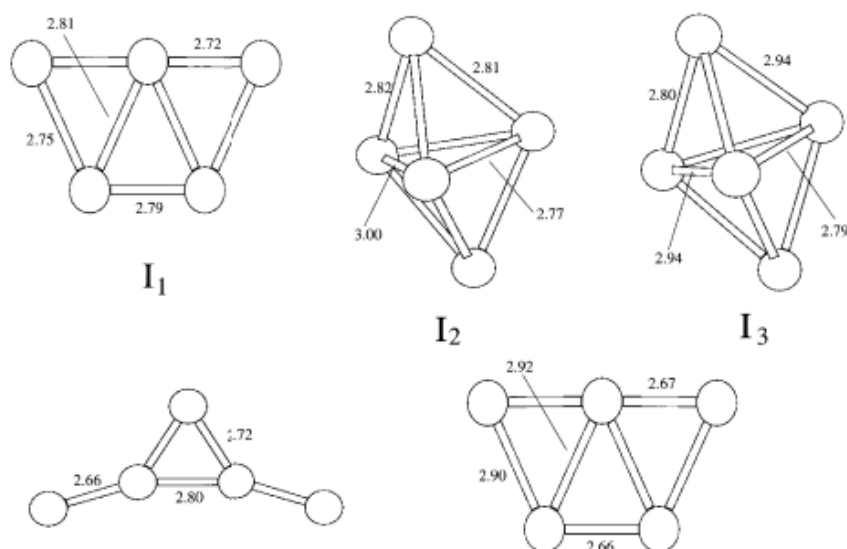


Figure 1.4 Structure prediction of Au₅ with various possible configurations, depicted from Ref [95].

Molecular imprinting techniques (MIT) are an alternative approach for designing heterogeneous catalysts, naturally mimicking chiral molecular structures by an inverse replication. Various types of molecular imprinted materials have been successfully obtained over the past decades with a precisely controlled shape and structure inside the imprinted matter, for example by molecular imprinting on silica beads,[98] molecular imprinting polymers (MIPs) [99-102] and bio-imprinted materials.[103] The concept of this approach is based on an *imprinting antigen* (imprinted molecules), which is used for creating the chiral information in the imprinted materials. The preparation procedure starts from a solution containing a mixture of the chiral templates and material precursors, and subsequently, the matrix is grown to cover the imprinting agent, establishing a chiral cavity inside the prepared material. In MITs, MIPs have been widely used in various applications owing to many advantages including a simple and inexpensive preparation as well as high mechanical, heat and pressure resistance.[104] Currently, the approaches for the synthesis of MIPs are divided into two methods, namely the *covalent approach* and the *non-covalent approach*. The covalent method relates to the

generation of a chiral environment using the imprinting antigen, which is covalently bound to a monomer before polymerization and after the polymer has been grown around the chiral template, the covalent bond between imprinted antigen and the polymer is cleaved at the functional binding site. Typically, functional groups of molecular templates are aldehyde, alcohol, ketone, amine and carboxylic groups, which can be activated for establishing covalent bonds. The advantage of this approach is that the functional group of the monomer is precisely controlled by the specific binding to the template molecule, eventually retaining the structure of the imprinting antigen. The complementary non-covalent method is very similar, however non-covalent forces, such as H-bonding, dipole-dipole interactions and ion-pairing, are predominant. MIPs obtained via both molecular imprinting techniques display high physical (mechanical stress, high pressure and severe temperatures) and chemical resistance. However, the removal of the template is difficult due to the closed structure. Moreover, the closed chiral cavity doesn't allow reactants to access the chiral selective site for the asymmetric recognition and synthesis.

It is well-known that the integration of mesoporous structures into bulk materials induces outstanding properties, especially a very high active surface area.[1, 105] To synthesize mesoporous metals, there are two efficient approaches, including hard and soft templating methods.[41, 106, 107] However, for meso-scale structures the soft templating approach is a much more promising strategy due to a facile preparation and easy removal of the mesoporegen. Mesoporous platinum, synthesized using a direct-template method, was first proposed by using the non-ionic surfactant Brij C10 to generate a lyotropic liquid crystal (LLC) in the presence of platinum salts.[108] After electrodeposition of platinum and surfactant removal, mesoporous Pt with a high electroactive surface area was obtained. This approach allows creating novel metal structures with a mesoporous framework. Furthermore, many researchers have paid great attention to extend the scope of designing such mesoporous metals by varying the chemical composition in terms of metal salts. For example, mesoporous Pd and Ru have been generated by LLC-assisted

electrodeposition.[25, 26] Moreover, alternative metals, which are earth-abundant, cheap and non-noble, such as Ni and Sn, have been also successfully prepared.[27, 28] Because of the fascinating nanostructure of mesoporous metals and a high electrocatalytic surface area, they allow various applications, especially in the frame of electrochemical conversion.

Creating chiral imprinted mesoporous metal is an alternative challenge in molecular imprinting technology, which exhibits the remarkable benefit of precisely mimicking the cavities of an imprinted antigen. Recently, chiral imprinted mesoporous platinum has been successfully electrodeposited by combining chiral cavities and a mesoporous structure in bulk platinum.[2] The schematic preparation procedure is shown in [Figure 1.5](#). The first step is the self-assembly of surfactant at a concentration allowing the formation of a lyotropic liquid crystal in the hexagonal phase (H_1), leading to non-covalent interactions between chiral templates and the lyotropic liquid crystals. Interestingly, after electrodeposition of the metal, the chiral information is retained even once surfactant and template are removed. The chiral recognition abilities of the prepared electrodes were investigated by using differential pulse voltammetry (DPV) in the presence of different chiral molecules.[109] It was found that the chiral imprinted mesoporous platinum was preferentially reacting with the initially imprinted chiral template molecule, whereas the reactivity is significantly lower for the opposite enantiomer. The high surface area of the mesoporous structure enhances the detection limit during chiral analysis. In addition, the chiral encoded mesoporous platinum electrodes can be also used for the analysis of other compounds with a similar structure.[39] For example, mesoporous platinum imprinted with mandelic acid (MA) was used as electrode for the chiral discrimination of 3,4-dihydroxyphenylalanine (DOPA). Interestingly, mesoporous platinum imprinted with R-MA preferentially reacts with L-DOPA and an analogous behavior has been observed when using electrodes imprinted with S-MA, which preferably convert D-DOPA. This confirmed the presence of chiral information in the encoded metal surfaces, opening interesting perspectives for pharmaceutical applications. [39]

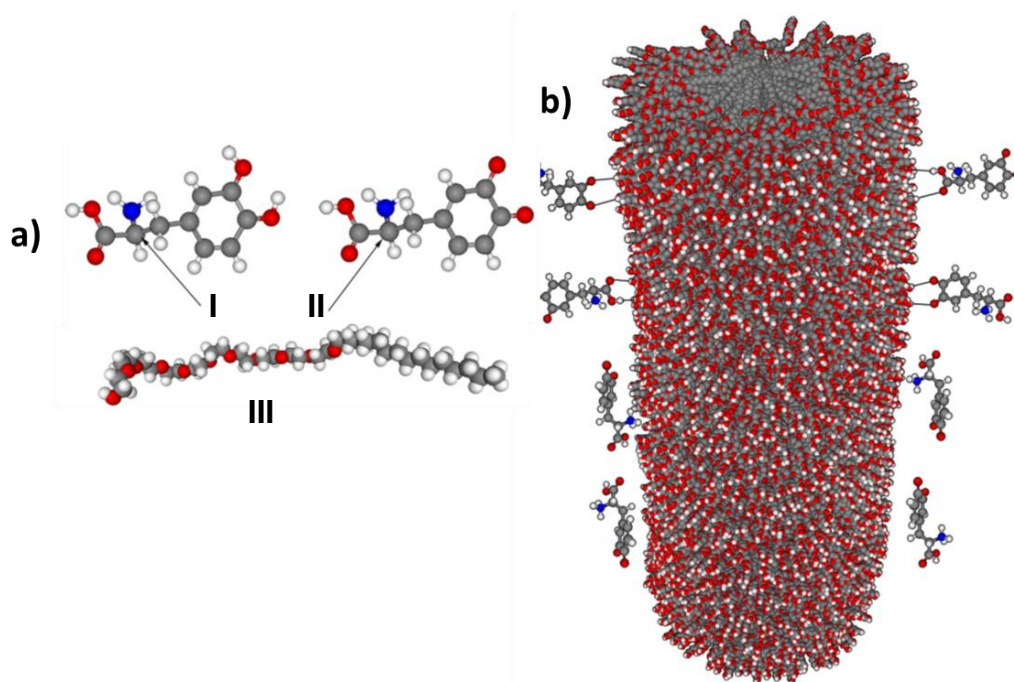


Figure 1.5 Interaction between the chiral template and Brij C10. a) L-DOPA (I), the oxidized form of L-DOPA (II), and the Brij C10 (III). b) The illustration of a column of aggregated Brij C10, depicted from [2].

Apart from the enantioselective analysis of chiral molecules using chiral encoded mesoporous platinum, Yutthalekha and co-workers reported the further application of such designer materials for the enantioselective synthesis of MA by using MA imprinted mesoporous platinum.[3] The electrosynthesis mechanism is shown in **figure 1.6**. **Figure 1.6a** illustrates the hydrogenation process of phenyl glyoxylic acid (PGA), for which hydrogen can be added on the left or the right side of the prochiral carbon. *R*-cavities and *S*-cavities were obtained after the chiral template and surfactant were removed as shown in **figure 1.6b** and **1.6c**, respectively. Applying a negative potential, the chiral imprinted electrode allows the transformation of the prochiral molecule adsorbed in the chiral cavity (**Figure 1.6d**). The product is formed in the asymmetric environment of the chiral porous structure (**Figure 1.6e**) and then the product desorbs from the electrode surface. The efficiency of the chiral synthesis, or enantiomeric excess (%ee), can be calculated by equation 1.1:

$$\%ee = \frac{RMA-SMA}{RMA+SMA} \quad (1.1)$$

where RMA and SMA refer to the concentration of R-MA and S-MA in the solution for a certain reaction time. Moreover, in order to improve the enantiomeric excess, the concentration of imprinted molecules can be optimized. A suitable concentration of imprinted MA is in the range of 3-5% compared to the weight of metal salt. At too low concentrations of imprinted molecules there are only few chiral active sites imprinted in the electrode, whereas at too high concentrations of chiral molecules the formation of the LLC structure is disturbed, leading to a less well-defined mesoporous structure. Remarkably, under the most suitable conditions, the enantiomeric excess can reach 20%ee. Although such a significant %ee can be observed, a large portion of unwanted enantiomer is obtained due to the inference of the reactions at non-imprinted active sites at the external surface of the electrodes. In addition, diffusion limitation inside the mesoporous channels is another important factor that needs to be considered. Another drawback is the use of expensive precious metals and deleterious environmental impact,[110] which makes it difficult to establish the present system at a practical scale. In order to open up more realistic perspectives, the imprinting of chiral information in earth-abundant first-row transition metals such as nickel would be beneficial in terms of cost and sustainability.[111, 112] In addition, nickel is an interesting metal, which shows high catalytic performance for several electrocatalytic reductions, for example, hydrogen production,[113] oxygen reduction[114] and especially electroreduction of organic molecules.[115]

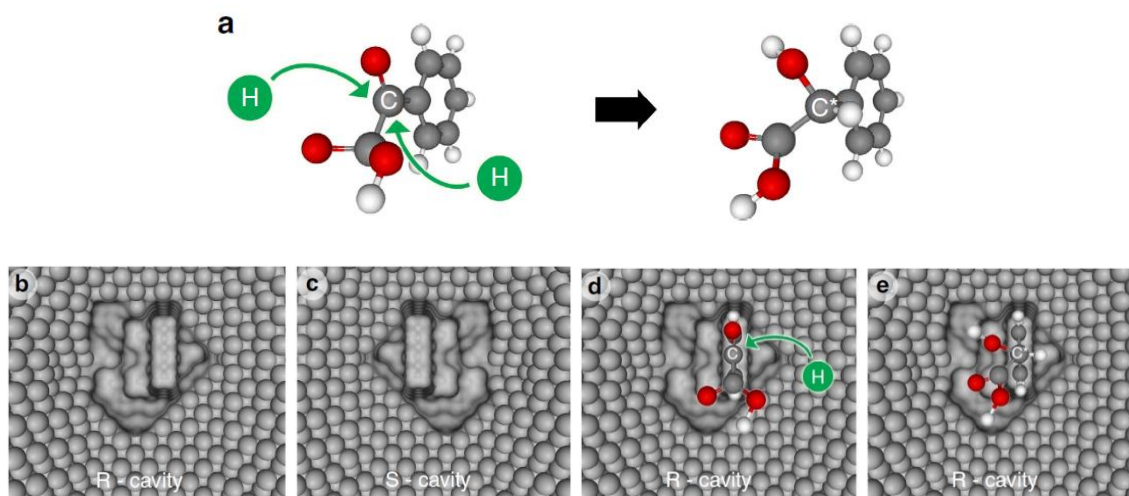


Figure 1.6 Synthesis scheme of mandelic acid: a) hydrogenation of phenyl glyoxylic acid (PGA) to chiral mandelic acid (MA), (b) R-MA chiral cavity, (c) S-MA chiral cavity, (d) adsorption of PGA in R-MA cavity and (e) selective electroreduction of PGA to R-MA, taken from Ref [3].

In the present study, we describe a new concept for highly enantioselective synthesis of chiral compounds via a pulsed electrochemical technique using chiral encoded mesoporous metal surfaces. This strategy has been used in order to improve the enantioselectivity of chiral compounds due to a minimization of the reactions taking place on non-imprinted sites. The degree of enantioselectivity can be tuned by controlling the pulse time and the amount of imprinted active sites. Chiral encoded mesoporous Ni metal has been prepared by electrodeposition of nickel salts ($\text{Ni}(\text{OAc})_2 \cdot 4\text{H}_2\text{O}$) in the simultaneous presence of non-ionic surfactant (Brij C10) and chiral compounds (phenylethanol). To confirm the presence of chiral information in the non-noble metal, the electrochemical electrooxidation of phenylethanol has been used. In addition, in order to illustrate the synergy of chiral features and a mesoporous structure, the chiral electrodes were used for the enantioselective electroreduction of a prochiral compound such as acetophenone to selectively produce phenylethanol enantiomers.

When chiral imprinted mesoporous nickel is used for pulsed electrochemical reduction combined with a fine-tuning of the pulse time and relaxation time, the enantioselectivity is greatly improved.

1.2 Experimental section

Chemicals

Hexachloroplatinic acid hydrate ($\text{H}_2\text{PtCl}_6 \cdot x\text{H}_2\text{O}$), nickel acetate tetrahydrate ($\text{Ni}(\text{OAc})_2 \cdot 4\text{H}_2\text{O}$), sodium acetate trihydrate ($\text{NaOAc} \cdot 3\text{H}_2\text{O}$), boric acid ($\text{B}(\text{OH})_3$), polyoxyethylene (10) cetyl ether (Brij C10), (R)-phenylethanol (R-PE), (S)-phenylethanol (S-PE), acetophenone, isopropanol, potassium hydroxide, sulfuric acid and ammonium chloride were purchased from Sigma-Aldrich. Heptane and hydrochloric acid were purchased from Fisher Scientific and QREC, respectively. All chemicals were used directly without any further purification and all solutions and the plating mixture were prepared using MilliQ water.

Substrate cleaning

Gold-coated glass slides were used as substrates for the electrodeposition of chiral imprinted mesoporous metals. In order to clean the gold surface of the substrates (1.2 cm×2.4 cm), they were sonicated in isopropanol for 30 min, resulting in organic impurities removal. Subsequently, the substrates were rinsed with MilliQ water (18.2 MΩcm) and isopropanol, and then dried with nitrogen. The substrates were connected by soldering a normal wire and the geometric surface area of the electrodes was confined by nail varnish.

Electrodeposition of chiral imprinted mesoporous platinum

Electrodeposition of the chiral encoded mesoporous platinum was carried out following a literature procedure. [2, 3, 39] Chiral imprinted mesoporous Pt electrodes were prepared by electroreduction of the platinum salt in the simultaneous presence of a self-assembled lyotropic liquid crystal and the chiral template. In this contribution, polyoxyethylene (10) cetyl ether (Brij

C10) as a non-ionic surfactant, and enantiomeric phenylethanol were used as a mesopore-directing agent and chiral template, respectively. To prepare plating mixtures for platinum deposition, the liquid crystal composed of 42 wt% Brij C10, 29 wt% chloroplatinic acid, 29 wt% MilliQ water and the desired amount of phenylethanol template were combined. The resulting gel was mixed until becoming homogeneous. The viscous plating gel was carefully placed on the gold-coated glass, and then a platinum mesh was positioned at the top of the gel as a counter electrode. Ag/AgCl was used as a reference electrode in the electrochemical cell. A potential of -0.1 V vs Ag/AgCl was applied to the gold substrate for the reduction of the platinum ions with various charge densities in order to optimize the film thickness. After electrodeposition, all the prepared electrodes were rinsed with MilliQ water several times to remove the chiral template and lyotropic liquid crystal from the mesopores and chiral cavities.

Electrodeposition of chiral encoded mesoporous nickel

Chiral encoded mesoporous Ni electrodes were coated on the gold substrate via the electrodeposition of nickel acetate salt in a presence of lyotropic liquid crystal as a mesopore directing agent and chiral molecules as a chiral template. The plating solution was composed of 0.2 M $\text{Ni}(\text{OAc})_2 \cdot 4\text{H}_2\text{O}$, 0.5 M $\text{Na}(\text{OAc}) \cdot 3\text{H}_2\text{O}$, and 0.2 M $\text{B}(\text{OH})_3$, prepared at 333 K. The liquid crystalline mixture was obtained by combining 35 wt% of the prepared nickel solution, 65 wt% of Brij C10 and 1.45 wt% of (S) or (R)-PE compared to Pt salt under vigorous stirring at 333 K for 15 min until the prepared gel was homogeneous and transparent. Subsequently the gold-coated glass substrate was dipped in the nickel gel for 15 min, and electrodeposition of mesoporous nickel was obtained by applying a potential of -0.86 V vs Ag/AgCl with various charge densities using a conventionally electrochemical cell, including the gold-coated glass slide, a platinum mesh and a Ag/AgCl (Sat. KCl) as a working, counter and reference electrode, respectively. The lyotropic liquid crystal and chiral templates were removed by rinsing with water several times after nickel deposition. Subsequently, the electrodes were kept in nitrogen-saturated water to maintain the chiral information and to prevent nickel oxidation.

Electrode characterization

The surface morphology and the thickness of the chiral imprinted platinum and nickel films obtained with various deposition charge densities were characterized by using a Hitachi TM-1000 tabletop electron microscope and JEOL, JSM-7610F, respectively. Furthermore, the mesoporous structure of the deposited platinum and nickel electrode was confirmed by transmission electron microscopy (TEM) performed on a JEOL JEM-2010 and a JEOL JEM-2100 microscope. For chiral imprinted mesoporous platinum samples, the gold layer was removed by immersing in an aqueous solution composed of 4 wt% KI and 1 wt% I₂ for 20 min. The platinum film was consequently detached from the electrode surface and then was carefully transferred onto the Cu TEM grid. In order to analyze the mesoporous structure of the nickel films, the deposited layer was detached by physical removal and then transferred into an ethanol solution. The mesoporous nickel film was transferred onto the TEM grid and dried at ambient temperature. The electrochemical characterization of chiral encoded mesoporous platinum and nickel films was performed using an Autolab PGSTAT204 equipped with a three-electrode system. The prepared electrodes, a platinum mesh and Ag/AgCl (Sat. KCl) were used as a working, counter and reference electrodes respectively. The surface area of the mesoporous platinum electrodes was measured by cyclic voltammetry (CV) in 0.5 M H₂SO₄ recorded at a scan rate of 100 mVs⁻¹ in the range of – 0.25 to 1.25 V vs Ag/AgCl. However, to obtain the surface area of the prepared nickel electrodes, CVs were recorded in basic solution (1 M KOH) at a scan rate of 100 mVs⁻¹ in the range between 0 and 0.6 V vs Ag/AgCl. Chiral recognition at the prepared electrodes was confirmed by differential pulse voltammetry (DPV) with a step potential and a modulation amplitude of 25 mV in 4 mM PE and 50 mM HCl as a supporting electrolyte at a scan rate 50 mVs⁻¹.

Enantioselective electrosynthesis of chiral compounds

Chiral electrosynthesis of phenylethanol (PE) was carried out in 1 M NH₄Cl as supporting electrolyte containing 4 mM and 10 mM acetophenone in

the case of platinum and nickel electrodes, respectively. In order to optimize the experimental parameters, the reduction potential of acetophenone was studied using CV in 4 mM acetophenone (ACE) and 10 mM NH₄Cl as supporting electrolyte. In the case of chiral imprinted mesoporous platinum electrodes, the conventional electrochemical reduction was performed in a potential range from -0.4 to -0.5 V for 13 h in a stirred aqueous solution. However, when using the chiral imprinted nickel film, a reduction potential of -0.55 V was applied for 12 h. In the case of pulsed electrosynthesis, pulse time and total reaction time was varied in order to find the optimal conditions. After electroreduction, the reaction mixture was extracted by using heptane as a solvent and then the upper layer of the extract solution (heptane layer) was taken and analyzed by high performance liquid chromatography (HPLC) performed on a Shimadzu LC-2030C3D equipped with a chiral HPLC column (CHIRALPAK IB, 250 ×4.6 mm inner diameter) and using a mobile phase containing 95 % (v/v) heptane/5 % (v/v) isopropanol at a flow rate of 0.5 ml/min and an optical detection at 215 nm. To further confirm the enantiomeric nature, the products were analyzed with a Jasco J-815 spectrometer and circular dichroism spectra were recorded at a scan rate of 50 nm/min. The absorption peaks of chiral products and reactant were measured by using Lab Solution software. The enantiomeric excess (%ee) is calculated based on the integrated peak areas of (S)- and (R)-PE using the following equation:

$$\%ee = \frac{SPE-RPE}{SPE+RPE} \times 100 \quad (1.2)$$

where SPE and RPE refer to the obtained peak area of S-phenylethanol and R-phenylethanol, respectively. The standard error of %ee was successfully calculated as standard error of the mean (s.e.m.) based on the following equation:

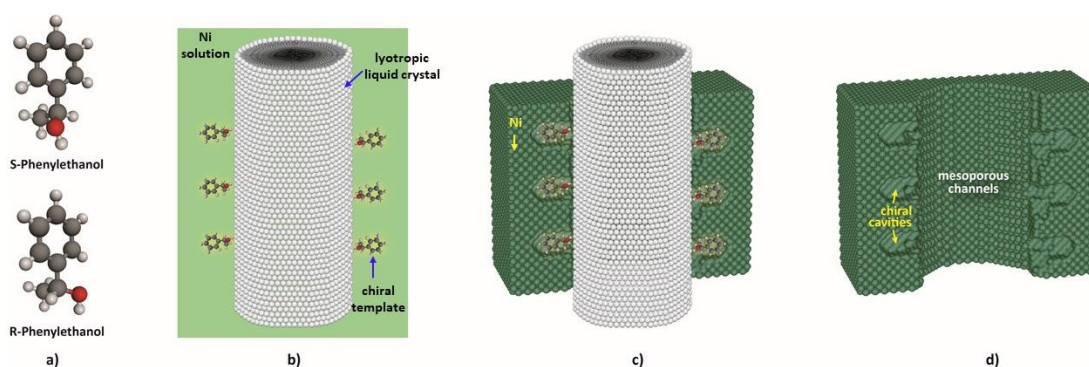
$$s.e.m. = \frac{S}{\sqrt{n}} \quad (1.3)$$

where S represents the standard deviation and n is the number of experiments

1.3. Results and discussion

Characterization

Chiral encoded mesoporous metal surfaces (CEMMSs), including platinum and nickel films, were successfully electrodeposited on a gold-coated glass substrate in the presence of metal salts (H_2PtCl_6 or $\text{Ni}(\text{OAc})_2$) and a self-assembled lyotropic liquid crystal (Brij C10) as presented in [Scheme 1.1](#).^[4, 5] [Scheme 1.1a](#) illustrates the molecular structure of both chiral template molecules, S-phenylethanol (SPE) and R-phenylethanol (RPE), which are the desired products obtained by the electroreduction of acetophenone. The fabrication of the chiral imprinted electrodes, includes as a first step the hydrogen bond formation between the hydroxy group of phenylethanol and the head groups of the lyotropic liquid crystal ([scheme 1.1b](#)). The hydrogen bonding allows the chiral template molecules to bind to the self-assembled hexagonal phase (H_1) of the non-ionic surfactant. Subsequently electrodeposition is performed to generate the metal around the templates as shown in [Scheme 1.1c](#). After removal of the templates, mesoporous structures with chiral cavities are obtained ([Scheme 1.1d](#)).



Scheme 1.1 Illustration of chiral imprinted mesoporous nickel film formation: a) the molecular structure of (R) and (S) phenylethanol; b) the self-assembly of the lyotropic liquid crystal in the presence of Ni salt; c) Ni electrodeposition in the presence of mesoporous template and chiral template; d) the chiral imprinted mesoporous nickel after template removal.

To study the morphology of chiral encoded mesoporous platinum, the electrodes prepared with various deposition charge densities were observed by scanning electron microscope (SEM). **Figures 1.7a** and **1.7b** show the cross-sectional SEM images of platinum films obtained with different charge densities, confirming the presence of uniform mesoporous platinum films on the gold substrate. The mesoporous structure of chiral imprinted platinum was confirmed by using a transmission electron microscope (TEM) as shown in the inset of **figure 1.7a**, revealing a uniform pore size distribution around 5 nm. The thickness of the chiral imprinted mesoporous Pt films was measured from the cross-sectional SEM images of the samples obtained using various deposition charge densities. As expected, the thickness of the prepared samples is proportional to the charge density as presented in **Figure 1.7c**. To evaluate the active surface of the prepared electrodes, cyclic voltammograms of chiral imprinted mesoporous electrodes were measured in 0.5 M H₂SO₄ in the potential range between – 0.2 V and +1.2 V vs Ag/AgCl (**Figure 1.7d**). In this range, cyclic voltammograms exhibit four distinct peaks, assigned to hydrogen adsorption (H_a), hydrogen desorption (H_d), oxidation of Pt and reduction of PtO_n. The remarkable increase of the active surface area of mesoporous platinum (blue) compared to the flat platinum electrode (red) is about 33.4 times. Moreover, the active surface area of non-imprinted films and chiral imprinted mesoporous platinum was compared, and no significant increase of surface area was observed as shown in **Figure 1.8**. This suggests that the high surface area can be predominantly attributed to the additional mesoporosity of the metal matrix.

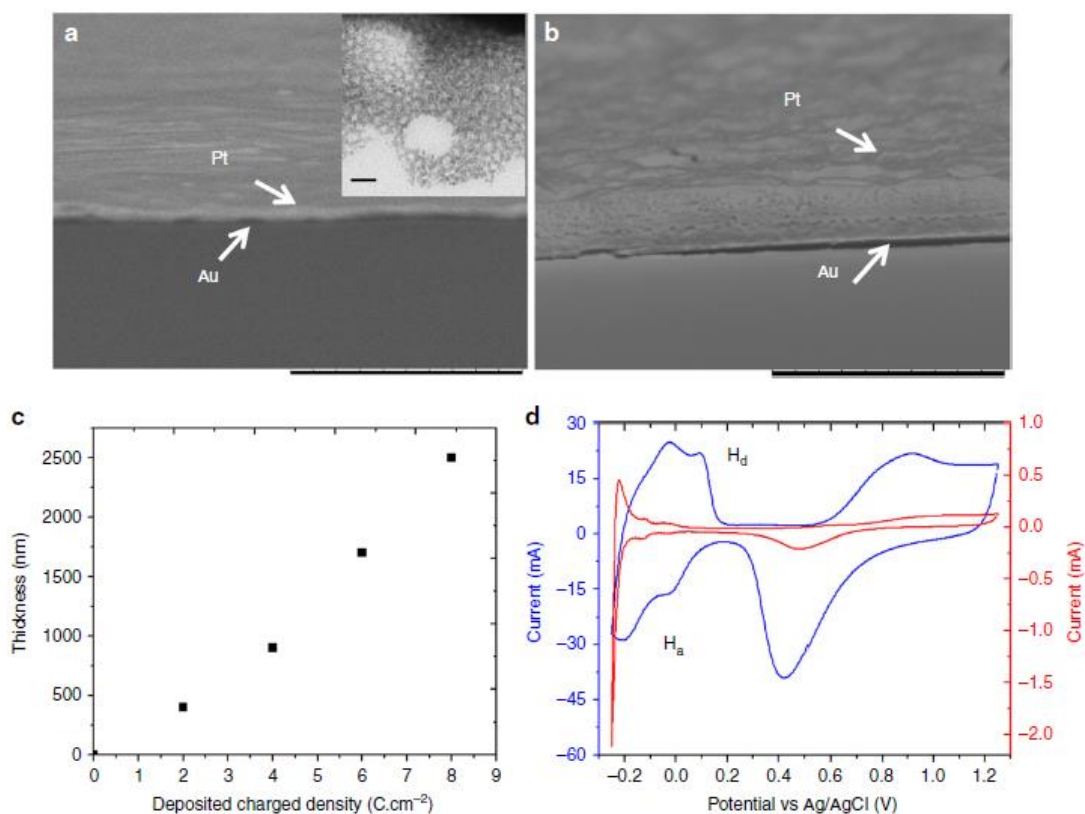


Figure 1.7 Structural characterization of chiral imprinted mesoporous platinum electrodes: a) and b) cross section SEM images of chiral imprinted platinum electrodes with injected charge densities of 2 and 8 C cm⁻², scale bar of 10 μm. The inset illustrates the mesoporous structure of the platinum matrix, scale bar of 20 nm; (c) thickness of the platinum film as a function of the deposition charge density and (d) cyclic voltammetry of flat platinum (red) and a chiral-encoded mesoporous platinum film with an injected charge density of 8 C cm⁻² (blue) in 0.5 M H₂SO₄ at a scan rate of 100 mVs⁻¹; H_a (hydrogen adsorption) and H_d (hydrogen desorption).

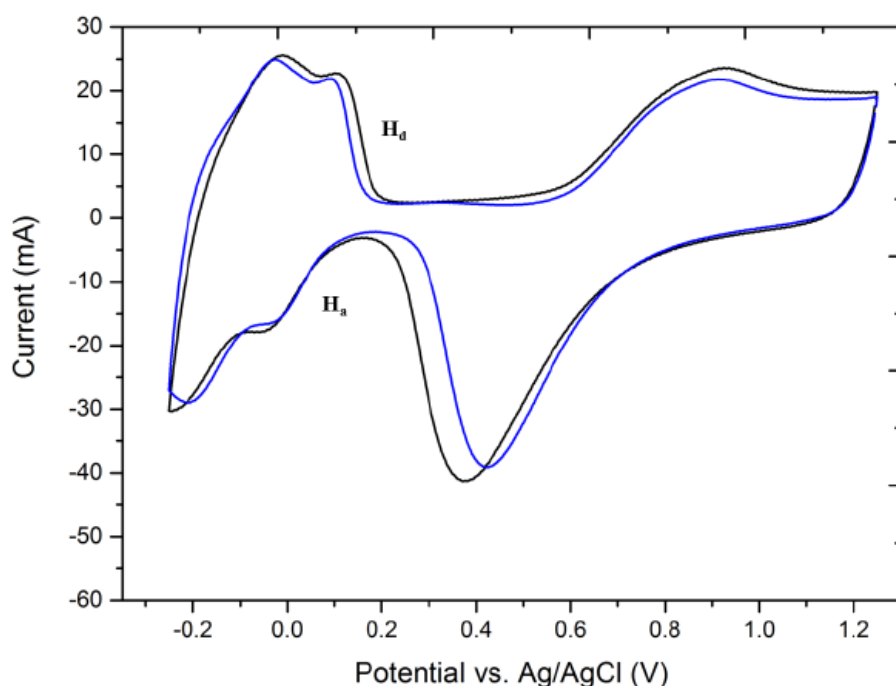


Figure 1.8 Cyclic voltammograms of non-imprinted mesoporous platinum (blue) and chiral imprinted mesoporous platinum (black) obtained with a deposition charge density of 8 C cm^{-2} , recorded in $0.5 \text{ M H}_2\text{SO}_4$ at a scan rate of 100 mVs^{-1} in the range from -0.25 to $1.25 \text{ V vs Ag/AgCl}$.

In addition, to validate the physical properties of non-noble metal electrodes, chiral imprinted mesoporous nickel, was characterized by various techniques, including SEM, TEM and CV as shown in **Figure 1.9**. **Figures 1.9a** and **1.9b** illustrate a smooth surface with a uniform thickness over the entire area of the prepared Ni electrode obtained for a deposition charge density of 4 C cm^{-2} as can be seen in the top and cross-sectional views. Obviously, the thickness of the mesoporous Ni films can be easily tuned by changing the electrodeposition charge density (**Figure 1.10**). The thickness of the films obtained for a deposition charge density of 1 , 2 and 4 C cm^{-2} correlates with 1.0 , 1.8 and 4.0 nm respectively. In order to confirm the mesoporous structure, created by the self-assembly of the lyotropic liquid crystalline phase, the TEM image of the chiral encoded mesoporous Ni electrode obtained with a charge density of 100 mC cm^{-2} reveals a uniform mesopore size distribution in the range

of 2.33 ± 0.22 nm (the inset of **Figure 1.9a**). The relationship between the relative roughness factor and the thickness of the nickel film measured by SEM (**Figure 1.9b** and **1.10**) is plotted as a function of charge density as shown in **Figure 1.9c**. Furthermore, to investigate the high active surface area of the mesoporous surfaces, the electroactivity of Ni in 1 M KOH was monitored by cyclic voltammetry in the reduction and oxidation region of nickel (250 to 350 mV and 100 to 250 mV, respectively) (**Figure 1.9d**). The current density of the oxide-layer formation relates to the active surface area of Ni, obtained for various deposition charge densities. These observations indicate an increase of the relative roughness factor of chiral imprinted Ni films as a function of film thickness. The relative roughness factors of the electrodes prepared with deposition charge densities of 1, 2 and 4 C cm⁻² are about 28.3, 61 and 114.2, respectively. It is reasonable to conclude that the relative roughness factor is proportional to the film thickness and the injected charge density.

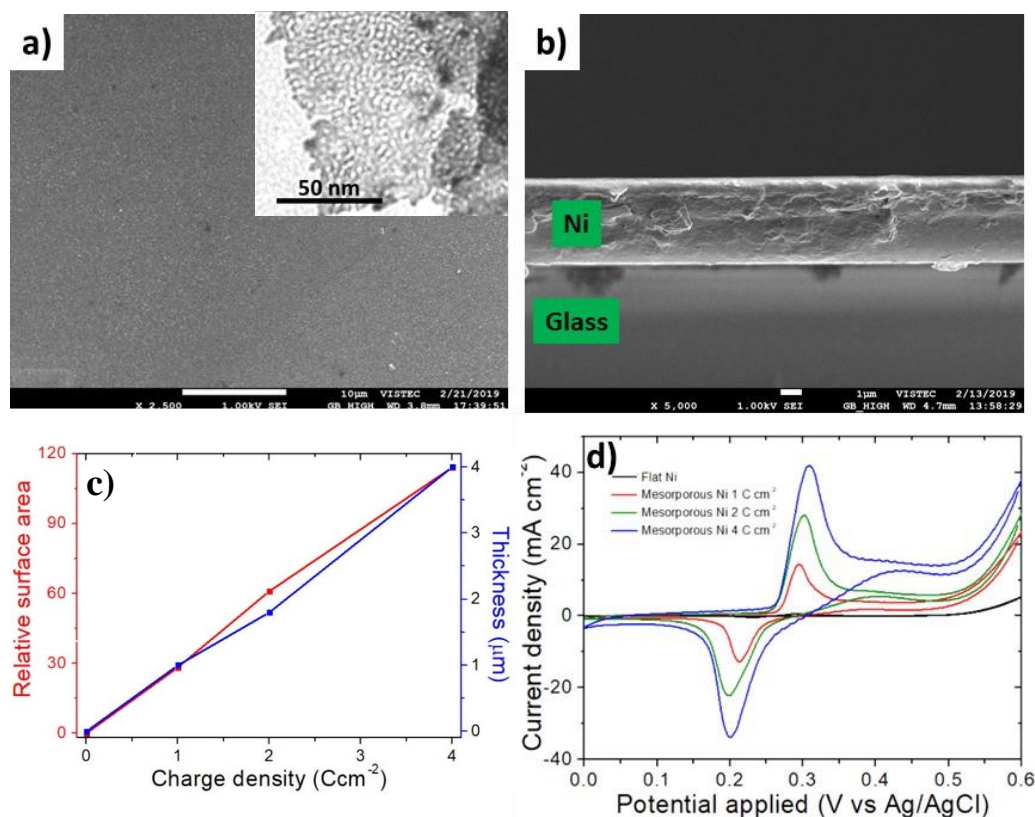


Figure 1.9 Structural characterization of chiral imprinted mesoporous nickel electrodes: a) and b) top view and cross section SEM images of a chiral imprinted nickel electrode with an injected charge density of

4 C cm⁻², scale bar of 10 μm and 1 μm, respectively; the inset illustrates the mesoporous structure of the nickel matrix, scale bar of 50 nm; (c) relative surface area and thickness of the nickel film as a function of the deposition charge density and (d) cyclic voltammograms of flat nickel and chiral-encoded mesoporous nickel films with various charge densities in 1 M KOH at a scan rate of 100 mVs⁻¹.

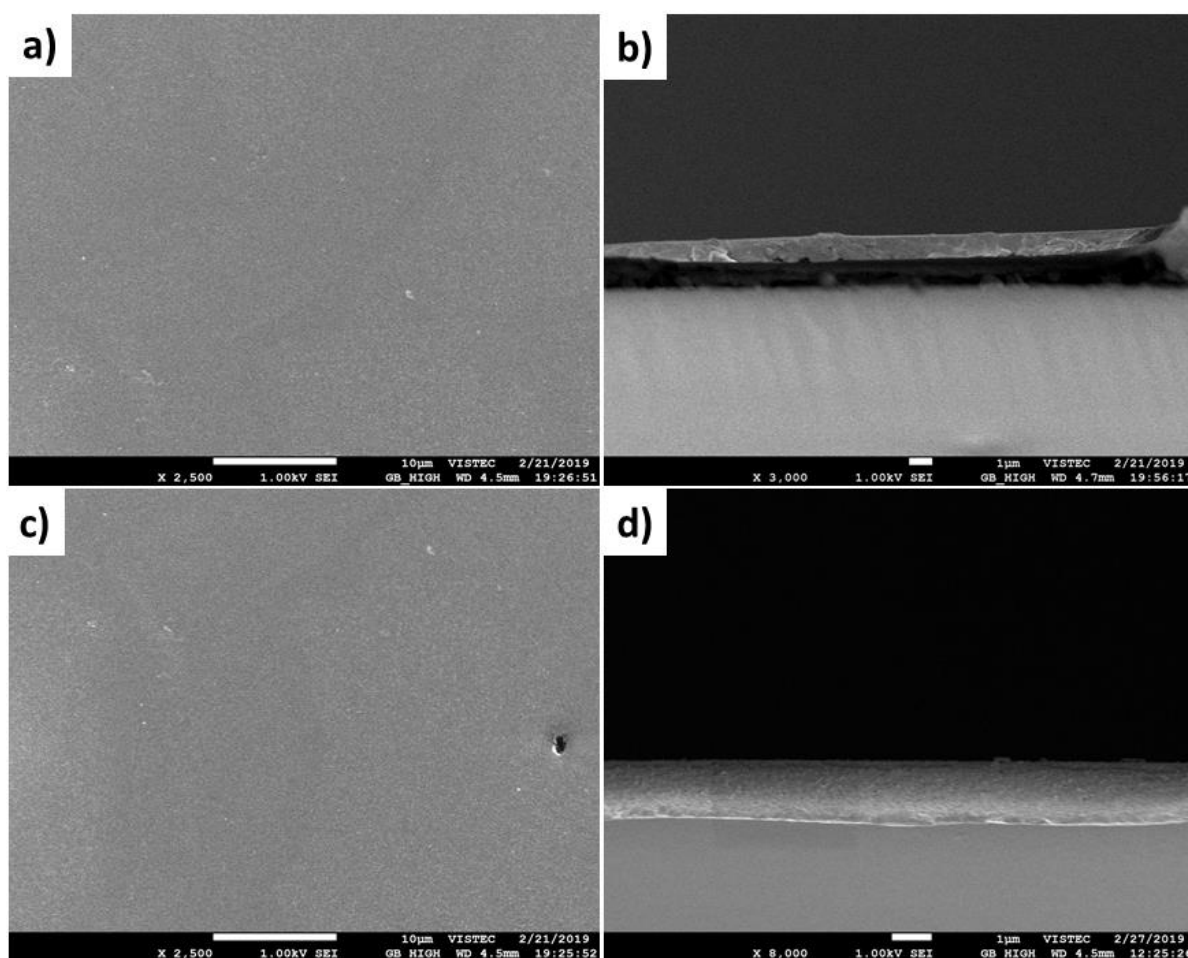


Figure 1.10 SEM images of mesoporous nickel electrodes imprinted with S-PE obtained with various injected charge densities: (a-b) 1C cm⁻²; (c-d) 2 C cm⁻² with a scale bar of 10 μm (top view) and 1 μm (cross-section).

Prior to the study of the enantioselective recognition properties of chiral imprinted metals, the complete removal of chiral template was confirmed by two

independent methods: (i) examining the amount of removed chiral template as a function of rinsing time by UV-VIS spectroscopy; (ii) monitoring the electrooxidation current of remaining chiral compounds by DPV. **Figure 1.11a** illustrates the UV-Vis spectra of the washing solutions as a function of rinsing times. The results clearly exhibit that there are no chiral template molecules leaving the platinum matrix after rising with water for 24 hr. In addition, the template removal from chiral encoded nickel films is confirmed and shown in **Figure 1.11b and 1.11c**. The series of UV-Vis spectra of the different washing solutions were recorded to confirm the complete template removal, and clearly shows that no template molecules are leaving the matrix after a rinsing time of 36 h (see in **Figure 1.11b**). In addition, to further confirm the removal of chiral molecules, differential pulse voltammograms (DPV) of the chiral imprinted mesoporous Ni after washing for 36 h in supporting electrolyte (50 mM HCl) was carried out in the potential range from 400 to 530 mV vs. Ag/AgCl as illustrated in **Figure 1.11c**. The current density of PE oxidation was background subtracted from 410 to 530 mV due to the interference with Ni oxidation.

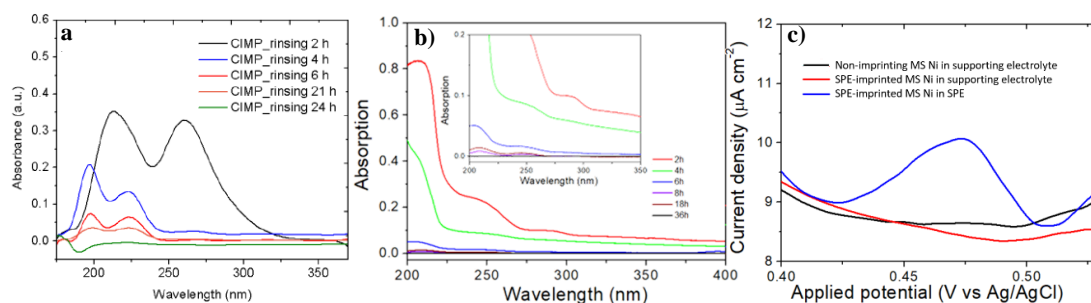


Figure 1.11. Investigating template removal of the prepared electrodes; a) and b) absorption spectra of the washing solutions when cleaning chiral platinum and nickel electrodes, respectively and c) differential pulse voltammetry (DPV) of the cleaned electrode in pure supporting electrolyte (red curve) compared to a non-imprinted electrode (black curve) and an electrode in S-PE solution (blue curve).

Enantioselective recognition of chiral compounds at chiral imprinted mesoporous metals surfaces.

In order to illustrate the enantioselective properties of chiral encoded metal films, DPV was used for obtaining the enantioselective electrooxidation of phenylethanol enantiomers at these metal surfaces (see in [Figure 1.12](#) for platinum electrodes and [Figure 1.13](#) for nickel electrodes). The used potential window for chiral imprinted platinum and nickel was limited by the oxidation of the metal causing eventually a rearrangement of the chiral cavities, leading to a destruction of the chiral information encoded in the prepared electrodes. The limiting potentials for platinum and nickel in DPV are in a positive range up to +0.6 V and +0.58 V vs Ag/AgCl, respectively. As expected, identical DPV current densities are obtained for the electro-oxidation of (S)-PE (red) and (R)-PE (blue) for non-imprinted mesoporous Pt and Ni, confirming no chiral recognition as illustrated in [Figure 1.12a](#) and [Figure 1.13a](#). For the chiral imprinted platinum electrode, a more pronounced signal of (R)-PE compared to (S)-PE could be obtained when the electrode is encoded with (R)-PE as shown in [Figure 1.12b](#). In strong contrast, the current of PE oxidation for (S)-PE encoded platinum in (S)-PE is higher than in a (R)-PE solution ([Figure 1.12c](#)). This proves that the chiral recognition corresponds to the encoded chiral information. In the case of chiral imprinted mesoporous Ni, a similar recognition ability is observed ([Figures 1.13b](#) and [1.13c](#)). Mesoporous Ni imprinted with (S)-PE exhibits a more pronounced signal for (S)-PE (red) compared to (R)-PE (blue). In contrast, the one imprinted with (R)-PE shows a significantly higher signal for (R)-PE (blue) compared to (S)-PE (red). These observations clearly confirm the presence of chiral footprints in the Ni matrix even after removal of the chiral template. However, due to the easy oxidation of Ni, it is difficult to retain the chiral feature while going to higher positive potentials.

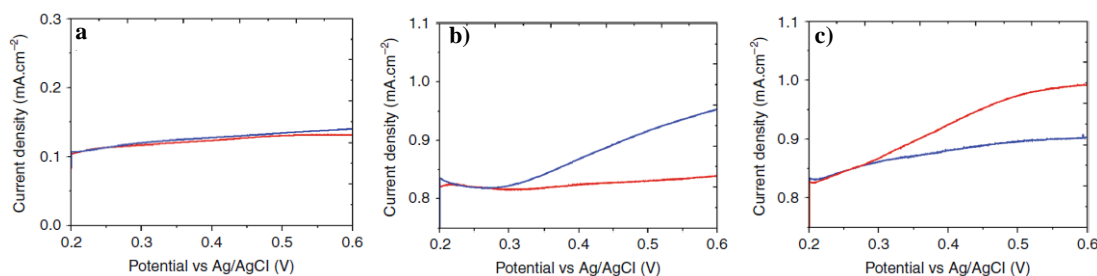


Figure 1.12 DPV of electrooxidation of (R)-phenyl ethanol (red) and (S)-phenyl ethanol (blue) in 50 mM HCl as a supporting electrolyte with different electrodes: a) non-encoded mesoporous platinum; b) and c) chiral mesoporous platinum encoded with (R)-PE and (S)-PE, respectively. All electrodes were prepared using a charge density of 2 Ccm^{-2} and a PE/PtCl_6^{2-} ratio of 0.05 for encoding the electrode.

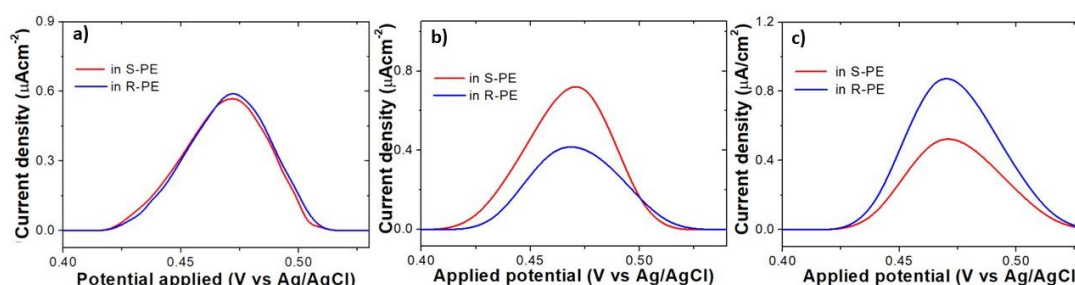


Figure 1.13 DPV of electrooxidation of (R)-phenyl ethanol and (S)-phenyl ethanol in 50 mM HCl supporting electrolyte with different electrodes: a) non-encoded mesoporous nickel; b) and c) chiral mesoporous nickel encoded with (S)-PE and (R)-PE, respectively.

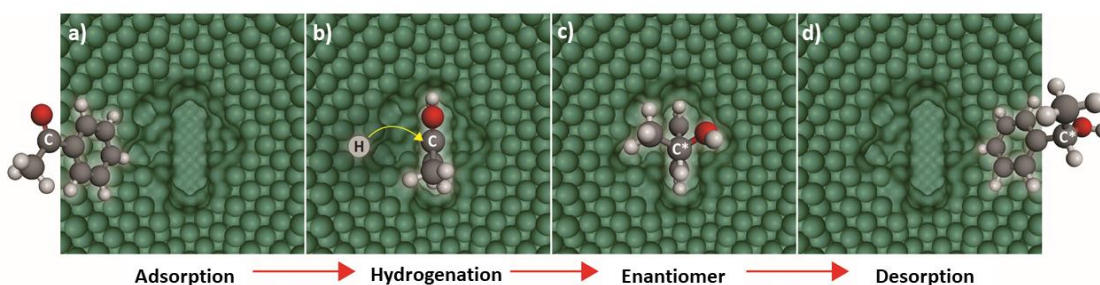
Asymmetric synthesis of chiral compounds at chiral imprinted mesoporous metal surfaces

In previous reports, enantioselective electrosynthesis of chiral compounds from a prochiral molecule at chiral encoded mesoporous platinum surfaces has been described.[3] As mentioned above, imprinting chiral molecules results in retaining chiral information in the metal matrix, and finally can result in a significant enantioselectivity during the synthesis of chiral compounds. Here we describe two approaches in order to improve the performance of these electrodes for electrosynthesis: (i) enantioselective synthesis via pulsed electrochemistry with a chiral encoded mesoporous platinum electrode and (ii) extending the scheme to chiral imprinted mesoporous non-noble metal surfaces.

In order to investigate electrochemical synthesis, the formation of phenylethanol from acetophenone was chosen as a model reaction because it has a simple molecular structure and is also present in large portions in bio-oil

(up to ~27 wt%).[116] Moreover, the hydrogenation product of acetophenone can be used as an intermediate for synthesizing various chiral compounds for pharmaceutical applications.[117]

During the enantioselective synthesis of chiral compounds, the first step is the oriented adsorption of acetophenone in the chiral cavities. Subsequently, its keto group ($C=O$) is partially reduced as can be seen in **Scheme 1.2a**. Due to the asymmetric environment of the chiral cavity, a chiral product, which has an identical spatial configuration with respect to the encoded chiral information, is selectively produced during the hydrogenation step (**Scheme 1.2b** and **2c**). Finally, the chiral product is released from the cavity as represented in **Scheme 1.2d**.

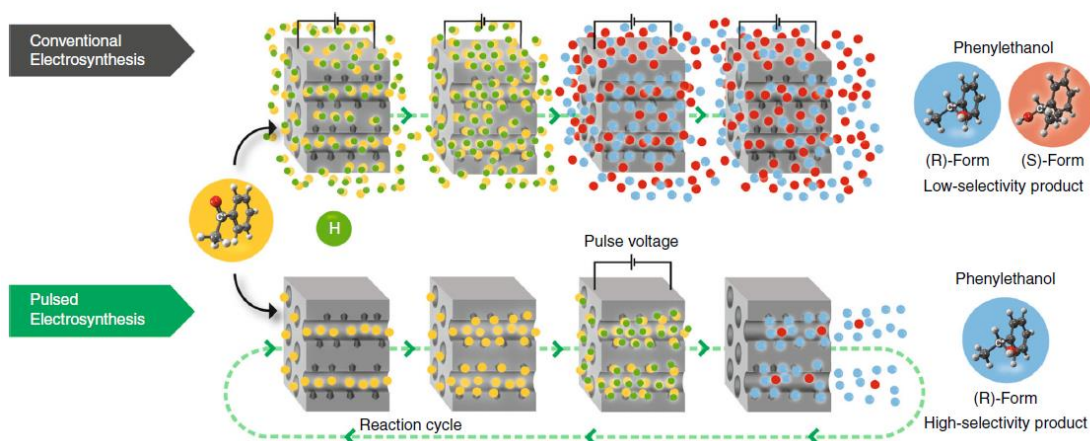


Scheme 1.2 Electrosynthesis of enantiomeric phenylethanol via hydrogenation of acetophenone: a) adsorption of the prochiral precursor in the imprinted cavity; b) selective hydrogenation of acetophenone inside the chiral cavity; c) chiral product obtained after hydrogenation; d) molecular desorption of phenylethanol from the cavity.

In order to improve the enantiomeric excess of the electrosynthesis the possibility of using a pulsed electrochemical technique has been explored. In conventional electrosynthesis, potential is continuously applied to the chiral metal phase. However, the %ee is not very high because hydrogenation of prochiral molecules can also occur at the non-imprinted sites and especially at the external surface of the electrode. Therefore, in order to increase the proportion of enantioselective product, we propose to apply the potential only

for a short time, followed by a relaxation period without applied potential. A comparison of the two strategies is schematically shown in [Scheme 1.3](#).

In the case of traditional electrosynthesis, acetophenone (yellow dots) can combine with hydrogen (green dots) inside the chiral cavities and at the outer surface of the electrode. This results in low enantiomeric excess of either (R)- or (S)-PE (blue and red dots, respectively) depending on the encoded enantiomer. Interestingly, a significant increase of the enantioselective properties can be obtained when a pulsed potential is used instead of the steady state experiment. During the relaxation period, fresh prochiral molecules can diffuse into the mesopores and adsorb in the chiral cavities. Subsequently, when a potential pulse of appropriate amplitude and duration is applied, hydrogenation of the prochiral molecules occurs preferentially in the asymmetric chiral cavities. After that, when the applied potential is switched off, the synthesized chiral product can leave the matrix and fresh reactant enters again the chiral cavities. By repeating the above-mentioned procedure for many cycles, the preferentially formed enantiomer accumulates in the bulk solution. Remarkably, pulsed electrochemical synthesis can significantly reduce the amount of unwanted product. The interference of electroreduction at the external surface can be minimized by fine-tuning the pulse duration and the relaxation time. However, for a given overall reaction time, the quantity of converted molecules is much smaller and the global synthesis time is much longer compared to conventional electrosynthesis.



Scheme 1.3 Comparison of the two strategies of enantiomeric synthesis. The prochiral precursor (yellow dots) enters the metal matrix and reacts with hydrogen (green dots). The products obtained from the electrosynthesis are (S)-PE (red dots) and (R)-PE (blue dots).

In order to obtain a highly enantioselective synthesis of phenylethanol enantiomers, an optimized potential of -450 mV vs Ag/AgCl for chiral imprinted platinum and of -550 mV vs. Ag/AgCl for encoded nickel was applied for the reduction of the prochiral C=O functional group of the acetophenone molecules. To avoid the interference of proton reduction that may generate hydrogen bubbles, eventually destroying the mesoporous structures, potentials in the range of -400 to -500 mV vs Ag/AgCl were tested for hydrogenation of acetophenone on chiral imprinted platinum (**Figure 1.14a**). For nickel films -450 to -550 mV vs. Ag/AgCl are a good compromise for the electroreduction of the C=O group (**Figure 1.14b**). The standard chromatograms of the chiral products (R)-PE, and (S)-PE, including prochiral reactant (acetophenone), show retention times of 13.5 (red), 14.5 (blue) and 10.1 min (black), respectively, as can be seen in **Figure 1.15**.

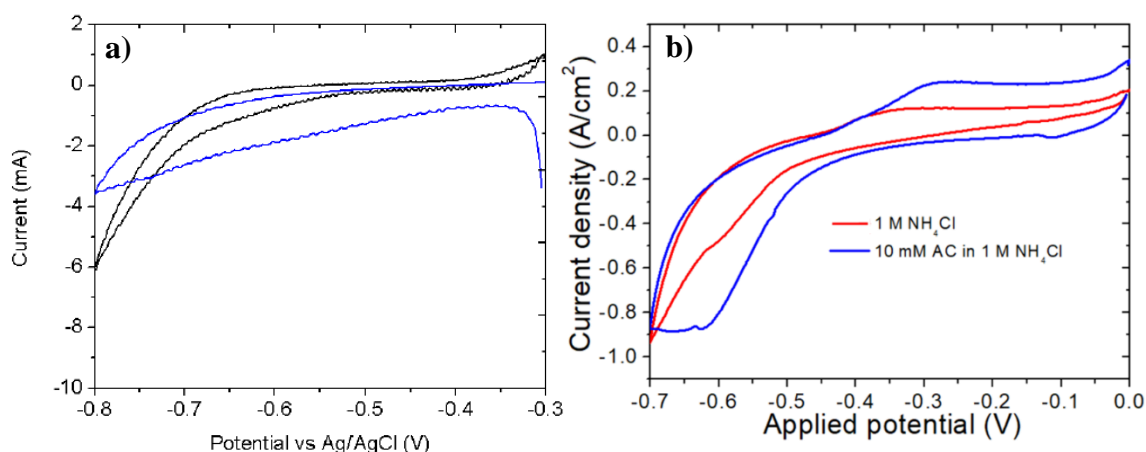


Figure 1.14 Cyclic voltammograms of flat electrodes obtained at a scan rate of 100 mVs^{-1} under various conditions: a) flat platinum electrode in 1 M NH_4Cl (black) and 43 mM acetophenone (blue); b) flat nickel electrode in 1 M NH_4Cl (red) and 10 mM acetophenone (blue).

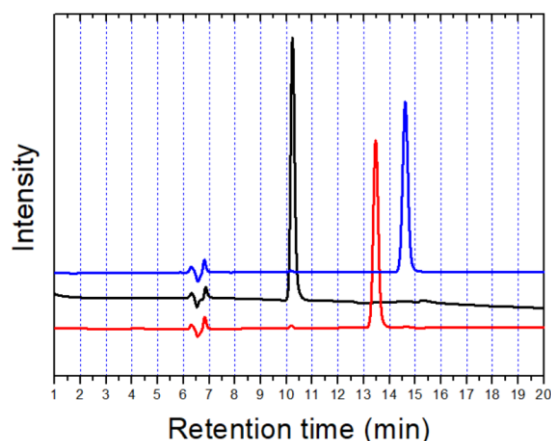


Figure 1.15 Standard chromatograms of the educt acetophenone (black), and the products (R)-PE (red) and (S)-PE (blue).

Figure 1.16a illustrates the HPLC chromatogram of the products obtained during the enantioselective electroreduction at chiral encoded mesoporous platinum electrodes. In order to enhance the enantiomeric excess, a potential of -450 mV vs. Ag/AgCl has been applied with different pulse durations. Interestingly, when a pulse duration of 60s is used, the enantiomeric excess is significantly improved (**Figure 1.16b**). For example, the enantiomeric excess can be increased from 13 % to 38 % with respect to conventional steady-state electroreduction. An even more pronounced enantioselectivity is obtained for shorter pulses of 30s, 10s and 2s. In the latter case, the enantiomeric excess reaches up to 90 % as shown in **Figure 1.16b**. From a theoretical point of view, a decrease in pulse duration plays an important role with respect to the competition between molecular transport effects in the mesopores and the reaction kinetics at non-selective sites. A short pulse duration combined with a relatively long relaxation time improves the contribution of diffusion inside the mesoporous matrix and allows filling the pores with fresh prochiral molecules from the bulk solution. The chiral nature of the products obtained during the synthesis can be confirmed by using circular dichroism (CD) measurements as shown in **Figure 1.17**. Opposite spectra are observed, meaning that the products are enantiomers.

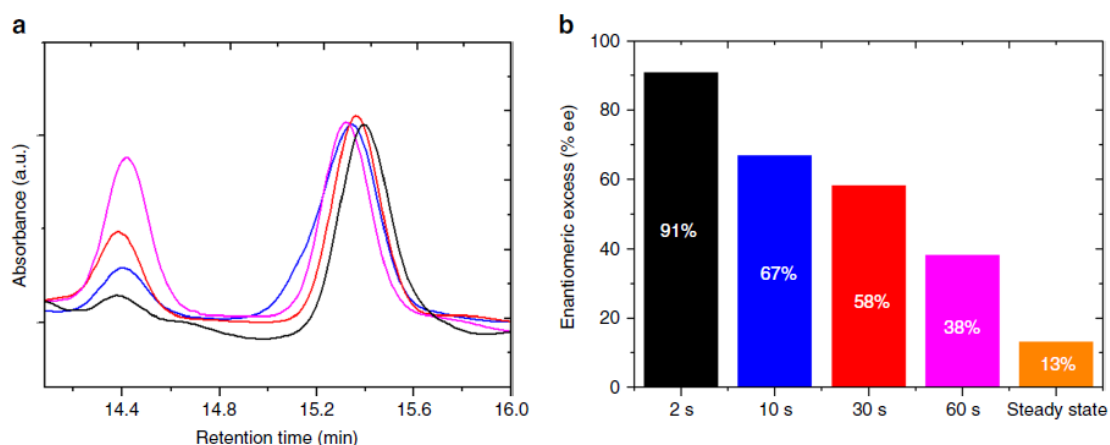


Figure 1.16 Results of the asymmetric synthesis when using chiral imprinted platinum electrodes: a) HPLC chromatograms of the electrosynthesis products obtained with (S)-PE imprinted electrodes in 10 mM acetophenone and 1 M NH_4Cl at a potential of -0.45 V vs Ag/AgCl for different pulse durations. The peak retention times of 13.5 and 14.5 min correspond to (*R*)-PE and (*S*)-PE, respectively. b) Histogram summarizing the enantiomeric excess (% ee) for various pulse times. Color codes present the different conditions of enantiomeric synthesis: classic electrosynthesis (orange); 60s pulses (pink) 30s pulses (red); 10s pulses (blue) 2s pulses (black).

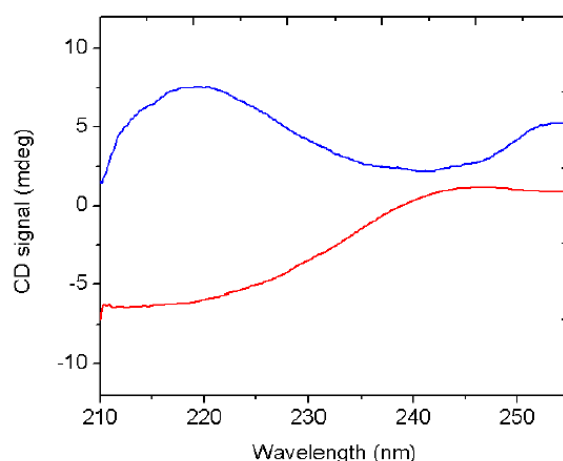


Figure 1.17 Circular dichroism (CD) spectra of the products obtained from electroreduction of acetophenone using a mesoporous platinum

matrix imprinted with (R)-PE (blue) and (S)-PE (red) for a pulse time of 5s.

As can be seen in **Figure 1.18**, the degree of enantioselectivity for the electroreduction of acetophenone at chiral imprinted mesoporous Ni surfaces can be also determined by high-performance liquid chromatography (HPLC). In a control experiment, using non-imprinted mesoporous Ni as a working electrode, no significant enantiomeric excess (-1.9%) was observed as illustrated in **Figure 1.18a**. Considering the error or the s.e.m. of the % ee value (± 3.61 %), calculated by **equation 1.3**, we can conclude that there is, as expected, no enantioselectivity. However, when using mesoporous Ni imprinted with (S)-PE, the enantiomeric excess reaches 23 % after 12h of reaction time for the conventional electroreduction method. The enantiomeric excess when using an electrode imprinted with (R)-PE is about -19 %. These observations confirm that it is possible to retain chiral information in the mesoporous Ni matrix, eventually leading to a moderately selective production of chiral compounds.

As mentioned above,[4] the concept of pulsed electrosynthesis can significantly improve the enantioselectivity due to the suppression of the interference of concomitant reactions at the non-imprinted sites located at the external electrode surface. Thus, we tested this concept also for chiral imprinted mesoporous Ni by applying the potential of -550 mV vs. Ag/AgCl with different pulse durations. Interestingly, when a pulsed duration of 30 s is chosen, the enantiomeric excess can be improved from 23 % to 45 % compared to conventional steady-state electroreduction (**Figure 1.18b**). An even more pronounced effect is observed for very short pulse durations of 10 s. In this case, the enantiomeric excess eventually reaches 80 % as shown in **Figure 1.18c**.

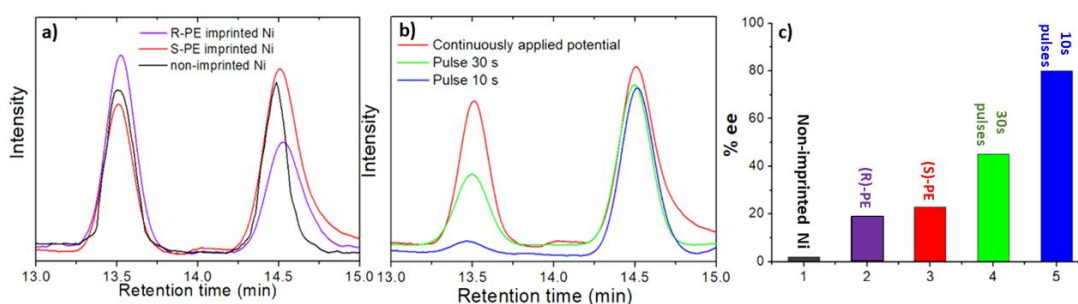


Figure 1.18 Chiral synthesis using chiral imprinted nickel as working electrode: a) and b) HPLC chromatograms of electrosynthesis products from 10 mM acetophenone and 1 M NH_4Cl as supporting electrolyte with (a) a constant applied potential of -0.55 V vs Ag/AgCl and (b) potential pulses of -0.55 V vs Ag/AgCl for an (S)-PE imprinted electrode. The peak retention times of 13.5 and 14.5 min correspond to (*R*)-PE and (*S*)-PE, respectively. c) The histogram summarizing the enantiomeric excess (%ee) for various pulse times. Color codes present the different conditions of enantiomeric synthesis: non-imprinted Ni (black); (*R*)-PE imprinted Ni (purple) and (*S*)-PE imprinted Ni (red) with continuously applied potential; (*S*)-PE imprinted Ni with 30s potential pulses (green) and (*S*)-PE imprinted Ni with 10s potential pulses (blue).

It is well-known that Ni is a soft non-noble metal, and therefore the chemical and mechanical stability of the chiral imprinted nickel films might be a critical issue.[118] It was found that when chiral imprinted mesoporous Ni electrodes were immersed into the supporting electrolyte without any applied potential under continuous stirring in nitrogen atmosphere, the mesoporous Ni layer was completely oxidized and removed after a day as can be seen from **Figure 1.19**. However, when a negative potential is constantly applied, the Ni layer is more stable via “cathodic protection”.[119, 120] This allows to envision still the use of such a soft metal in the frame of a reductive electrosynthesis experiment despite its intrinsic stability problems.

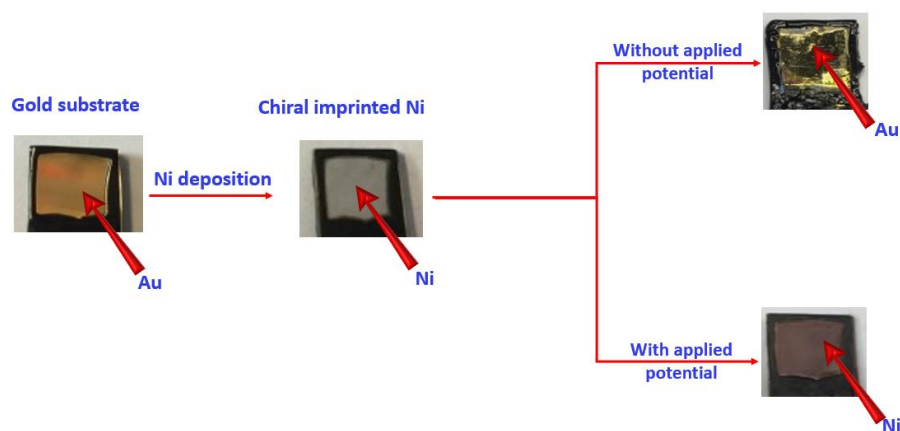


Figure 1.19 Mechanical stability of chiral encoded mesoporous nickel electrodes in supporting electrolyte with and without an applied potential of -0.55 V vs Ag/AgCl.

1.4 Conclusion

Chiral-encoded mesoporous Pt and Ni have been successfully prepared by the electrodeposition from Pt and Ni salts in the simultaneous presence of a lyotropic liquid crystal phase of non-ionic surfactant, Brij C10, and a chiral template, phenylethanol. The electrochemical properties of the prepared materials can be greatly improved compared to flat electrodes. This behaviour ultimately leads to an improved discrimination of (R)-PE and (S)-PE enantiomers, confirmed by DPV. In addition, the designed materials can be applied for the asymmetric electrosynthesis of phenylethanol from a prochiral starting compound (acetophenone). In conventional electrohydrogenation, only low enantiomeric excess was obtained due to the interference of hydrogenation on non-imprinted sites. However, the enantiomeric excess can be greatly improved when using the concept of pulsed electrosynthesis. By fine-tuning and optimizing the pulse duration, up to 90% and 80 % ee were obtained when using chiral imprinted platinum and nickel electrodes, respectively. This work significantly extends the application potential of enantioselective electrosynthesis with respect to the generation of high added-value chemicals and opens promising industrial perspectives for the future.

Chapter 2

Electrochemically fine-tuning of the enantioaffinity of chiral imprinted platinum surfaces for chiral discrimination and separation

2.1 Introduction

There are many types of molecules in nature having a chiral character. Although enantiomers usually have the same physical and chemical properties, very different biological activities are often observed. For example, in a biological environment one enantiomer usually presents a positive effect, whereas the other one might even be toxic. Therefore, the development of chiral technologies to obtain pure enantiomers is the main challenge for pharmaceutical applications.[121-123] Regarding chiral technologies, there are many approaches focusing on the asymmetric design of materials for different applications ranging from chiral analysis[124-131] to asymmetric synthesis[132-137] and chiral separation.[138-144] It has been found that chiral discrimination is generally considered as an important approach to obtain enantiomerically pure compounds (EPC) and to minimize unwanted products.[138-144] Therefore, the design and engineering of chiral stationary phases can improve their separation efficiency, eventually providing high performance tools for practical purposes.

For such applications, various asymmetric materials have been obtained by using different concepts including molecular imprinting,[130, 145-149], organometallic compounds,[133] metal organic frameworks,[150] and molecular grafting.[151, 152] Among these approaches, molecular imprinting is one of the most fascinating one, which employs enantiomer molecules as asymmetric templates to encode chiral information inside a bulk matrix.[102, 153] Molecularly imprinted polymers (MIPs) were the first examples of the molecular imprinting technology, and they have been widely used for mimicking biologically active sites inside the polymer matrices. For example, MIPs were

first studied and used as chiral adsorbent for chiral chromatography in 1978. [154] The chiral molecular template, 4-nitrophenyl- α -D-mannopyranoside, was covalently linked to a monomer, 1,2,3,4,6-di-o-(4-vinylphenylboronate), to form 4-nitrophenyl- α -D-mannopyranoside-2,3,4,6-di-o-(4-vinylphenylboronate). Interestingly, the MIP could be prepared and used as a chromatographic sorbent, providing specific cavities with chiral functionality. Furthermore, the prepared stationary phases were well suited for the separation of chiral compounds, even though broadened and tailing peaks were observed. Therefore, MIPs have been extensively explored as stationary phases in HPLC columns for racemic separation. For example, when using (R)-enantiomer-imprinted stationary phases, the (S)-enantiomer often elutes before the R-configuration. [155, 156] To further develop MIP materials, Yin and co-workers studied the enantiomeric separation of nateglinide and its enantiomer by comparing different chiral stationary phases including bulk and monolithic nateglinide-MIPs.[157] The recognition performance of the monolithic MIPs is remarkably higher than that of a column packed with bulk polymer. Although MIPs have been widely used as a stationary phase for chiral separation, the main drawback is the excessive peak broadening and tailing, often observed in the chromatograms when MIPs are employed as sorbent. [51]

In order to improve the separation efficiency of chiral compounds, MIPs were also employed as stationary phases in capillary electrochromatography. For instance, MIP was prepared using tert-butoxycarbonyl-tryptophan (Boc-Trp), acrylamide and ethylene glycol dimethacrylate as a chiral template, functional monomer and cross-linker agent, respectively, and subsequently the obtained material was used in a microfluidic device.[158] The resulting MIP-coated microchannels (MIP-MCMD) provide a complete baseline separation of racemic compounds with a short retention time (75 s), due to the large surface area and high number of chiral cavities in the MIP wall. However, the high pressure present in microfluidic channels results in leaching of the stationary MIP phase from the microchannel, thus reducing separation efficiency. Hence, a promising idea consist of integrating the MIP with a magnetic solid support in order to improve the stability of the MIP phase inside the microchannel.

Typically, the stationary phase was prepared using Fe_3O_4 nanoparticles and norepinephrine as the supporting substrate and the functional monomer, respectively. Various kinds of chiral templates to generate the chiral information were used including tryptophan, valine, threonine, ofloxacin and binaphthol. The results exhibited high separation performance and especially high stability of MIPs in the presence of the magnetic field.[159] However, due to the physical properties of the MIPs, in particular the shrinking and swelling of the chiral cavities after the template removal, as well as the poor accessibility of the internal part of the polymer matrix, a loss of chiral information is often a problem.[160, 161]

Regarding the disadvantages of conventional MIPs for chiral separation, alternative porous structures with chiral features imprinted in more rigid materials have been proposed.[162, 163] The new concept allows designing and selectively fine-tuning the interaction between guest molecules and chiral cavities. Recently, chiral imprinted mesoporous platinum films have been rationally designed and prepared based on the self-assembly of a lyotropic liquid crystalline phase in the simultaneous presence of enantiomers and a metal salt in order to create chiral cavities following a molecular imprinting approach.[2] Chiral encoded mesoporous metal surfaces (CEMMS) have been used in various applications ranging from chiral recognition, to electroanalysis[2, 39] and asymmetric synthesis.[3] Such a chiral imprinted mesoporous platinum exhibits a very high electrocatalytic surface area, promising enantiomeric recognition and acceptable asymmetric synthesis abilities. Interestingly, when chiral encoded mesoporous platinum is used for pulsed electrosynthesis, an enantiomeric excess above 90% was observed as explained in the previous chapter.[4] This implies that the chiral selective not only originates from the chiral information inside the mesopores, but also strongly relies on the operating conditions.

It is well known that the binding affinity of a chiral molecule on chiral surfaces can be significantly improved by fine-tuning their interaction. For example, capillary electrochromatography is a general technique of chromatographic separation in the presence of an electric field gradient.[164-

167] Because the applied potential allows inducing an electrostatic interaction, the additional force can therefore control the enantioaffinity of the racemic mixture for the surface of the stationary phase. The additional electrostatic force can significantly improve the chiral discrimination efficiency.[139, 165] Castellani and co-workers explored the electrostatic interaction between racemic 2-arylpropionic acids and an alkaloid-based stationary phase column. The results showed that the chiral separation efficiency strongly depends on the pH of the racemic solution, because the electrostatic interaction between stationary phase and racemic molecules becomes less important at pH >4 owing to the deprotonated functional group of the stationary phases.[168]

To combine the benefit of fine-tuning the electrostatic interactions with encoded mesoporous metal surfaces, we propose a new concept of fine-tuning the electrostatic interaction of chiral molecules with chiral-imprinted mesoporous metal surfaces. This can be achieved in microfluidic channels by adjusting the applied potential and the pH of the racemic solution. This eventually leads to a dramatically improved chiral resolution, even when using a stationary phase with only a short path-length.

2.2 Experimental section

Chemicals

Hexachloroplatinic acid hydrate ($\text{H}_2\text{PtCl}_6 \cdot x\text{H}_2\text{O}$), polyoxyethylene (10) cetyl ether (Brij C10), *L*- and *D*-tryptophan (Trp), *R*-, *S*- naproxen, 3,4-dihydroxy-*D*-phenylalanine (*D*-DOPA) and 3,4-dihydroxy-*L*-phenylalanine (*L*-DOPA), potassium iodide, iodine, hydrogen peroxide, sulfuric acid and sodium hydroxide were purchased from Sigma-Aldrich. Racemic tryptophan and hydrochloric acid were purchased from Alfa Aesar. Racemic naproxen was purchased from Merck. MilliQ water (resistivity: 18.2 M Ω cm) was used for the lyotropic liquid crystal preparation and chiral separation processes. All chemicals were directly used without additional purification.

Gold-coated glass substrate cleaning

Gold-coated glass slides were employed as a substrate for the electrodeposition of chiral encoded mesoporous platinum films. In order to clean the gold surface of the substrates (4.8 cm×2.4 cm), the surface of the gold-coated glass was immersed in piranha solution (H_2SO_4 and H_2O_2) for 30 min, resulting in organic impurities removal. Subsequently, the substrates were rinsed with MilliQ water (18.2 MΩcm) and then dried with nitrogen. The substrates were connected by soldering a normal wire and the geometric electrode surface area of about 4.0 cm × 0.2 cm was confined with scotch tape.

Electrodeposition of chiral imprinted mesoporous platinum microchannels

Chiral imprinted mesoporous platinum electrodes were prepared following literature procedures,[2, 3, 39] by electroreduction of a platinum salt in the simultaneous presence of a self-assembled lyotropic liquid crystal and the chiral template. In the present work, polyoxyethylene (10) cetyl ether (Brij C10) as a non-ionic surfactant and enantiomeric tryptophan were used as a mesoporegen and chiral template, respectively. To prepare plating mixtures for platinum deposition, the liquid crystal composed of 42 wt% Brij C10, 29 wt% chloroplatinic acid, 29% wt% MilliQ water and the desired amount of tryptophan template were combined. The resulting gel was mixed until becoming homogeneous. The viscous plating gel was carefully placed on the gold-coated glass, and then a platinum mesh was positioned at the top of the gel as a counter electrode. Ag/AgCl was used as a reference electrode in the electrochemical cell. A potential of -0.15 V vs Ag/AgCl was applied to the gold substrate for the reduction of the platinum ions with various charge densities in order to optimize the film thickness. After electrodeposition, all the prepared electrodes were rinsed with MilliQ water several times to remove the chiral template and lyotropic liquid crystal from the mesopores and chiral cavities.

Electrodes characterization

The surface morphology and the thickness of the chiral imprinted platinum obtained with various deposition charge densities were characterized by using a Hitachi TM-1000 tabletop electron microscope and JEOL, JSM-7610F, respectively. Furthermore, the mesoporous structure of the deposited platinum was confirmed by transmission electron microscopy (TEM) performed on a JEOL JEM-2010 and a JEOL JEM-2100 microscope. For chiral imprinted mesoporous platinum samples, the gold layer was removed by immersion in an aqueous solution composed of 4 wt% KI and 1 wt% I₂ for 20 min. The platinum film was then detached from the electrode surface and transferred into an ethanol solution. Subsequently the mesoporous film was transferred onto the TEM grid and dried at ambient temperature. The electrochemical characterization of chiral encoded mesoporous platinum films was performed using a μ AUTOLAB type III equipped with a three-electrode system. The prepared electrodes, a platinum mesh and Ag/AgCl (Sat. KCl) were used as a working, counter and reference electrode respectively. The surface area of the mesoporous platinum electrodes was measured by cyclic voltammetry in 0.5 M H₂SO₄ recorded at a scan rate of 100 mVs⁻¹ in the range of – 0.25 to 1.25 V vs Ag/AgCl.

Potential tuning on chiral imprinted platinum surfaces for chiral separation

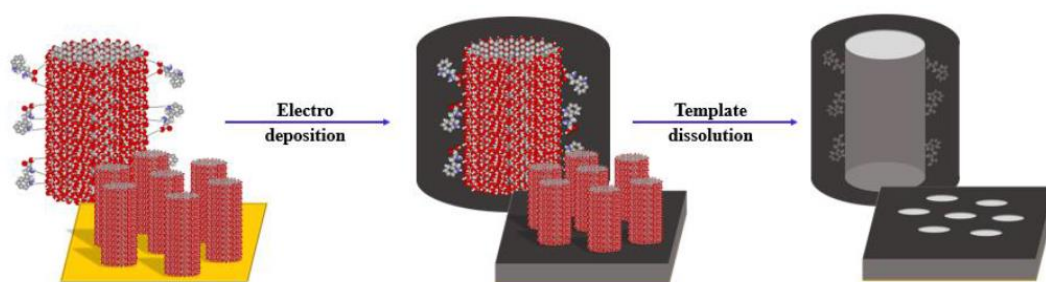
Chiral-imprinted mesoporous platinum was electrodeposited on the substrate and used as electrode. For the affinity fine-tuning, the potential was controlled by a potentiostat connected to the mesoporous stationary phase and to a silver wire located at the exit of the microchannel as pseudo reference electrode. The potential of the chiral stationary phase was tuned in the range from 0 to 0.3 V vs Ag. While applying the potential to the imprinted channel walls, 0.2 μ l of a 1 mM racemate solution is injected at the channel inlet. The racemic mixture is then transported through the channel with water (pH 10-11) at a flow rate of 0.5 ml hr⁻¹. After passing through the column, the different

constituents of the solution were detected at the channel outlet by fluorescence at 396 nm with a spectrophotometer connected to an optical fiber

2.3 Results and discussion

Characterization of chiral-encoded mesoporous platinum films

Tryptophan encoded mesoporous platinum films were successfully deposited on a gold-coated glass substrate in the simultaneous presence of platinum salt and a self-assembly of a lyotropic liquid crystal (Brij C10) as a stationary phase in a microfluidic channel. **Scheme 2.1** demonstrates the fabrication procedure of the chiral imprinted electrode comprising the following two steps. It starts in the first step with the self-assembly of the lyotropic liquid crystal, which interacts with chiral template molecules, *L*-tryptophan (*L*-Trp) or *D*-tryptophan (*D*-Trp) via a hydrogen bond interaction between the hydroxyl group of the chiral templates and the head group of surfactant. The concentration of the mesoporegen template was controlled in order to be in the range of the hexagonal phase (H_1). Consequently, platinum was electrodeposited around the chiral template and lyotropic liquid crystal to create enantioselective cavities and a mesoporous structure.



Scheme 2.1 Tryptophan-encoded mesoporous platinum preparation starting from the self-assembled lyotropic liquid crystal (red columns) interacting with chiral template on gold coated glass. Then platinum is electrodeposited through the template and in the last step the chiral template and surfactant are completely removed, leading to imprinted mesopores.

In order to investigate the textural properties of the chiral encoded platinum electrodes, various techniques have been used for revealing the surface morphology, the mesoporous structure, the electroactive surface area and the enantioselective recognition properties. The morphology of the imprinted electrode shown in **Figure 2.1a** presents a smooth surface in the entire area of the prepared Pt electrode obtained with an electrodeposited charge density of 8 C cm^{-2} . A constant film thickness of $\approx 2 \text{ }\mu\text{m}$ was obtained, which is suitable for using it as a chiral stationary phase in the microfluidic channel (**Figure 2.1b**). Indeed, the thickness of the prepared electrodes can be varied and optimized by adjusting the deposited charge density. For example, when using charge densities of 2, 4 and 8 C cm^{-2} , film thicknesses of 0.28, 0.58 and $1.04 \text{ }\mu\text{m}$ are obtained respectively (**Figure 2.2**). The presence of a mesoporous phase is confirmed by TEM images of the chiral mesoporous Pt electrode obtained with a charge density of 100 mC cm^{-2} . They reveal the presence of a uniform mesopore size of about 5 nm (**Figure 2.1c**).

In addition, to verify the high active surface area of the chiral imprinted mesoporous Pt electrodes, cyclic voltammetry in $0.5 \text{ M H}_2\text{SO}_4$ was performed in the range from -0.25 V to $+1.25 \text{ V}$ vs Ag/AgCl (**Figure 2.1d**). Typically, the CVs show four processes including hydrogen adsorption (H_a), hydrogen desorption (H_d), oxidation of Pt and reduction of PtO_n . CVs confirm that the active surface area of mesoporous platinum electrodes is much higher than that of flat platinum and the electroactive surface area increases with increasing charge density, as illustrated by a roughness factor of 16, 35 and 82 for a deposition charge density of 2 (green), 4 (blue) and 8 C.cm^{-2} (purple), respectively. The relationship between surface enhancement factor, measured by CV, and the thickness obtained for various injected charge densities was studied, and it was found that the gradual increase of surface area directly correlates with the injected charge densities (**Figure 2.2**). The linear relationship between surface area and film thickness is due to the identical structure and homogeneous deposit.

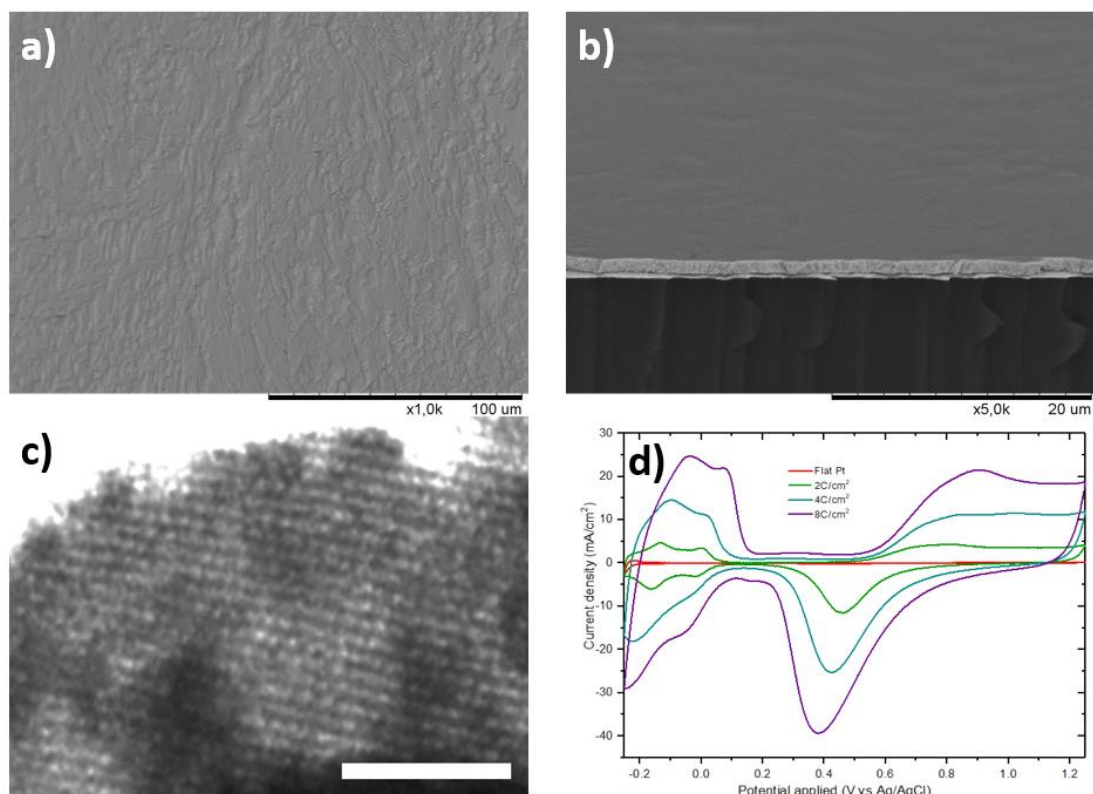


Figure 2.1 a) and b) SEM images of L-Trp encoded mesoporous platinum deposited with 8 C cm⁻² as top view and cross section, respectively; scale bars are 100 and 20 μm. c) TEM image of the platinum film; scale bar 50 nm. d) Cyclic voltammograms of various platinum electrodes in 0.5M H₂SO₄ at 100 mVs⁻¹ in the range from -0.25 to 1.25 V vs. Ag/AgCl. Key: flat platinum (red) and Trp-encoded mesoporous platinum, deposited with a charge density of 2 (green), 4 (blue), and 8 C cm⁻² (purple).

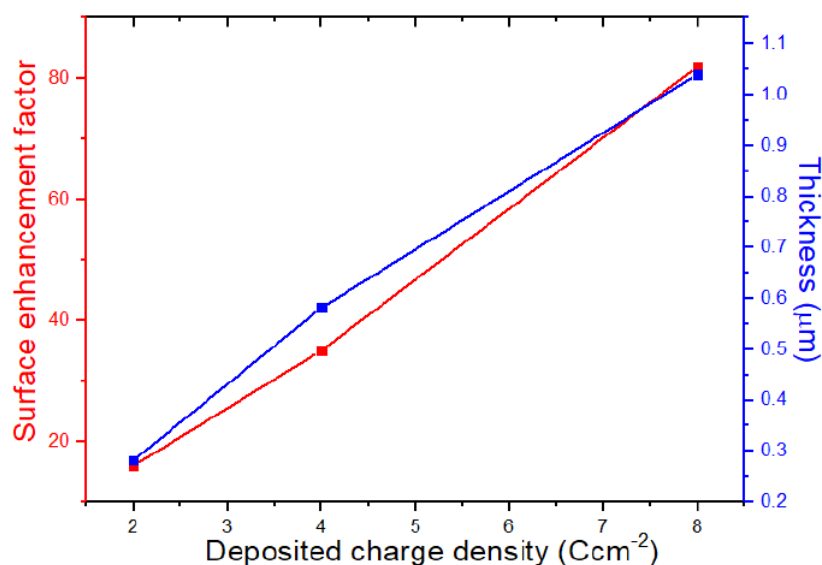


Figure 2.2 Surface enhancement factor and deposit thickness as a function of injected charge density during the electrodeposition of the mesoporous metal.

Prior to the study of the enantioselective recognition properties of chiral imprinted metals, the complete removal of mesoporegen and chiral template inside the mesoporous structure needs to be confirmed because the chiral template molecule and non-ionic surfactant can interfere with the measurement. UV-Vis spectroscopy is one of the suitable techniques to indirectly conclude regarding the tryptophan template left in chiral imprinted electrode. Typically, tryptophan exhibits an absorption peak at wavelengths between 215 and 260 nm. The washing solution was collected as a function of rinsing time and the spectra of [Figure 2.3](#) were recorded. They indicate that the chiral template was totally removed after washing the electrode for 60 min or more.

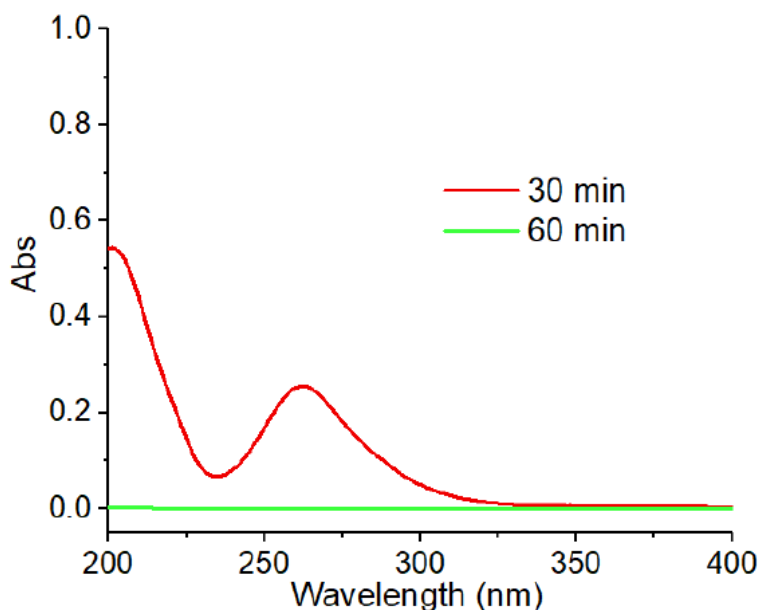


Figure 2.3. Absorption spectra of supernatant during the washing process after 30 (red) min and 60 min (green).

Enantioselective recognition of chiral compounds at chiral imprinted mesoporous metals surfaces

To reveal the enantioselective recognition properties of the chiral imprinted mesoporous platinum films, the oxidation signals of L-Trp and D-Trp were recorded using DPV in the potential range of Trp oxidation (0.7 to 1.2 V vs Ag/AgCl) (**Figure 2.4**). Chiral recognition is revealed by comparing the amplitude of current density in the Trp oxidation region. As anticipated, no chiral recognition is observed in the case of non-imprinted flat platinum (**Figure 2.4a**). In strong contrast to the non-imprinted electrode, the L-Trp-encoded mesoporous platinum electrode prefers to oxidize L-Trp rather than D-Trp, as shown by the higher oxidation signal in **Figure 2.4b**. On the other hand, for the platinum electrode imprinted with D-Trp, the amplitude of the current density in D-Trp solution is significantly higher than the one for the L-Trp solution (**Figure 2.4c**). It is therefore reasonable to confirm the presence of chiral information in the imprinted platinum electrodes. It is well known that at a high positive potential, the chiral information of the imprinted electrode can be destroyed. Obviously, when the imprinted platinum electrodes were first scanned in sulfuric acid in a potential range from -0.25 to 1.25 V vs Ag/AgCl, the current density

recorded subsequently for Trp oxidation is almost the same for both enantiomers (**Figure 2.4d**). These observations imply that there is no chiral information left after bringing the electrode to a high positive potential.

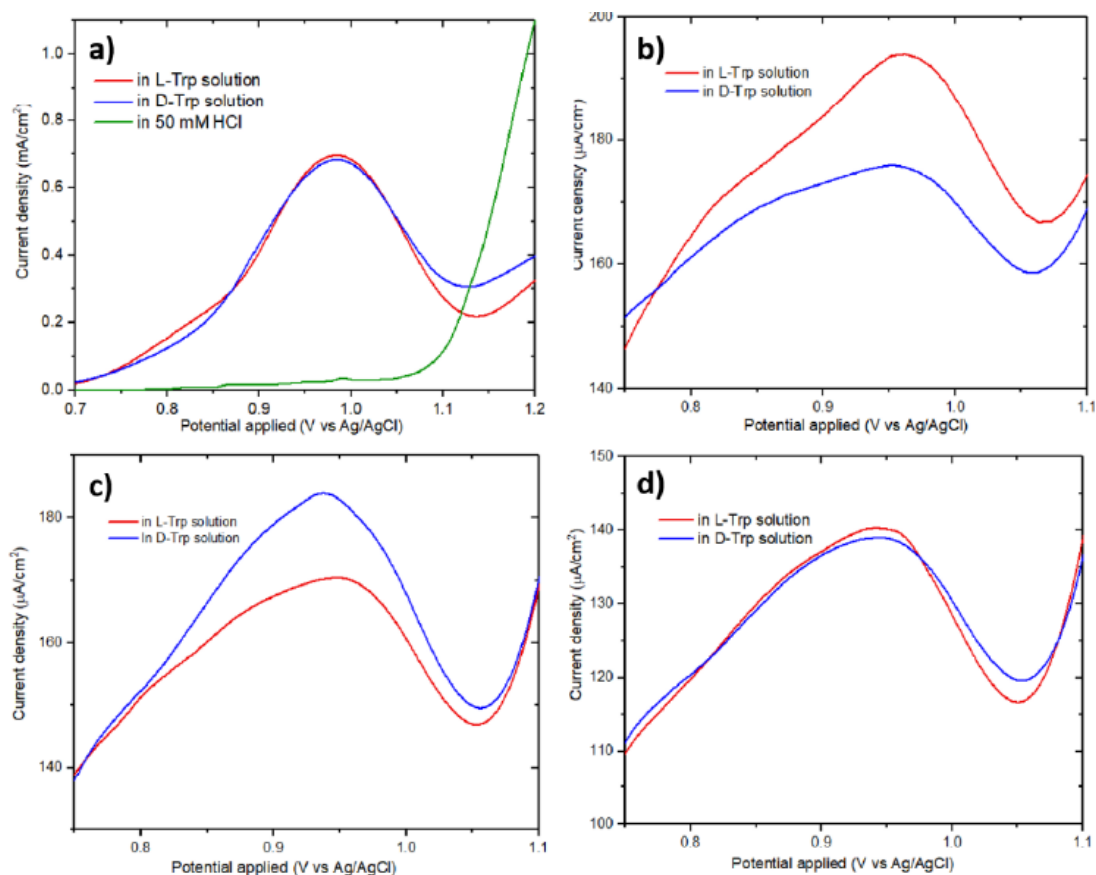


Figure 2.4. Differential pulse voltammetry (DPV) of various platinum electrodes in 4 mM L-Trp (red) and D-Trp (blue) using 50 mM HCL as supporting electrolyte (green is measured in supporting electrolyte only); (a) a flat platinum electrode, (b) L-Trp encoded mesoporous platinum, (c) D-Trp encoded mesoporous platinum and (d) L-Trp encoded mesoporous platinum after erasing the chirality by running a CV in 0.5 M H₂SO₄ between -0.25 and 1.25 V vs Ag/AgCl.

In addition, the imprinted platinum films also exhibit outstanding features for the enantioselective recognition of 3,4-dihydroxyphenylalanine (DOPA) as illustrated in **Figure 2.5**. As expected, undistinguishable DPV current densities for the electro-oxidation of L-DOPA (red) and D-DOPA (blue) are obtained on non-imprinted mesoporous Pt, confirming no chiral recognition as illustrated in

Figure 2.5a. For the chiral imprinted platinum electrode, a significantly more pronounced signal of L-DOPA oxidation with respect to D-DOPA oxidation can be obtained when an electrode is encoded by (L)-Trp as shown in **Figure 2.5b**. In contrast, the current density of D-DOPA is more pronounced than that of L-DOPA on D-Trp encoded platinum in (**Figure 2.5c**). This implies that the chiral encoded mesoporous platinum imprinted with tryptophan enantiomers has chiral affinity even for molecules with different molecular structures. As previously, enantioselective recognition was tested after erasing the chiral information (**Figure 2.5d**), exhibiting again identical current densities for both enantiomers.

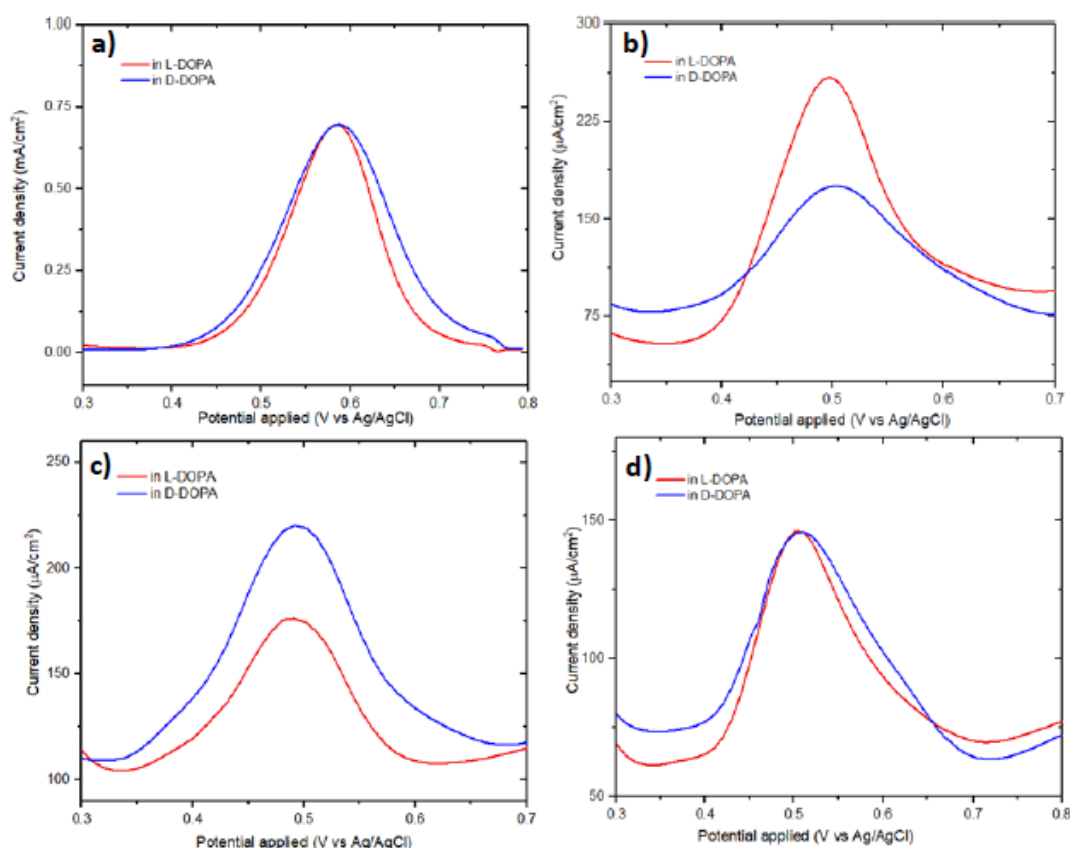


Figure 2.5. Differential pulse voltammetry (DPV) of various platinum electrodes in 4 mM L-DOPA (red) and D-DOPA (blue) using 50 mM HCL as supporting electrolyte; (a) a flat platinum electrode, (b) L-Trp encoded mesoporous platinum, (c) D-Trp encoded mesoporous platinum and (d) L-Trp encoded mesoporous platinum after erasing

the chirality by running a CV in 0.5M H₂SO₄ between -0.25 and 1.25 V vs Ag/AgCl.

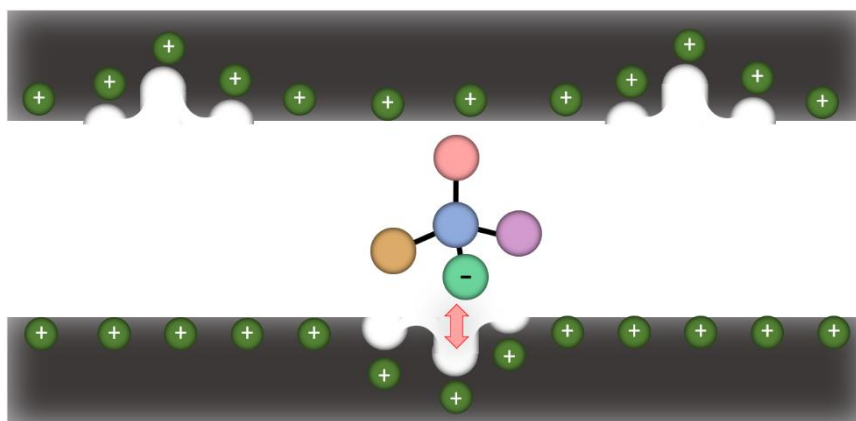
Chiral discrimination and separation

To illustrate the concept of fine-tuning the enantioaffinity of chiral molecules, the applied potential has been tuned at a chiral-encoded mesoporous platinum film used as a stationary phase and working electrode for chiral separation. The potential has been optimized to identify suitable conditions for the enantiomeric separation because at a very low positive potential only small electrostatic forces are present, and therefore the enantiomeric molecules are not able to get separated by the chiral electrodes. However, if the applied positive potential is too high, an oxidation of the chiral molecules and the platinum surface might occur, leading to a loss of chiral information of the imprinted cavities.

In the present case, tryptophan enantiomers were used as the chiral template because L-tryptophan (L-Trp) is a well-known natural essential amino acid, involved in protein synthesis and a precursor of the neurotransmitter serotonin, whereas the mirror enantiomer, D-tryptophan (D-Trp), is used in pharmaceutical applications as an intermediate in the synthesis of peptide antibiotics. Above the pK_a of Trp (9.39), the main portion of Trp is deprotonated and therefore negatively charged. The electrostatic interaction between a negatively charged molecule and the positively charged metal surface is illustrated in [Scheme 2.2](#). The electrostatic interaction is described by Coulomb's law in which the Coulombic force (F_E) depends on the potential applied to the chiral metal phase and the charge of the deprotonated molecule.

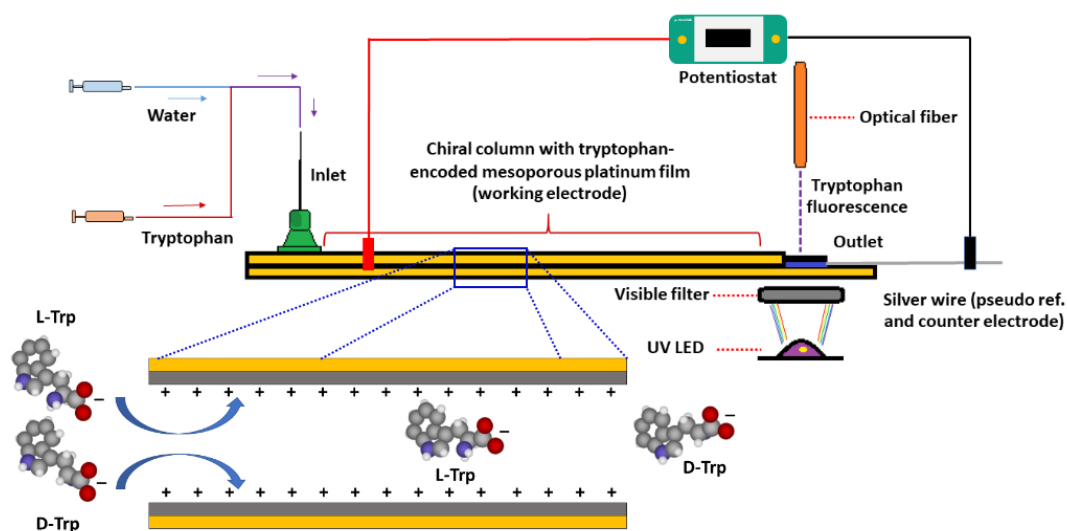
$$F_E = qE \quad (2.1)$$

with q being the charge of deprotonated racemate and E refers to the applied potential. Enantiomeric molecules with the right chirality should then interact in a favorable way with the imprinted cavities.



Scheme 2.2 An illustration of the electrostatic interaction of deprotonated Trp with a cavity in a positively charged mesopore of the microchannel.

To illustrate the benefits of the chiral imprinted metal films for chiral separation, the designed materials were electrochemically deposited as the stationary phase in the micro-fluidic channel. Interestingly, the interaction of the chiral molecules with the imprinted surfaces can be adjusted by applying a positive potential at the electrode surfaces as shown in [Scheme 2.3](#).



Scheme 2.3. A hyphenated microfluidic electrochromatography device with an L-Trp-encoded mesoporous platinum film as a stationary phase. The electrochemical potential of the stationary phase is controlled by a potentiostat.

When using L-Trp imprinted mesoporous platinum as a stationary phase and as a working electrode in a microfluidic device, as illustrated in [Figure 2.6](#), the applied potential can be controlled by a potentiostat with respect to a silver wire used as a counter and pseudo reference electrode. Deprotonated racemic Trp is injected at the inlet, with water as a mobile phase. The electrostatic force is generated by applying a potential to the chiral-encoded Pt film. The solution leaving the microchannel is studied by fluorescence at 396 nm with an optical fiber connected to a spectrophotometer using an excitation wavelength of 260 nm generated by a UV-LED. The absorption and emission spectra of tryptophan are shown in [Figure 2.7](#).

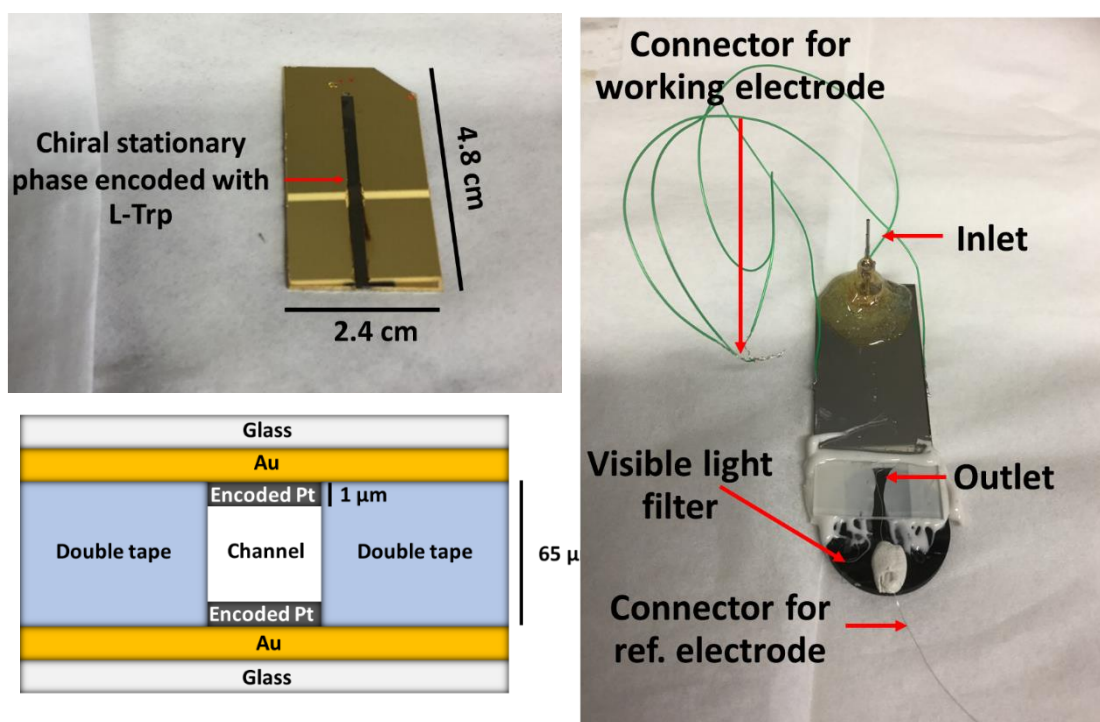


Figure 2.6 (a) Electrodeposition of a narrow strip of tryptophan encoded mesoporous platinum on a gold-coated glass slide. (b) Two plates prepared in this way are placed face to face and kept separated at a distance of 65 μm by positioning double-sided tape along both sides of the metal deposit. This also allows to seal the channel. (c) Global view of the final microfluidic device for chiral separation.

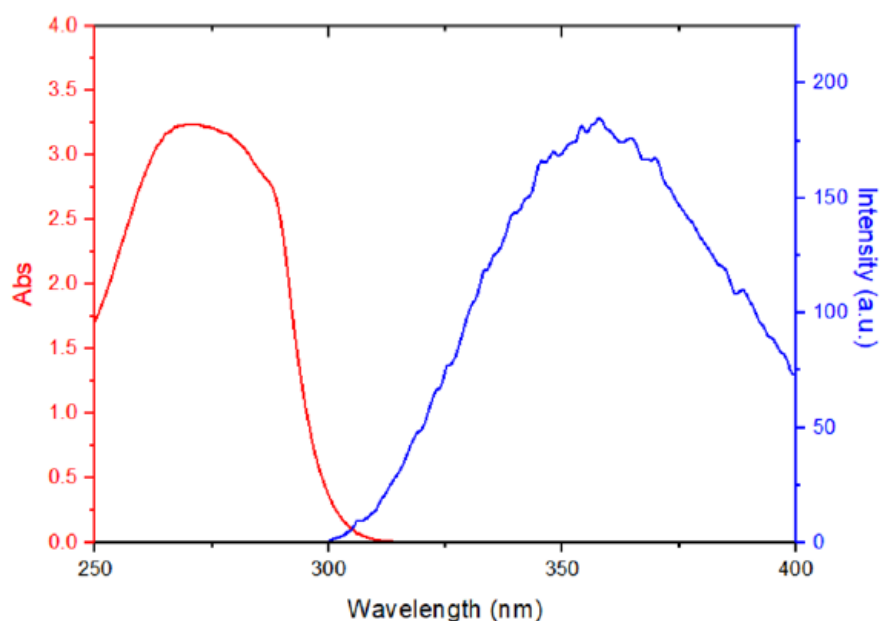


Figure 2.7. Absorption and fluorescence spectra of 1 mM tryptophan dissolved in water.

The applied potential was optimized in order to find a suitable condition for tryptophan separation using L-Trp encoded mesoporous platinum as a stationary phase as shown in [Figure 2.8](#). First, injection of the racemic mixture was carried out without applied potential as a control experiment at a flow rate of 0.5 ml min^{-1} of supporting electrolyte at pH= 9-10 as represented in [Figure 2.8a](#). As expected, a very broad peak was obtained after 300 s due to the overlapping between L-Trp and D-Trp. This implies that the interaction between the chiral compounds and the stationary phase are not strong enough to allow baseline separation. In contrast to this, the interaction between chiral stationary phase and racemic molecules can be enhanced by applying a positive potential of 200 mV vs Ag to the chiral metal phase as illustrated in [Figure 2.8b](#). This results in improving the separation, leading to two broad peaks. In addition, the retention time of the peak attributed to L-Trp is shifted by approximately 750 s when applying a potential of +200 mV vs Ag. Due to the presence of chiral cavities and electrostatic forces, the strong interaction of L-Trp with the imprinted surface results in a very significant prolongation of its retention time (peak at 1200s). In strong contrast, D-Trp is almost not affected within the error

bars of the measurement. When increasing the applied potential to +300 mV, the racemate solution is completely separated as shown in [Figure 2.8c](#), and the peaks of D-Trp and L-Trp are observed at ~500 and ~1400 s. However, the applied potential cannot be increased above 300 mV due to the risk of platinum oxidation and oxidation of deprotonated Trp in the channel which would result in losing chiral recognition.

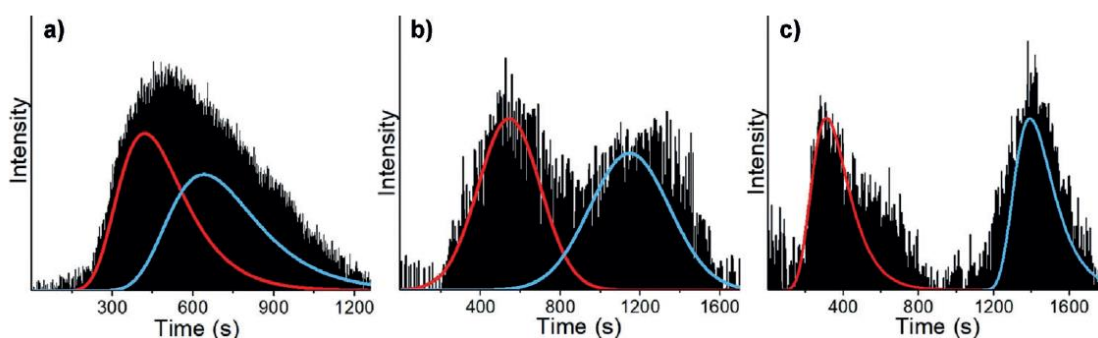


Figure 2.8 Electrochromatography of racemate Trp solutions with fluorescence detection at the microchannel outlet by an optical fiber for a L-Trp imprinted platinum layer. a) No applied potential; (b) 200 mV vs Ag; and (c) 300 mV (fresh).

To confirm the structural selectivity, standard solutions of L-Trp and D-Trp have been tested with respect to the retention times of the individual compounds at an applied potential of 300 mV vs Ag. As expected, when the stationary phase is imprinted with L-Trp, the chiral cavity prefers to interact with the right configuration (L-Trp), thus the opposite enantiomer (D-Trp) exhibits a short retention time (400s) as shown in [Figure 2.9a](#), while the retention time of pure L-Trp is around 1400s ([Figure 2.9b](#)). This confirms the peak assignment when injecting the racemic mixture.

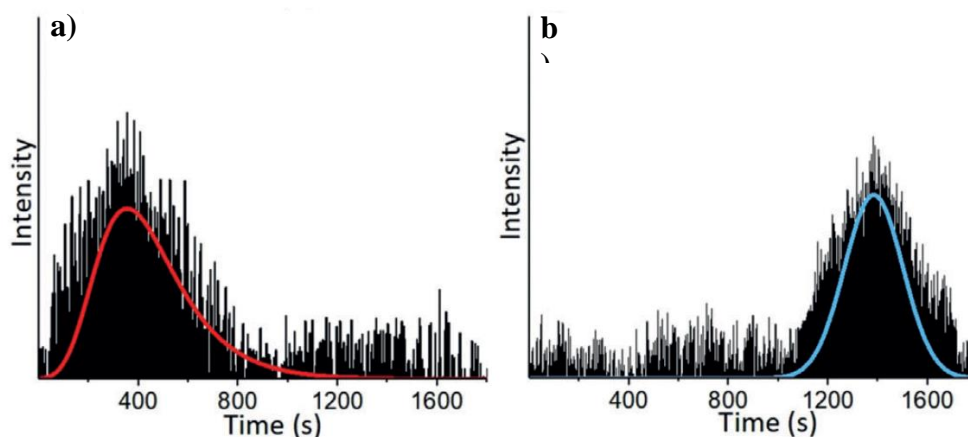


Figure 2.9 Electrochromatography of racemic Trp solutions with fluorescence detection at the microchannel outlet by an optical fiber for a L-Trp imprinted platinum layer. a) D-Trp; and b) L-Trp.

The atomic structure of the chiral imprinted column might be rearranged during the chiral discrimination process due to the electrochemical reaction on the surface, and therefore the stability of the stationary phase was studied by reusing the metal phase after keeping it for a month ([Figure 2.10](#)). Interestingly, although the chiral platinum phase exhibits a slightly lower separation efficiency, reflected by a reduction of the retention time of L-Trp from 1400 s to 1200, a clear separation of the two enantiomers is still observed.

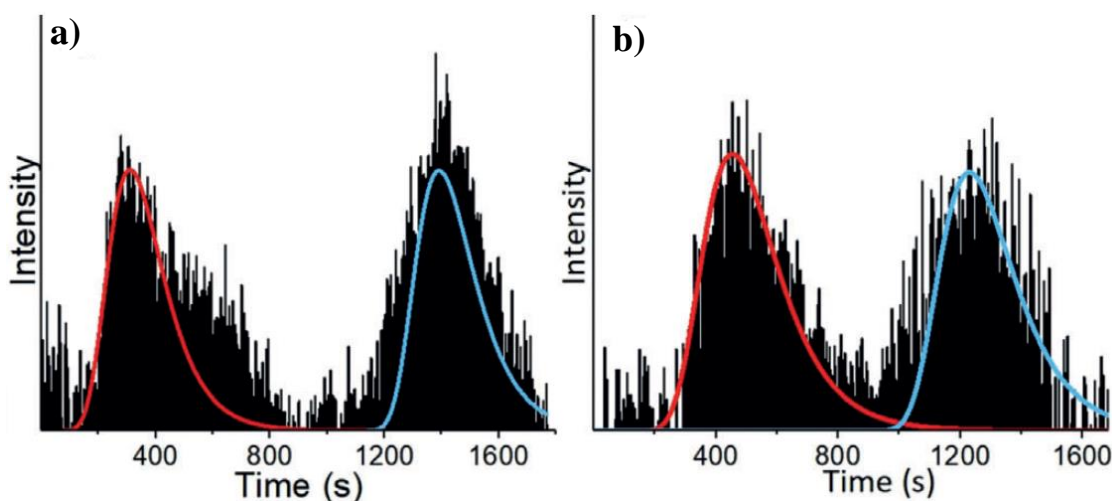


Figure 2.10 Electrochromatography of racemic Trp solutions with fluorescence detection at the microchannel outlet by an optical fiber for a L-Trp

imprinted platinum layer. a) freshly prepared layer of chiral platinum film; and b) after 1 month.

Previously, Yutthalekha and co-workers reported that a chiral electrode imprinted with one type of chiral molecule can be used for the chiral discrimination of other structures.[39] We have tested this feature in the present case of chiral separation using chiral encoded metals. In this case, the L-Trp-imprinted Pt film was also employed for chiral discrimination of other enantiomeric structures. Alternative amino acids are limited as candidates due to lower fluorescence signals which don't allow an easy detection. However, tyrosine (Tyr) is a suitable amino acid due to high fluorescence and a rather similar structure to that of tryptophan. Similarly, the peaks of Tyr racemate are undistinguishable when no potential is applied at the chiral metal phase, only a single broad peak indicates the presence of two enantiomers (**Figure 2.11a**). However, when an electric field is applied, a remarkable difference in retention time is seen in the form of two separated peaks (**Figure 2.11b**). Even without further optimization, almost baseline separation of the two enantiomers could be observed, indicating the versatility of the strategy to use chiral imprinted mesoporous metals as a stationary phase for the separation of various enantiomers.

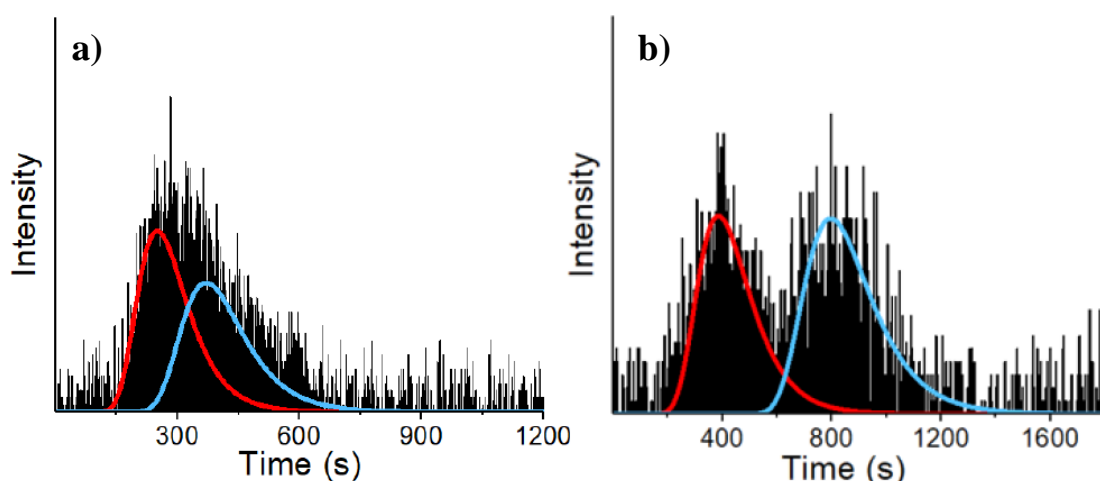


Figure 2.11. Record of the fluorescence signal at the microchannel outlet during tyrosine separation with a) no potential and b) +300 mV vs Ag applied to the L-Trp imprinted mesoporous platinum.

Moreover, it is interesting to check whether the chiral encoded mesoporous platinum can be used as a stationary phase for the separation of a real chiral pharmaceutical compound. Chiral naproxen was chosen as a pharmaceutical model compound because its two configurations exhibit totally different effects in the human body. For example, (S)-naproxen has been used to treat arthritis pain, whereas R-naproxen causes liver poisoning. Interestingly, the separation efficiency of these enantiomers can be improved by tuning the applied potential as shown in [Figure 2.12a](#), [12b](#) and [12c](#), corresponding to applied potentials of 300 mV and 400 mV vs Ag, respectively. *R*-naproxen seems to preferentially interact with the L-Trp cavities, observed at retention times of ~415 s (200 mV) and ~720 s (300 mV) compared with *S*-naproxen which leaves the microchannel at ~300 s (200 mV) and ~350 s (300 mV). These promising results reveal that this stationary phase not only can separate a model compound, but can be also applied to a real pharmaceutical product.

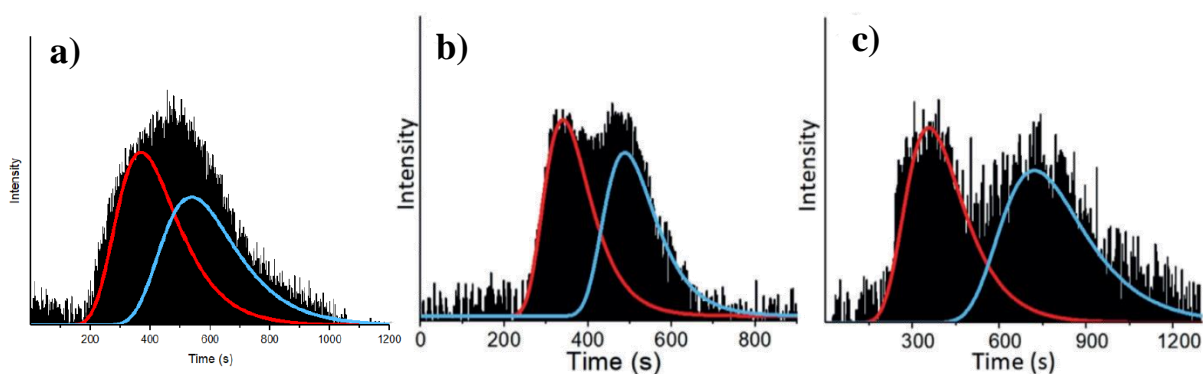


Figure 2.12. Separation of Naproxen enantiomers on an L-Trp-encoded platinum film at a) no applied potential b) +300 mV and c) +400 mV vs. Ag

2.4 Conclusion

In summary, chiral Trp-imprinted mesoporous platinum films have been successfully synthesized on gold-coated glass substrates in the simultaneous presence of a lyotropic liquid crystal phase and tryptophan as a chiral template. The electroactive surface area obtained from their mesoporous structure is

significantly improved compared to flat platinum. The prepared materials were used as a chiral stationary phase in a microfluidic channel. No chiral separation was observed when a racemic mixture of Trp was injected without applied potential. Interestingly, fine-tuning of the applied potential allowed optimizing the separation efficiency. Moreover, the Trp encoded platinum film could also be used as a stationary phase for chiral discrimination of other chiral structures including tyrosine and naproxen. Therefore this study presents a very promising and versatile strategy for the development of chiral separation technologies especially also because of the high stability and reusability of the metal matrix.

Chapter 3

Advanced design of chiral-imprinted platinum-polypyrrole hybrid films for enantioselective actuators of mandelic acid

3.1 Introduction

The design of materials with a sophisticated structure is of key importance for the development of nanotechnology. To design specific materials with molecular cavities, molecular imprinting technology is an advanced strategy, which is based on the generation of template-shaped cavities in material matrices to be used as molecular recognition sites.[125, 169] In this context, the development of molecular imprinted materials with chiral recognition sites is an extremely interesting topic because many pharmaceutical compounds usually are chiral molecules, in which one enantiomer has the desired effect in biological systems, however, the opposite enantiomer can even exhibit negative effects, and thus, obtaining only one specific enantiomer is highly desirable.[2, 170]

Generally, the molecularly imprinting approach has been widely focusing on the design of chiral recognition sites in soft matrices such as polymers, namely molecularly imprinted polymers (MIPs). They are formed by the self-assembly of functional monomers around the template or imprinting agent, followed by cross-linking of the monomer to form a film gel.[125, 169, 171, 172] Up to date, MIPs have been widely developed in chiral imprinting technologies due to a straight-forward preparation method and cost-effectiveness. These imprinted polymeric materials have been used as suitable candidates in various applications ranging from chiral synthesis,[3-5] separation of racemates,[6] enantiomeric analysis[2, 39] and osmosis,[161, 173] to nanofiltration[174] and electrodialysis.[169] In particular, in chiral sensing, materials and surfaces need to be engineered in such a way that they exhibit a specific enantioselective property.[2, 109] However, they often suffer from the disadvantage of template

removal and structural shrinking. Moreover, poor mass transfer, low binding constants and slow binding kinetics can cause an inefficient chiral recognition in MIPs.[2, 101, 161, 169] Substituting polymeric materials with metals is an interesting alternative way to retain chiral information inside matrices even after the template removal. However, it still suffers from the drawback that recognition efficiency is limited by the active area of flat metal surfaces.[63] To overcome the problem of very low active surface areas, mesoporous metals should be used.

Due to the low surface area of flat surfaces, mesoporous materials have been extensively applied in different fields such as catalysis, drug delivery and chemical detection related to their extremely high surface area.[175-177] Following a similar concept as the one described for the case of MIPs, mesoporous platinum films were deposited together with chiral template molecules and mesoporegens in order to control the structure of chiral cavities and mesoporous matrix, respectively.[2] As already explained in detail in the previous chapters, chiral encoded mesoporous platinum films can retain chiral information even after template removal. Moreover, the mesoporous structure not only increases the number of chiral active sites by up to two or even three orders of magnitude compared to flat surfaces, but also facilitates the accessibility of the chiral cavities for target molecules.

Electrochemical techniques are interesting tools for the detection of chiral compounds; however, such techniques require a physical connection between a power supply and the chiral imprinted mesoporous electrode as a working electrode. Hence, cost effective, wireless and portable electrochemical devices are highly desirable. Recently, wireless sensing devices including electrochemical interfaces, wearable smart electronics, radio frequency identification tags and near field communication labeling, have been developed. For example, Sampianato et al. described the development of a wireless wearable ring device for chemical sensing by using a battery powered stamp size potentiostat.[178] Furthermore, Mishra et al. demonstrated the concept of lab-on-a-glove, for which data transmission takes place via a smartphone.[179] Ma et al. recently reported wireless and portable sensing to detect food spoilage

using a conducting polymer, *i.e.* polyaniline, based on the principal of near field communication labeling.[180] Zhu et al. reported a wireless oxygen sensor based on the concept of radio frequency identification tags using Fe (II)-polymer wrapped carbon nanotubes.[181]

To design new materials for molecular sensing devices, conducting polymers are well-known materials able to show electrochromism and actuation, due to the change in oxidation state during the electrochemical reaction, and thus they can be used as an ingredient for wireless sensing/recognition, based on a physical transformation as an optical readout. Among all conducting polymers, polypyrrole doped with dodecylbenzenesulfonate (DBS) exhibits the highest efficiency of actuation, because of high volume changes during electrochemical cycling combined with a high mechanical strength.

Bipolar electrochemistry is an increasingly popular electrochemical concept, based on the polarization of a conducting object in an applied electric field. This approach has been used for various applications, for instance generating motion[182-184], site specific deposition[185, 186] and patterning[187, 188]. The generated potential difference between the two extremities of the conductive object can trigger an asymmetric reaction. The principal of bipolar electrochemical sensing is based on the wireless actuation of polypyrrole without any physical connection to the power supply.[7] In order to trigger motion of the polymer film, the material needs to be designed in an asymmetric way.[170, 189, 190] Our group has pioneered the electrochemical deformation for the purpose of wireless sensing of chemical and biochemical molecules in solution by using a free standing conducting polymer film.[189] The polypyrrole films were electropolymerized in the presence of high molecular weight electrolytes such as DBS, which act as a surfactant to provide better physical properties, leading to the formation of long and well-organized polymer chains. The obtained surface morphology is very different on the two faces of the polymer. One side is quite rough due to the free growth into the solution, whereas the other side is rather smooth because it was facing the electrode support during the electrodeposition. In a bipolar electrochemical system, an electric field is generated in the electrolyte solution, and triggers an oxidation

and reduction reaction occurring simultaneously at the two extremities of the polymer strip. [7] This leads to a differential swelling and shrinking along the main axis of the film. During the experiment, the symmetry of the polypyrrole strip is broken due to the asymmetric polarization triggered by the applied electric field, and therefore, the bipolar approach gives an easy and straightforward access to wireless actuation of the polymer. Furthermore, the electrochemical reaction at one extremity can be tuned in such a way that the actuation allows an optical readout of the concentration of chemical and biochemical compounds present in the solution.[189] A freestanding film of PPy was used to illustrate the possibility of measuring several chemicals including hydrogen peroxide, hydroquinone and glucose with a bipolar electrochemical set-up.

Based on the aforementioned promising results of wireless electroanalysis, we were interested in combining chiral mesoporous metals together with a freestanding polypyrrole film in order to test the possibility to recognize specifically chiral molecules via the wireless electromechanical deformation of the polymer. The objective of this work is to integrate the outstanding characteristic properties of both constituents, leading to a synergy of enantioselectivity and actuation. This approach not only generates an advanced hybrid material, but also increases the functionality of the conducting polymer and the range of possible applications of mesoporous chiral imprinted metals. We therefore propose to combine the above-mentioned chiral platinum as an enantioselective component together with the conducting polymer, in order to design a wireless enantioselective PPy actuator. The resulting hybrid material with dual functionality allows triggering the actuation in the presence of a chosen enantiomer. This can be considered as the artificial biomimetic equivalent of a muscle, which is preferentially interacting with only one stereoisomer, analog to what has been observed in body tissue.[191]

3.2 Experimental section

Chemicals

Hexachloroplatinic acid hydrate ($\text{H}_2\text{PtCl}_6 \cdot x\text{H}_2\text{O}$), polyoxyethylene (10) cetyl ether (Brij C10), *R*-, *S*- mandelic acid, pyrrole, potassium iodide, iodine, hydrogen peroxide, and sulfuric acid were purchased from Sigma-Aldrich. Hydrochloric acid was purchased from Alfa Aesar. All solutions and lyotropic liquid crystalline gel were prepared by using MilliQ water (resistivity: 18.2 M Ω cm). All chemicals were directly used without any purification.

Gold-coated glass substrate cleaning

A gold-coated glass slide was employed as a substrate for the electrodeposition of chiral encoded mesoporous platinum electrodes. In order to clean the gold surface of the substrate (1.6 cm \times 2.4 cm), the gold-coated glass was immersed in piranha solution (H_2SO_4 and H_2O_2) for 30 min, resulting in organic impurities removal ([Scheme 3.1a](#)). Subsequently, the substrates were rinsed with MilliQ water until the acid solution on the surface was totally removed, and then dried with nitrogen. The substrates were connected with a normal wire and the electrode's geometric surface area of about 1.6 cm \times 0.5 cm was defined with scotch tape during the electrodeposition of chiral imprinted mesoporous platinum.

Chiral encoded mesoporous platinum using mandelic acid as a template

Electrodeposition of the chiral encoded mesoporous platinum was carried out following a literature procedure. [2, 3, 39] Chiral imprinted mesoporous Pt electrodes were prepared by electroreduction of the platinum salt in the simultaneous presence of a self-assembled lyotropic liquid crystal and the chiral template. Polyoxyethylene (10) cetyl ether (Brij C10) as a non-ionic surfactant, and enantiomeric mandelic acid were used as a mesoporegen and chiral template, respectively. To prepare plating mixtures for platinum deposition, the liquid crystal composed of 42 wt% Brij C10, 29 wt% chloroplatinic acid, 29% wt% MilliQ water and the desired amount of mandelic acid template

were combined. The resulting gel was mixed to obtain a homogeneous paste. The viscous plating gel was carefully placed on the gold-coated glass, and then a platinum mesh was positioned at the top of the gel as a counter electrode. Ag/AgCl was used as a reference electrode in the electrochemical cell. A potential of -0.15 V vs Ag/AgCl was applied to the gold substrate for the reduction of the platinum ions with various electrodeposition charge densities in order to optimize the film thickness. After electrodeposition, all the prepared electrodes were rinsed with MilliQ water several times to remove the chiral template and lyotropic liquid crystal from the mesopores and chiral cavities (**Scheme 3.1b**).

Hybrid PPy-chiral platinum

The as-prepared chiral-encoded mesoporous platinum was modified with a polypyrrole layer following a literature procedure.[7, 189] A solution composed of pyrrole (140 μ l, 0.2M) and sodium dodecylbenzenesulfonate (0.875 g, 0.2 M) in 10 ml MilliQ water was prepared. The previously modified gold plate was immersed in the monomer solution for 15 min and electropolymerization was carried out in a galvanostatic mode at 3.6 mA for 5400 s. The resulting hybrid material was cleaned with water for a day to remove residual monomer (**Scheme 3.1c**), and then peeled off by immersing it in a KI/I₂ solution for 2 days in order to etch away the underlying gold layer. Afterwards the PPy-Pt film was rinsed with water to remove adsorbed I₂ and KI for 4 h (**Scheme 3.1d**).

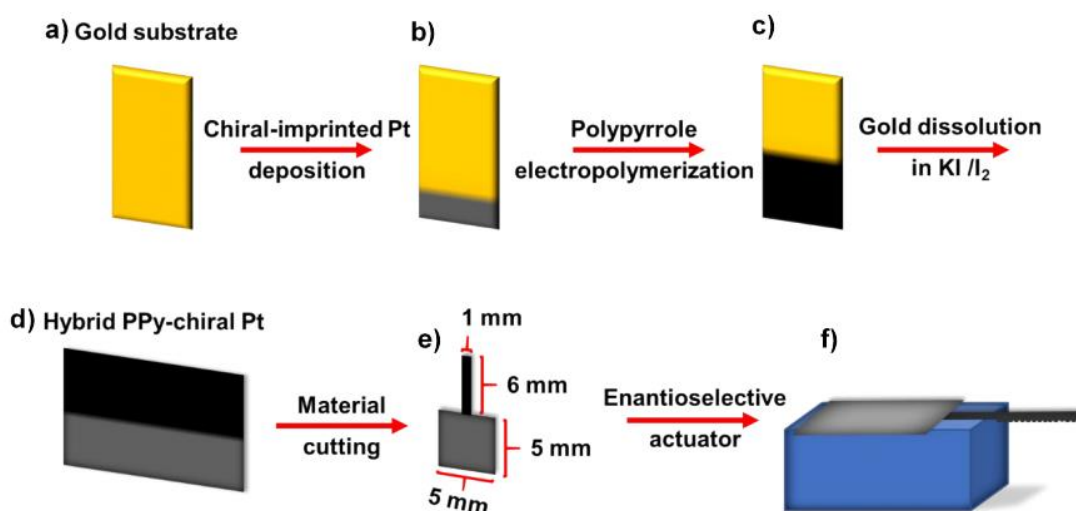
Electrode characterization

The surface morphology and the thickness of the hybrid material, PPy-chiral imprinted platinum, were characterized by SEM performed on a Hitachi TM-1000 tabletop electron microscope and JEOL, JSM-7610F. In addition, the electrochemical characterization of chiral encoded mesoporous platinum was performed using a μ Autolab type III equipped with a three-electrode system. The prepared electrodes, a platinum mesh and Ag/AgCl (Sat. KCl) were used as working electrode, counter electrode and reference electrode, respectively. Chiral recognition at the prepared electrode surfaces was confirmed by DPV

with a step potential and modulation amplitude of 25 mV in 50 mM mandelic acid and 50 mM HCl as a supporting electrolyte at a scan rate of 50 mVs⁻¹.

Enantioselective actuator

A piece of the hybrid PPy-Pt film with dimensions of 1 mm × 6 mm × 50 μm (PPy) and 5 mm × 5 mm × 50 μm (Pt-PPy) (**Scheme 3.1e**) was fixed on an inert support at the center of the electrochemical cell (**see Scheme 3.1f**). Two graphite electrodes with 10 mm diameter were used as feeder electrodes in the bipolar electrochemical system. The cell was filled with a solution of 50 mM mandelic acid in 50 mM HCl. A potential of 5.3 V was applied between the feeder electrodes for the chiral actuation experiment. After waiting for 5 min to ensure that the solution was able to diffuse inside the porous structure, a video was recorded with a macroscope (LEICA AZ16 APO).

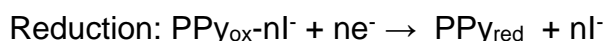
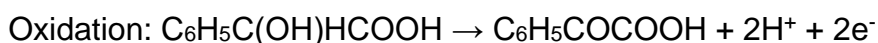


Scheme 3.1 Preparation of a hybrid chiral Pt-PPy film a) gold substrate; b) chiral-imprinted Pt partially covering the gold coated glass slide; c) hybrid film on gold substrate; d) freestanding hybrid film after etching of the gold layer; e) tailored final geometry of the actuator f) enantioselective actuator mounted on a rubber support.

3.3 Results and discussion

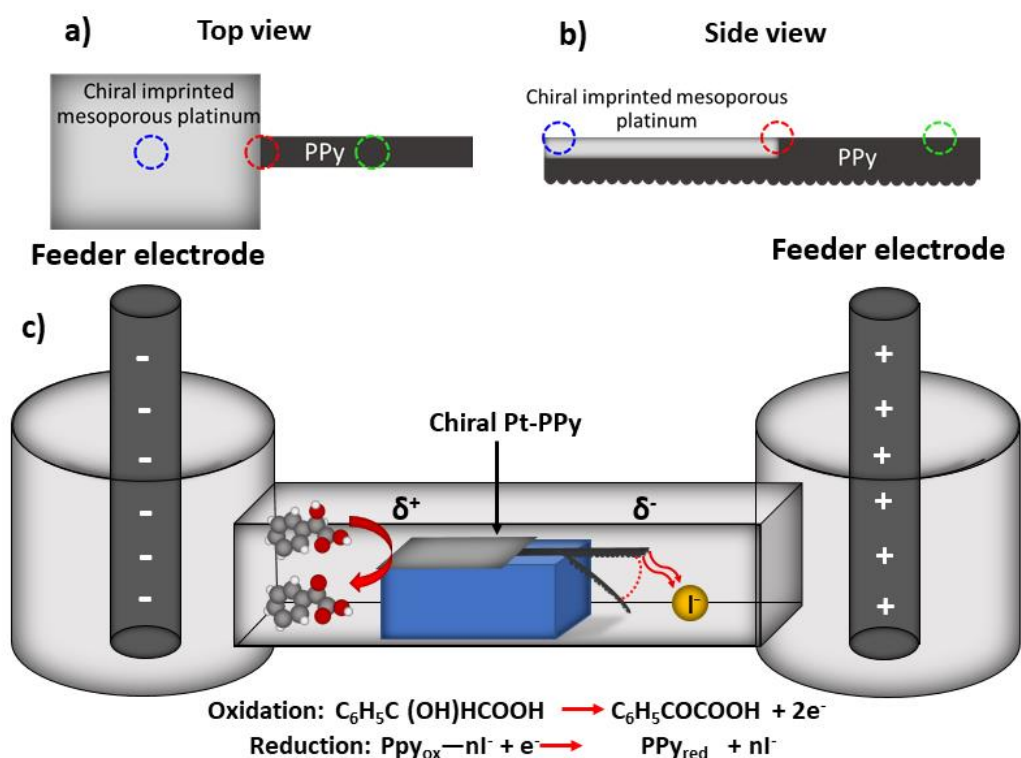
In order to test the use of the hybrid material as an enantioselective actuator, the PPy-chiral Pt film was attached to an inert support in the middle of

the bipolar cell as shown in [Scheme 3.2](#). When applying the potential, the oxidation of mandelic acid occurs at the positively polarized chiral imprinted Pt surface. On the other hand, the reduction of polypyrrole takes place at the negatively polarized side of the oxidized polypyrrole strip. The change in redox state during electroactuation is compensated by the release of iodide ions. The reduction of polypyrrole and the release of iodide is directly and quantitatively correlated with the oxidation of chiral mandelic acid at the imprinted platinum side. In the case of Pt-PPy imprinted with R-mandelic acid, the R enantiomer is preferentially oxidized at the encoded platinum. This can be attributed to a more favorable partition coefficient for this enantiomer between the solution and the porous metal phase. The redox processes occurring at the extremities of the hybrid PPy-Pt material in a mandelic acid solution are described by the following equations



The bending amplitude and kinetics of PPy at the negative polarized side quantitatively corresponds to the amount of mandelic acid which is oxidized at the chiral imprinted surface. For example, using imprinted platinum with R-MA as a chiral template leads to a more favorable electrooxidation of R-MA compared to S-MA because of its chiral feature is matching the chiral metal cavities, and therefore the degree of bending of PPy in R-MA solution is much higher than that of S-MA. On the other hand, the bending kinetics of hybrid Pt-PPy imprinted with S-MA is higher in S-MA solution than the one observed in R-MA solution. The discrimination can be represented in the terms of relative bending:

$$\text{Relative bending} = \frac{\text{Bending distance of the studied enantiomer at a given time}}{\text{Final bending distance for the imprinted enantiomer}} \quad (3.1)$$



Scheme 3.2 Illustration of the hybrid Pt-PPy film used for chiral recognition (a) Top view and (b) cross section of Pt-PPy (c) Scheme of the bipolar electrochemical cell for chiral recognition of mandelic acid with the hybrid actuator.

Chiral-encoded mesoporous platinum characterization

In order to observe the morphology and components of hybrid Pt-PPy, scanning electron microscopy (SEM) with energy dispersive X-ray spectroscopy has been used. The surface morphology of free-standing hybrid films is illustrated in [Figure 3.1](#). The images reveal a homogeneous deposition and smooth surface in the entire area of the Pt-PPy film. [Figure 3.1a](#) presents the surface morphology of chiral imprinted mesoporous platinum deposited with a charge density of 8 C cm^{-2} , illustrating a homogeneous deposition and smooth surface of platinum without any void space. A constant thickness of $\sim 1 \text{ }\mu\text{m}$ for the platinum layer is visible in [Figure 3.1d](#). The surface texture and cross section of the as-synthesized polypyrrole film was also investigated. The PPy

part of the hybrid material exhibits two different faces, similar to what has been described previously.[7] Very smooth PPy is observed for the top face (**Figure 3.1c**), because it has been facing the gold substrate during polymerization, whereas the bottom face is rougher due to the free growth of the polymer towards the electrolyte (**Figure 3.2**). Moreover, as described in previous work,[7] the conductivity of the smooth and rough faces is quite different due to different degrees of cross-linking. A cross sectional view of the polymer indicates a total thickness of about 50 μm (**Fig. 3.1f**). This asymmetric behavior between the two faces of the film in terms of density of cross-linking is absolutely important for actuation, because it constitutes the equivalent of a classic bilamellar structure. This allows using the as-synthesized polymer film as a chiral actuator without the need of fixing it onto another non-electroactive material. The homogeneous thin platinum layer is intimately connected to the PPy film (**Figures 3.1b** and **3.1e**). The elemental composition is confirmed by EDS mapping with platinum coded as green and carbon as red (inset of **Figure 3.1b**). The good electrical connection between the two materials ensures the efficient electron transport during the actuation process.

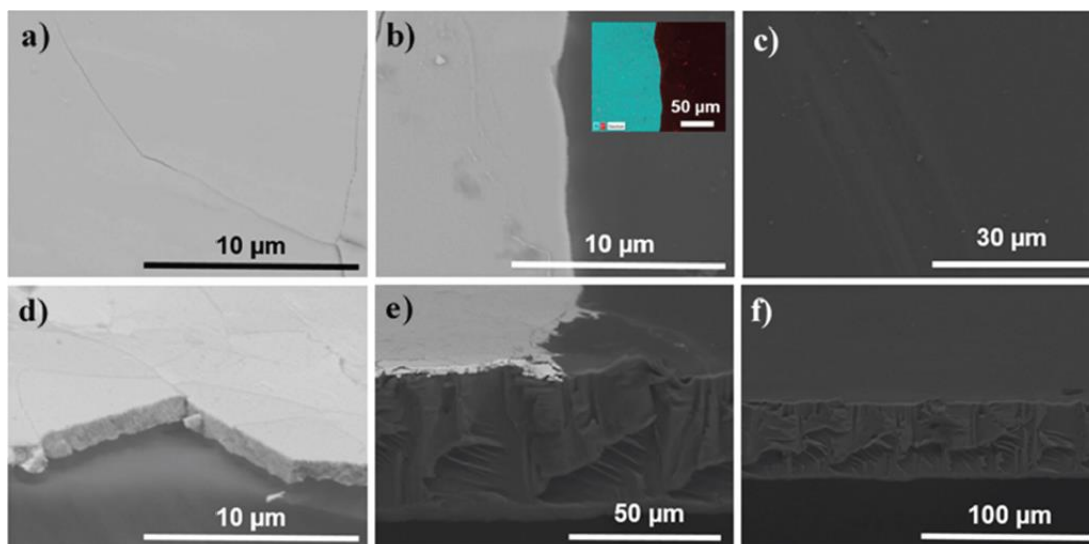


Figure 3.1 SEM images of the hybrid chiral imprinted Pt–PPy film at different positions. (a and d) top and side view of the chiral-encoded platinum layer, (b and e) top and side view of the Pt–PPy junction (inset: EDS map), (c and f) top and side view of the PPy film.

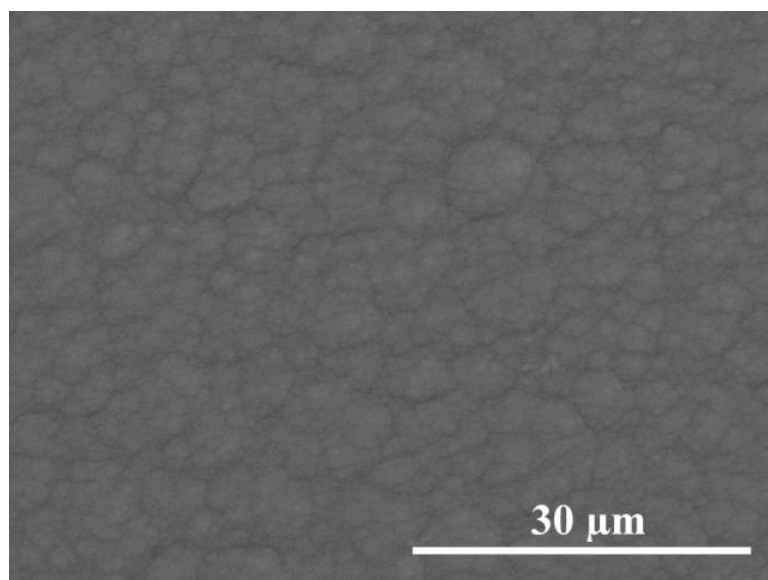


Figure 3.2. SEM image of the bottom face of the free-standing hybrid Pt-PPy material.

Chiral actuator

In order to confirm the recognition of chiral molecules at encoded platinum surfaces, the enantioselective properties of the hybrid Pt-PPy film was first tested by using DPV in solutions of the two mandelic acid enantiomers. The oxidation signal of mandelic acid was recorded in the potential range from 0.2 to 0.8 V vs Ag/AgCl ([Figure 3.3](#)). The signal amplitude of Pt-PPy imprinted with R-MA is significantly higher in a R-MA solution compared to the analogous experiment in S-MA. This indicates that the hybrid R-MA imprinted Pt-PPy preferentially converts R-MA at the platinum surface rather than S-MA. A very similar behavior has been observed in previous studies for the enantioselective electrochemistry of other chiral molecules. The discrimination of the two enantiomers can be ascribed to a change in partition coefficient between the chiral solution and the porous metal phase. One can compare the metal phase with a sponge that has a higher affinity for one enantiomer due to the presence

of the chiral cavities. Therefore, the apparent concentration of the “good” enantiomer in the metal phase is higher with respect to the “wrong” enantiomer. This leads to higher oxidation currents, and it is therefore expected that in the bipolar electrochemical set-up such higher currents should allow a similar discrimination via an electromechanical read-out.

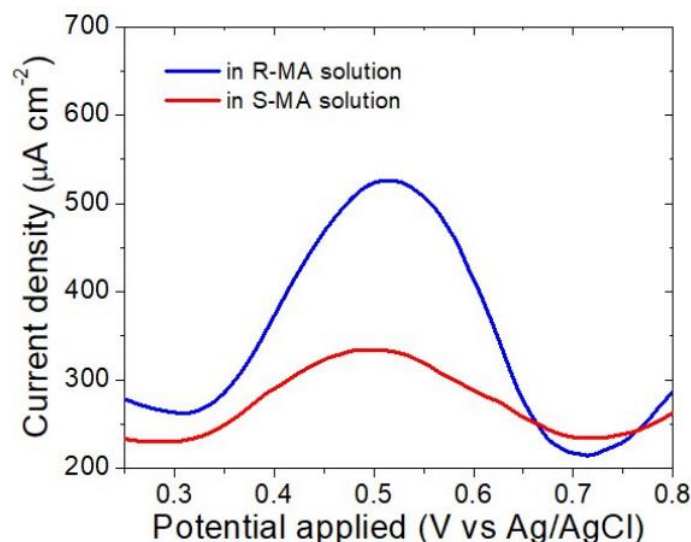


Figure 3.3. Differential pulse voltammetry of R-MA imprinted Pt-PPy in 50 mM R-MA (blue) and S-MA (red) using 50 mM HCl as supporting electrolyte.

For the chiral actuator experiment, the free-standing hybrid Pt-PPy was placed at the middle of the bipolar cell with the rough surface of PPy orientated downwards. While applying the electric field, the chiral encoded Pt side is facing the negative feeder electrode and therefore will be positively polarized (δ^+). As mentioned above, oxidation of mandelic acid, provides two electrons during the oxidation process. On the other hand, the PPy side is facing the positive feeder electrode, leading to a negative polarization potential at this extremity of the bipolar object. The electrons liberated by the oxidation at the Pt side are consumed by the reduction of PPy side, accompanied by a release of I^- ions. The release of iodide preferentially occurs through the rough face of the polymer due to the higher active surface area. Consequently, this face of the polymer strip starts to shrink and induces a bending towards the rough face. The degree of bending should be therefore directly correlated with the number of electrons

available from the oxidation of mandelic acid occurring at the opposite end of the strip.

The potential difference between the two feeder electrodes was optimized in order to identify the most suitable conditions for the chiral actuator in a mandelic acid solution. At potentials below 5.0 V, deformation of PPy could not be observed because it is not enough for the oxidation of mandelic acid at chiral imprinted platinum surface and the simultaneous reduction of the polymer, whereas for potentials above 5.5 V, fast bending of PPy could be observed. However, for too fast redox reactions, selectivity is less pronounced. Therefore, the most suitable potential is in the range between 5.2 and 5.4 V. The distance of the actuator extremity between the position before and during the actuation process has been measured in order to calculate the relative bending described in [equation 3.1](#) for R-MA and S-MA solutions.

In order to confirm the selective deformation of the hybrid material a control experiment using non-imprinted Pt-PPy has been also performed. It was found that there is no significant difference in the bending kinetics of PPy between R-MA and S-MA solutions as shown in [Figure 3.4](#).

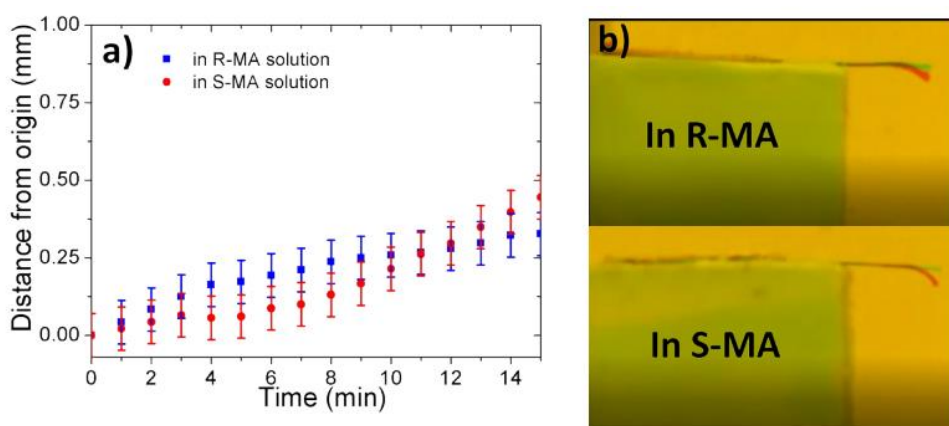


Figure 3.4 (a) Bending as a function of time for non-imprinted Pt-PPy in 50 mM R-MA (blue) and S-MA (red) using 50 mM HCl as supporting electrolyte. (b) Images of non-imprinted hybrid PPy-Pt during chiral analysis in R-MA (top) and S-MA (bottom) at the beginning (green) and after 15 min (red).

The bending kinetics of the enantioselective actuator imprinted with the two different conformations of mandelic acid was measured using 50 mM HCl as a supporting electrolyte (Figure 3.5). In the case of R-MA imprinted Pt-PPy, the polymer strip exhibits a significant and rapid bending in R-MA solution, due to more efficient electrooxidation of this enantiomer. However, in a solution containing S-MA, the target molecules are converted more slowly, eventually leading to a less pronounced bending (Figure 3.5a). In contrast, the symmetrically opposite situation is also studied by using S-MA imprinted Pt-PPy. As expected, the bending is now more efficient in S-MA solution compared to the R-MA solution (Figure 3.5b). The differentiation between the two enantiomers is based on the kinetics of bending, because it is directly related to the amplitude of the local current flowing in the bipolar object. The analytical information is provided by the speed of bending of these materials conditioned by the selective recognition via the chiral imprinted mesoporous platinum. The above results indicate that the bending rate is significantly different for the two enantiomers, and thus allows achieving a pronounced enantioselectivity of these hybrid materials. Therefore, at a given time, the degree of bending is higher for the “good” enantiomer compared to the “wrong” one. Obviously, when waiting for a long enough time, this difference will become smaller, because the polymer in the “good” enantiomer solution reaches its maximum degree of bending imposed by the experimental set-up, and therefore the polymer in the “wrong” solution will be able to catch up.

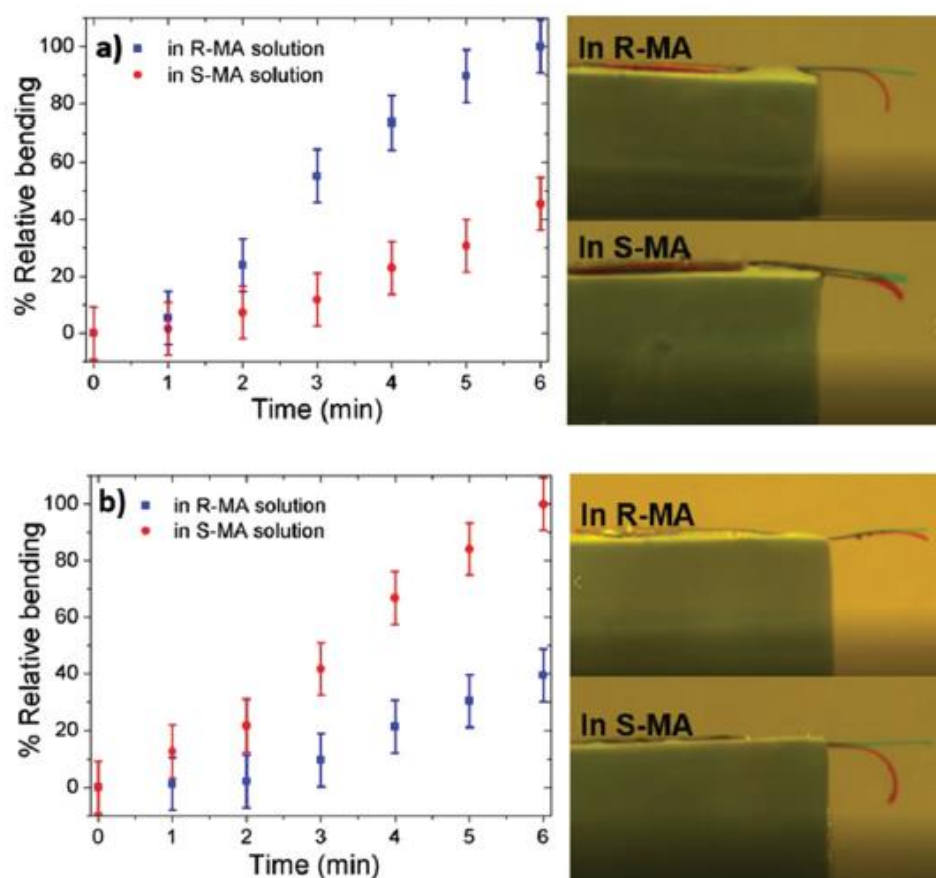


Figure 3.5 Bipolar electrochemical actuation of hybrid chiral Pt-PPy in 50 mM R-MA (blue) and S-MA (red) using 50 mM HCl as supporting electrolyte. Relative bending measured as a function of time for (a) R-MA imprinted Pt-PPy and (b) S-MA imprinted Pt-PPy. The pictures on the right have been taken after 6 min of applied potential. The green line indicates the initial position of the actuator, whereas red corresponds to its final position.

3.4 Conclusion

In summary, a free-standing hybrid bilayer material, chiral imprinted Pt-PPy, has been successfully obtained by combining electrodeposition of chiral encoded platinum and electropolymerization of PPy. The synergistic properties of both materials, wireless actuation and chiral recognition, were used for wireless chiral analysis. The surface morphology of the hybrid material was smooth for both materials, Pt and PPy, and the junction between both sides

clearly shows the intimate interaction between them. The concept of bipolar electrochemistry allows oxidizing selectively the right enantiomer at the chiral imprinted metal surface, whereas the polymer undergoes a corresponding reduction process accompanied by a release of iodine anions. This leads to a controlled deformation of the polymer film, acting as a readout signal of the chiral information. This versatile approach opens interesting perspectives not only for purely analytical applications, because such a hybrid material can also be considered as the biomimetic equivalent of a muscle, which is activated only by one stereoisomer, thus representing the artificial version of enantioselective actuation schemes in the body. This study opens access to a simple concept combining bipolar electrochemistry and enantiomeric analysis, thus allowing envisioning the design of a miniaturized device for chiral analysis based on a straightforward wireless electromechanical readout.

Chapter 4

Hierarchical macro- and mesoporous nickel nanosheets for oxygen evolution reaction

4.1 Introduction

Nowadays, energy demands have been increasing rapidly owing to population growth and progressing technology. Normally, fossil fuel is widely used to produce energy, whereas its amount is depleting and the release of CO₂ causes the greenhouse effect. Finding alternative energies that are able to play a significant role in energy applications, and simultaneously are environmentally friendly and increase sustainability is one of the most important challenges for energy development.[192-195] For instance, the conversion of water into hydrogen and oxygen, also called water splitting, is one of the most fascinating strategies, due to the capability of being used for producing clean power and having the advantage of being storable.[196-201] Regarding the hydrogen evolution reaction (HER) at the cathodic surface during water splitting, reduction of water generally needs low overpotentials of around 100 mV,[202] whereas for the anodic part, the oxygen evolution reaction (OER), requires significantly higher overpotentials compared to HER, in the range of 300 to 500 mV on commercial platinum-based electrocatalysts, due to sluggish electron transfer kinetics at the electrode interfaces.[203-205] Apart from Pt-based catalysts, Ir- and Ru-based catalysts are preferentially considered as one of the most efficient electrocatalysts for OER in acid media due to their high electrocatalytic activity at low overpotentials.[206] For instance, IrO₂ and RuO₂ nanoparticles were synthesized by a two-step preparation including metal nanoparticles and oxidation at high temperature. Both IrO₂ and RuO₂ nanoparticles were highly active for electrocatalytic OER and are currently benchmark catalysts for water splitting. In addition, nanoscale catalysts have been designed in order to reduce the noble metal content, due to a significantly higher active surface area. The common strategy is using conductive carbon as a support material for

nanoparticles. Reier and co-workers studied the intrinsic electrocatalytic activity of carbon supported Pt, Ru and Ir nanoparticles. Compared to bulk metals all catalysts exhibited a significantly improved electrocatalytic OER activity.[207] Nevertheless, the disadvantages of metal dissolution and high operating costs result in difficulties for practical industrial applications.[208-210] Therefore, great effort has been made in the development of alternative catalysts based on earth-abundant and non-precious metals, such as nickel-based electrocatalysts, like nickel foams,[211, 212] nickel alloys,[213, 214] nickel nitride,[215] nickel phosphides,[216-218] nickel selenide,[219, 220] nickel oxide[221, 222], layered nickel double hydroxide[223] and nickel hydroxide.[221, 222]

As stated above, although there are many publications focusing on the improvement of nickel-based catalysts for water splitting, they often suffer from a small surface area and poor mass transport of oxygen molecules.[224] To circumvent these problems, 3D multiporous materials or hierarchical porous materials, composed of micropores, mesopores and macropores have been developed over the past decades, aiming to illustrate the synergistic effect of hierarchical porous structures.[43, 225, 226] Typically, templating approaches have been employed to generate the porous structure, and these porous materials have played an important role as electrocatalysts for OER, because of their unique properties such as a very high electroactive surface area, the possibility of fine-tuning the morphology and improved mass transport. In general, hard template and soft template approaches have been widely used for tuning the porous structures and catalytic properties of hierarchically organized porous metals and metal oxides. For instance, macro- and mesoporous platinum prepared by the one-step electrodeposition of platinum salts in the simultaneous presence of silica nanoparticles and sodium dodecyl sulfate (SDS) greatly enhanced the electrocatalytic performance in methanol oxidation owing to its higher electroactive surface area.[42]

In order to create macroporous structures, there are two general techniques employed for assembling the template, namely Langmuir-Blodgett (LB) deposition and slow evaporation of particle suspensions. Rather

uncontrollable porous structures are obtained by the slow evaporation technique, and therefore very often LB has been preferred. LB deposition is one of the most useful approaches,[227-229] which is frequently employed for coating monolayers or multilayers of template films such as polymer and silica beads, by controlling the surface pressure between air and the water interface.[56] The LB technique, which provides exactly controllable layer-by-layer coatings with uniform film thickness and highly ordered structure, has been used to design materials for various applications ranging from analysis,[57, 230] and sensing,[231] to separation [232] and electrocatalysis.[233] However, the introduction of a single type of porosity generally provides a rather low surface area, leading to low catalytic performance. In order to enhance the active surface area of a single porous structure, many strategies have been followed. One of the most promising approaches is the reduction of the pore size to micropores. However, when the pore size is too small, mass transport limitations inside microporous connections are often observed, leading to low electrocatalytic activity. Therefore, a moderate pore size has to be used.

To design a mesoporous metal, there have been several reports about using the self-assembly of surfactants as mesoporous templates in which micelle structures can be observed when it reaches the critical micelle concentration (CMC).[1, 233] Over the past few decades, tuning the configuration of lyotropic liquid crystals (LLC) by applying a potential has been investigated for metal deposition, allowing an improvement of the viscosity of the solution in which the mesoporous phase can be formed even at concentrations below the CMC.[234, 235] The surfactant self-assembly is rearranged on the electrode surface by applying a suitable potential, revealed by analyzing the differential capacity in the mixture solution.[236, 237] The surface area of the obtained mesoporous architectures is greatly amplified when compared with a typical bare electrode. Furthermore, it is well-known that the additional surface area of mesoporous materials also depends on the pore structure.[231, 233, 236, 237] Although a significantly improved surface area can be achieved with mesoporous materials, they often suffer from the

disadvantages of a very small pore size, eventually resulting in diffusion limitations for bulky molecules penetrating the mesoporous network.

Generally, mesopores (2-50 nm in diameter) and micropores (<2 nm in diameter) provide a large pore volume and high surface area in materials. Diffusion is the main factor of mass transport limitations in micro- and mesoporous materials. The transportation of compounds with similar size to meso- or micropores is hindered. Therefore, these small pores can be combined with macropores (>50 nm in diameter) which improve mass transport.[238, 239] In addition, the connectivity between an additional porous system and the small pores needs to be designed in order to maximize the performance.[23] In this context, the hard templating approach for the production of hierarchical porous materials offers a precise control of the final porous structure.

In order to demonstrate the advantages of the synergistic effect of macro- and mesoporous architectures, we study here the performance of multiporous Ni electrodes, combining macroporous and mesoporous structures, for electrocatalytic OER. Hierarchical porous nickel nanosheets (Hi-Ni), integrating macro- and mesoporous structures are generated on a gold substrate by a two-step electrodeposition from nickel salts: (i) the first step is the electrodeposition of macroporous nickel from a Ni plating bath by using a colloidal crystal template, followed by silica bead removal to generate the macroporous nickel (Macro-Ni) with well-defined structural features; (ii) the Macro-Ni is then employed as a new substrate for nickel electrodeposition to generate a mesoporous nanosheet film in a Ni plating bath containing 5 wt.% of polyoxyethylene (10) cetyl ether (Brij C10) as a nonionic surfactant. The multiporous nanosheet architectures, obtained from this combined hard and soft templating approach, allow increasing the electroactive surface area and improving the accessibility of reactant for the electrocatalytic OER in water splitting application.

4.2 Experimental section

Chemicals

Nickel acetate tetrahydrate ($\text{Ni}(\text{OAc})_2 \cdot 2\text{H}_2\text{O}$), nickel chloride (NiCl_2), Boric acid, potassium hydroxide, hydrofluoric acid and polyoxyethylene (10) cetyl ether (Brij C10) were purchased from Sigma-Aldrich. All chemicals were used directly without any further purification and all solutions and the plating mixture were prepared using MilliQ water.

Mesoporous nickel nanosheets (Meso-Ni) deposition

A mixture containing 0.7 M nickel acetate tetrahydrate ($\text{Ni}(\text{OAc})_2 \cdot 2\text{H}_2\text{O}$), 1.0 M nickel chloride (NiCl_2), 3.0 M boric acid ($\text{B}(\text{OH})_3$) and 5 wt.% polyoxyethylene (10) cetyl ether (Brij C10) was dissolved in MilliQ water at 333 K. Mesoporous nickel was electrodeposited by chronoamperometry at -0.75 V vs Ag/AgCl at a controlled temperature of 313 K in order to adjust the viscosity of the mixture. Subsequently, the modified electrode was cleaned with isopropanol and rinsed several times with MilliQ water to remove the surfactant from the pores.

Macroporous nickel (Macro-Ni) preparation

Silica particles of 920 nm diameter were synthesized following modified literature procedures,[41, 45, 56] and then used as colloidal crystal templates transferred onto a gold-coated glass slide by using the Langmuir-Blodgett technique (LB).[41-43, 45, 56] Prior to silica template deposition, the gold substrate was cleaned with isopropanol and plasma, respectively. The plating bath contains 0.7 M nickel acetate tetrahydrate (Sigma-Aldrich, 98%), 1.0 M nickel chloride (Sigma-Aldrich, 98%), 3.0 M boric acid (Sigma-Aldrich, >99%) in MilliQ water (18 M Ω). Macro-Ni was electrodeposited at -0.8 V vs Ag/AgCl at room temperature, and the number of deposited layers was monitored by chronoamperometry. The macroporous structure was visualized by scanning electron microscopy after removable of the template in 10% hydrofluoric acid, which is diluted from a commercial solution (Sigma-Aldrich, 48%) for 15 min. In order to prevent the degradation of nickel by hydrofluoric acid, the as-prepared

electrodes were rinsed with MilliQ water for 30 min to remove the acid solution from the pores.

Hierarchical macro- and mesoporous nickel nanosheets (Hi-Ni) deposition

Hi-Ni was prepared by electrodeposition of mesoporous nickel using the above-mentioned approach, but with a Macro-Ni electrode as a substrate. Typically, the electrode was immersed in the nickel bath for 15 min and then electrodeposition was carried out by chronoamperometry at -0.75 V vs Ag/AgCl and 313 K. After electrodeposition, the prepared electrode was rinsed several times to remove the surfactant from the hierarchical pore structure.

Electrochemical Characterization

All electrochemical measurements were performed with a μ AUTOLAB type III and using a general electrochemical cell with a three-electrode compartment. Various electrodes of Meso-Ni, Macro-Ni, and Hi-Ni were used as working electrode, a platinum mesh and Ag/AgCl (sat. KCl) were used as a counter and reference electrode, respectively. The electroactive surface area of flat and porous Ni electrodes was obtained by cyclic voltammetry (CV) in the potential range of the capacitive region between 1.04 and 1.14 V vs RHE in 1 M N₂-saturated KOH at various scan rates. In order to observe the beneficial effect of the prepared electrodes for oxygen evolution reaction (OER), the electrocatalytic activity was measured by linear sweep voltammetry (LSV) in 1M KOH with nitrogen bubbling in the range between 1.2 V and 1.8 V at a scan rate of 5 mV.s⁻¹ and the applied potentials were normalized with respect to the reference hydrogen electrode (RHE) ($V_{\text{RHE}} = V_{\text{Ag/AgCl}} + 0.197 \text{ V} + 0.059 \text{ pH}$). The stability of the electrodes was investigated at two different potentials: (i) 1.52 (slow OER rate) V; (ii) 1.72 V (fast rate) during 2 h of reaction time.

Surfactant assembly study.

Chronoamperometry was used to investigate the effect of self-assembly of surfactant on the electrode surface during electrodeposition. Several gold-coated glass slides were exposed to a solution of 5% wt Brij 56 in 3.0 M boric acid while applying different potentials ranging from -0.75 V to 0.1 V for 1 min. The surfactant modified electrodes were then rinsed with miliQ water and directly transferred to a 0.5M NaCl solution in order to measure the current decay at an applied potential of -0.1 V vs Ag/AgCl for 1 min.

Compositions characterization and surface morphology

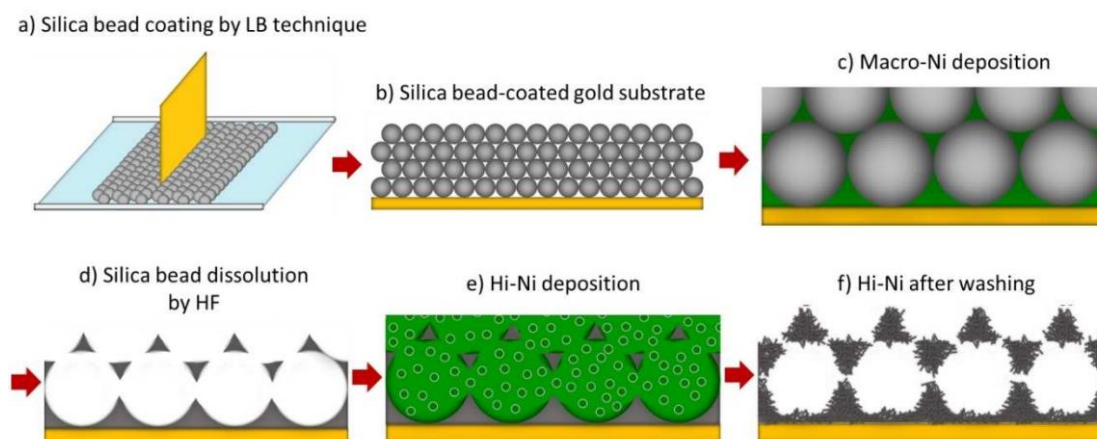
The composition of the prepared electrode surfaces was investigated using a Bruker D8 ADVANCE instrument with $\text{CuK}\alpha$ radiation (40 kV, 40 mA) in the 2θ range from 5° to 60° with a step size of 0.02 and a scan rate of 1 min^{-1} . In order to investigate the surface morphologies and monitor the number of deposited layers on the prepared electrodes, scanning electron microscopy (SEM) was performed on a Hitachi TM-1000 tabletop microscope and a JEOL JSM-7610F. In addition, macroporous structures and nanosheet features were directly observed by high-resolution SEM. To show the thickness of the films, SEM was performed with the cross-section after cutting the electrodes. The composition of the prepared nickel electrodes was analyzed by Energy dispersive X-ray spectroscopy (EDS) which was carried out with a JEOL, JEM ARM 200F model with an accelerating voltage of 200 kV.

4.3 Results and discussion

Electrode fabrication

In order to elaborate the hierarchical multiporous nickel nanosheet electrodes for electrocatalytic OER, we followed the preparation scheme shown in [Scheme 4.1](#). In the first step, a well-defined colloidal template has been successfully obtained by a layer-by-layer deposition process carried out with the LB technique as shown in [Scheme 4.1a](#) and [4.1b](#). A highly ordered structure of silica beads was obtained due to the pressure-controlled arrangement of the beads at the water-air interface ([Figure 4.1](#)). Subsequently nickel metal was

electrodeposited from a nickel-plating solution (**Scheme 4.1c** and **4.1c**). The number of deposited nickel layers was monitored by the oscillations of the current during the chronoamperometric deposition as shown in **Figure 4.2**. The current density minima correspond to odd-half layers of macroporous nickel, and allow stopping the electrodeposition in such a way that an open porous structure is obtained. The Macro-Ni showed a highly-ordered honeycomb-like porous structure after the dissolution of the silica bead template. In the last step, Macro-Ni was employed as a working electrode for the electrodeposition of hierarchical multiporous nickel nanosheet electrodes in the nickel-plating solution containing non-ionic surfactant as shown in **Scheme 4.1e** and **4.1f**.



Scheme 4.1. Schematic illustration of the synthesis of hierarchical macro- and mesoporous nickel deposited on a gold-coated glass slide using a colloidal crystal template: a) transfer of individual layers of silica beads onto the substrate by the LB technique; b) final silica bead template; c) electrodeposition of nickel; d) silica bead dissolution leads to Macro-Ni; e) electrodeposition of a mesoporous nickel film on the internal surface of Macro-Ni using a surfactant assembly as a template; f) Hi-Ni after the washing step.

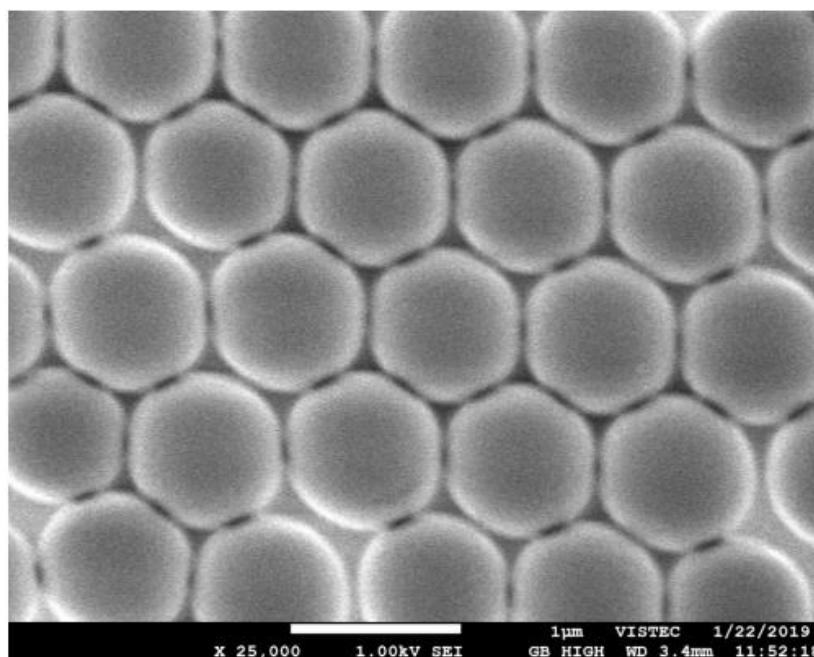


Figure 4.1 SEM image of a substrate coated with silica beads by using the Langmuir-Blodgett technique.

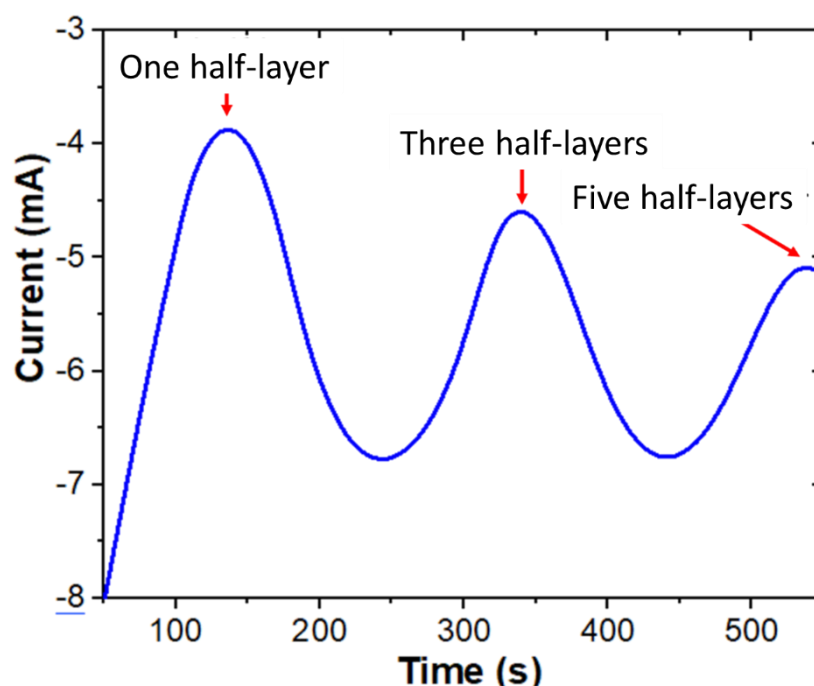


Figure 4.2 Chronoamperometric curve recorded during potentiostatic nickel electrodeposition through the first five half-layers of the colloidal silica-bead template (particle size of 920 nm diameter).

Porous electrode characterization

Scanning electron microscopy (SEM) was used to observe the surface morphology on the prepared porous electrode surfaces. A well-ordered arrangement of macropores is illustrated in **Figures 4.3a-c**. The void spots in the obtained macropores correspond to the connecting windows between consecutive macropore layers.[42, 57] The thickness of the Macro-Ni electrode is around 1.3 μm , corresponding to three half-layers of pores, with a constant thickness over the entire area. Mesoporous nickel nanosheets are then formed during electrodeposition with a nickel bath in the presence of a lyotropic liquid crystalline phase as a mesoporegen. The mesoporous features obtained by the electroreduction with a deposited charge density of 5 C cm^{-2} are illustrated in **Figures 4.3d** and **3e**. The mesoporous nanosheet texture is generated in the presence of non-ionic surfactant during electrodeposition even in the presence of only a small amount of surfactant (5 wt.%). This is due to the applied potential which can induce the self-assembly of micelles on the electrode substrate.[235] The phase diagram of self-assembled nonionic surfactant depends on the applied potential.[240] In other words, the tuning of the potential allows us to precisely control the structure of the non-ionic self-assembly.[237] At strongly negative potentials, a large fraction of surfactant is present at the electrode interface and leads to a reorganization of the spherical micelle phase into a lamellar micellar phase, responsible for the formation of the mesoporous nanosheet features. A homogeneous thickness of $\sim 1.1 \mu\text{m}$ (cross section view) is observed by SEM (**Figure 4.3f**). In order to study the formation mechanism of the lyotropic liquid crystalline structure at the electrode interface, various potentials of 0.1 V, 0 V, -0.1 V, -0.25 V and -0.75V were applied to the Brij solution, and subsequently, the electrode was investigated by chronoamperometry in 0.5 M NaCl at -0.1 V vs Ag/AgCl (**Figure 4.4**). Interestingly, electrodes modified at a highly negative potential show low currents due to the higher packing density of micelles. This allows a controlled transformation from a spherical micellar phase into a lyotropic lamellar liquid crystalline phase.[241] Therefore, the electrodeposition leads to nanosheet structures when applying highly negative potentials in the presence of Brij C10.

This allows increasing the electroactive surface area for electrocatalytic OER. [242]

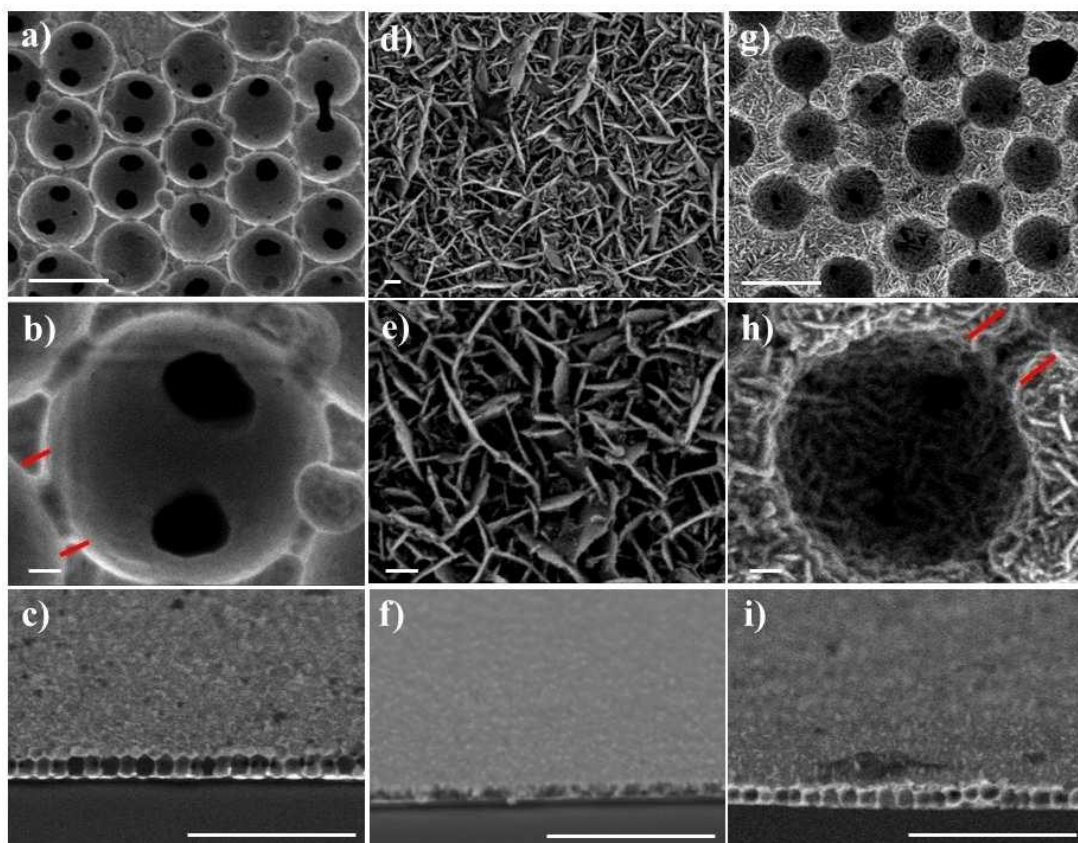


Figure 4.3 Scanning electron microscope (SEM) images of Macro-Ni obtained by the electroreduction of nickel salt in the void space of three half-layers of the colloidal silica template composed of beads with a diameter of about 920 nm (a: top view, scale bar 1 μm ; b: top view, scale bar 100 nm; c: cross section, scale bar 10 μm); Meso-Ni obtained by electrodepositing nickel with a charge density of 5 C cm^{-2} (d: low magnification, scale bar 100 nm; e: high magnification, scale bar 100 nm; f: cross section, scale bar 10 μm); Hi-Ni obtained by the electrodeposition of Meso-Ni inside the macropores (920 nm diameter) with a thickness of three half-layers (g: top view, scale bar 1 μm ; h: top view, scale bar 100 nm; i: cross section, scale bar 10 μm).

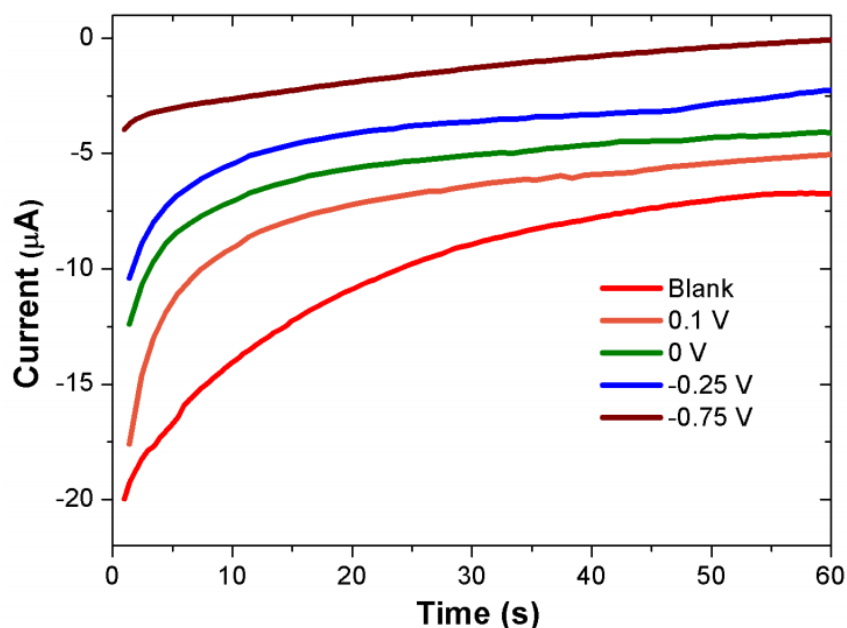


Figure 4.4 Chronoamperometric curve at a constant potential of -0.1V (vs Ag/AgCl) in pure 0.5 M NaCl supporting electrolyte to evaluate the surface coverage of self-assembled surfactant on the electrodes obtained by applying different deposition potentials: 0.1 V (orange), 0V (green), -0.25V (blue), -0.75 V(brown) and bare Au electrode (red).

For synthesizing hierarchical multiporous nickel electrodes, the Macro-Ni electrode was employed as a working electrode after colloidal silica template removal for the further electrodeposition in a nickel-plating solution containing the surfactant. The resulting metal structure, composed of macropores and mesoporous nanosheets is shown in [Figures 4.3g](#) and [4.3h](#). Mesoporous nickel with nanosheet features is deposited on the macroporous structure, maintaining still the connecting windows (red line) between the pores. The Hi-Ni film thickness is $\sim 1.4 \mu\text{m}$ and is insignificantly changed compared with that of Macro-Ni because only a few layers of Ni nanosheets were deposited ([Figure 4.3i](#).) Furthermore, in order to investigate the purity of the electrode surface, which might affect the electroactivity for OER, the composition has been investigated by energy dispersive X-ray spectroscopy (EDS) as illustrated in [Figure 4.5](#). As

expected, the red spots refer to nickel composition and indicate the absence of metal impurities (Fe) in the deposit.

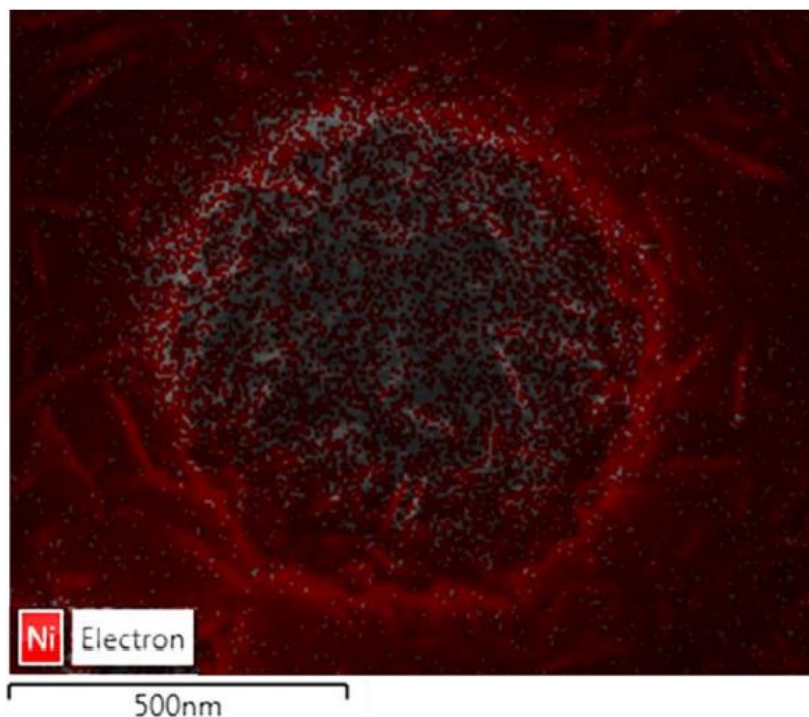


Figure 4.5 EDS mapping of Hi-Ni: Red spots indicate the nickel distribution on the prepared electrode in and around one macropore.

In addition, in order to analyze the crystallinity and composition of different nickel electrodes having the similar film thickness, thin film X-ray diffraction (XRD) has been used as shown in [Figure 4.6](#). The characteristic peaks of metallic nickel were confirmed at 2θ of 44.5, 52.0, 76.7 and 92.7 °(blue dots) and relate to Miller indices (hkl) corresponding to the crystal planes of (111), (200), (220) and (311), respectively.[243] Furthermore, oxygenated species (NiO, NiOOH and Ni(OH)₂) could be observed due to the oxidation of the prepared electrodes under air atmosphere..[27] In this case, three characteristic peaks of a face-centered cubic phase NiO (red spots) at 37.2, 43.2 and 62.8 corresponding to the (111), (200) and (220) diffraction planes, respectively, are identified.[244] In addition, NiOOH and Ni(OH)₂ species were also obtained as indicated by the green and yellow spots. The amorphous phase of the gold-coated glass substrate ($2\theta = 20^\circ$) is also visible because all

electrodes were prepared by using gold-coated glass. XRD results are complemented with EDS mapping, indicating that the electrodeposition of porous nickel could be achieved without any other metal impurity on the surface.

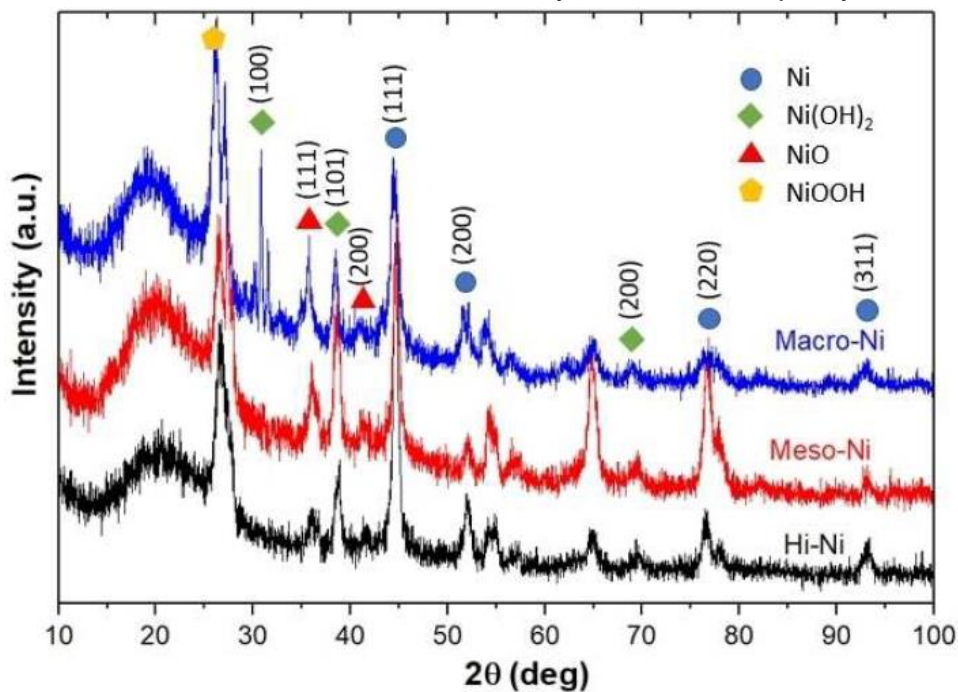


Figure 4.6. Thin film X-ray diffraction patterns of Macro-Ni (blue), Meso-Ni (red) and Hi-Ni (black) having a comparable film thickness of 1.2, 1.3 and 1.4 μm , respectively.

In order to measure the electrocatalytic surface area of bare and prepared nickel electrodes, CVs in 1 M KOH were recorded in the range of the capacitive double layer region with various optimized scan rates (5, 10, 20, 50 and 100 mV s^{-1}) as illustrated in [Figure 4.7a](#). To calculate the specific double layer capacitances of electrodes, the current density in the capacitive region is plotted as a function of the scan rate ([Figure 4.7b](#)). In order to measure the relative active surface area of the prepared nickel electrodes, a roughness factor (R_f) is calculated by dividing their capacitance by the capacitance of the bare nickel electrode obtained from I-V curves ($63.3\mu\text{Fcm}^{-2}$). The results are presented in [Table 4.1](#). As expected, hierarchical multiporous nickel nanosheets (Hi-Ni) display the highest surface area, followed by mesoporous

nickel (Meso-Ni), macroporous nickel (Macro-Ni) and flat nickel, which have the same thickness of $\sim 1.3 \mu\text{m}$, respectively. This indicates that the presence of the porous structures can greatly enhance the electroactive surface area.

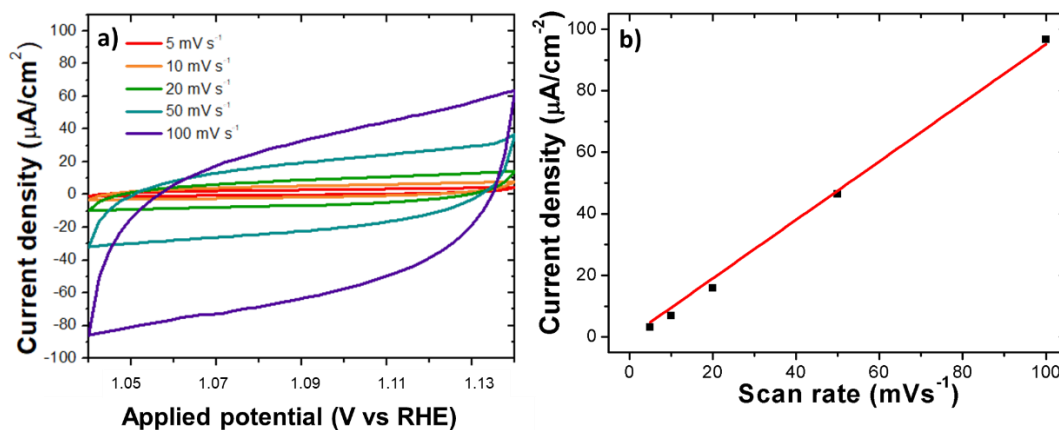


Figure 4.7 (a) Cyclic voltammograms of a three half-layer hierarchical nickel electrode (Hi-Ni) measured in N_2 -saturated 1 M KOH with varying scan rates in the range of 0 to 100 mV s^{-1} . (b) Plot of capacitance current density as a function of scan rate in order to determine the electroactive surface.

Table 4.1. Experimental and theoretical roughness factors of various fresh and used nickel electrodes taken before and after performing OER at different applied potentials.

Electrocatalyst	Roughness factor			
	Fresh electrode		Used electrode	
	Obtained value ^a	Theoretical value ^b	After OER at 1.52V ^c	After OER at 1.72V ^c
Flat Ni	1	-	1.1	1.2
Meso-Ni	8.4	-	10.7	12.7
One half-layer Macro-Ni	1.9	1.8	2.4	3
Three half-layer Macro-Ni	4.6	5.4	6.8	8.3
One half-layer Hi-Ni	6.9	-	8.8	9.3
Three half-layer Hi-Ni	15.6	20.7	21	31.5
Five half-layer Hi-Ni	33	34.5	34.4	39.9

^a The relative increase in roughness factor was calculated from the capacitance of the measured electrode divided by the capacitance of flat Ni. (b) The theoretical enhancement factor (f) is given by $f = n\pi (4/3)^{1/2}$

Furthermore, in order to illustrate the relationship between the roughness factor (R_f) and the thickness of hierarchical multiporous nickel films, the roughness factor measured by CV and the thickness of the electrodes obtained via SEM images were plotted as shown in **Figure 4.8**. As expected, an increase in the number of electrodeposited layers causes an increase of the roughness factor. To compare the obtained roughness factors and the theoretical roughness factor values, the theoretical value of the relative surface increase between bare and porous nickel can be estimated based on the assumption of a close packed pore structure.[230] The calculated enhancement factor (f) was used to determine the roughness factor of n half-layer porous electrodes following **Equation 4.1**:

$$f = n\pi (4/3)^{1/2} \quad (4.1)$$

where n is the number of pore layers. As expected, the roughness factors measured from the double layer capacitive region of a one half-layer and a three half-layer Macro-Ni are comparable to the theoretical values (**Table 4.1**). To calculate the roughness factor of a n half-layer Hi-Ni electrode, the roughness factor of the one half-layer sample is used as a reference value ($R_f = 6.9$). Again, the experimental results are rather close to the theoretical values.

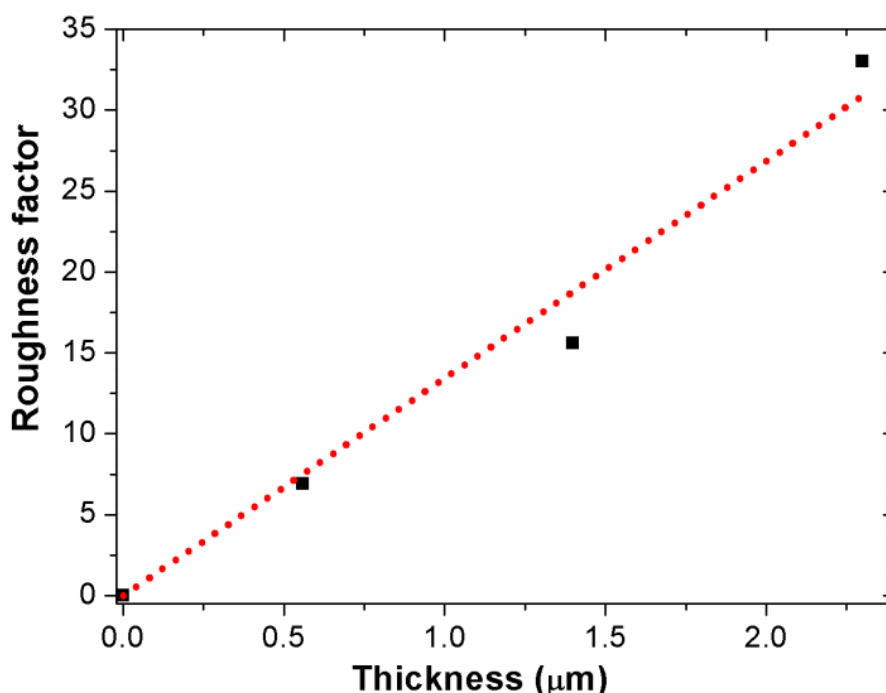


Figure 4.8 Roughness factor as a function of film thickness of Hi-Ni.

Electrocatalytic oxygen evolution reaction (OER)

In order to present the advantageous effect of hierarchical multiporous nickel nanosheets, the electrocatalytic performance of multiporous nickel films was studied for electrocatalytic OER via linear sweep voltammetry (LSV) in alkaline solution of N₂-saturated 1 M KOH in the potential window from 1.2 to 1.8 V vs RHE at a scan rate of 5 mV s⁻¹. [Figure 4.9](#) represents the different LSVs with the current density being defined as the current divided by the geometric surface area. Theoretically, in alkaline solution, nickel is oxidized in the potential range from 1.3 to 1.4 V vs RHE, indicated by the small peak in [Figure 4.9a](#). The onset potential for oxygen evolution for the different nickel electrodes was measured by linear extrapolation of the catalytic OER curves according to current recommendations. Compared to flat Ni with a similar film thickness, the OER onset potential for Meso-Ni, Macro-Ni and Hi-Ni is only slightly lower (1.56, 1.55 and 1.53 V vs RHE, respectively, instead of 1.57 V for flat Ni), which is not so surprising because for the same class of material/composition, one would expect more or less identical onset potentials for OER. The fact that here the potentials are slightly varying might indicate that

not only the morphology is changing as a function of the type of electrodeposit, but also the ratio between different oxidized nickel species (NiO and Ni(OH)₂) and the degree of crystallinity.

Most importantly, the electrocatalytic OER performance of Hi-Ni is significantly improved as can be seen from the higher current density compared to electrodes with a single type of porosity. This increase is due to the synergy between the high surface area of the mesoporous nanosheet structure and the improved mass transfer enabled by the macroporous structure, eventually also accelerating the evacuation of oxygen from the internal part of the porous structure.

The apparent onset potential for OER is also only slightly decreasing from 1.55 and 1.53 to 1.52 V when measuring one, three and five half-layer Hi-Ni electrodes, for the same reasons as mentioned above ([Figure 4.9b](#) and [Table 4.2](#)). To further evaluate the performance of these electrodes we estimate the driving force necessary to achieve a current density of 10 and 100 mA⁻², which are values comparable to what is used in solar to fuel conversion systems. Generally, flat Ni requires an operating potential of 1.63 V, or more than 1.80 V to obtain a current density of 10 mAcm⁻² and 100 mAcm⁻², respectively.[245-248] Interestingly, in the case of five half-layer Hi-Ni, a significantly lower operating potential of 1.52 and 1.65 V is needed for a current density of 10 mAcm⁻² and 100 mAcm⁻², respectively. These observations again confirm that the two-step electrodeposition, generating hierarchical structures, can improve the overall electrocatalytic performance for OER.[205] Although the values are not record numbers,[249] it shows that a controlled surface design allows gradual fine-tuning of the activity, in the present case essentially because the architecture considerably improves the transport processes in the porous structure and therefore the total current.

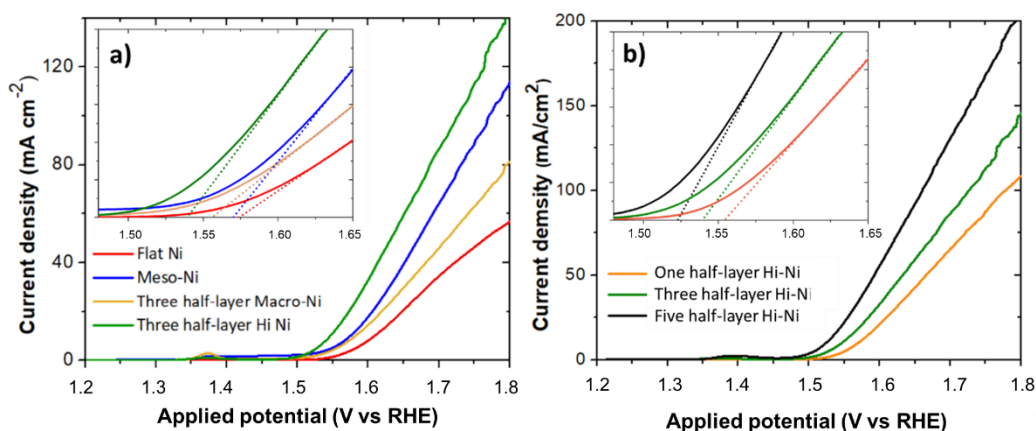


Figure 4.9. Linear sweep voltammograms (LSVs) for various nickel electrodes measured in N_2 -saturated 1 M KOH electrolyte at a scan rate of 5 mV s^{-1} ; (a) Effect of the type of nickel electrodes on OER activity: flat Ni (red), Meso-Ni (blue), three half-layer Macro-Ni (yellow), and three half-layer Hi-Ni (green); (b) Effect of the number of electrodeposited macroporous layers on OER activity: one half-layer Hi-Ni (orange), three half-layer Hi-Ni (green), and five half-layer Hi-Ni (black).

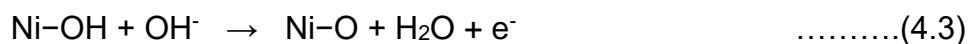
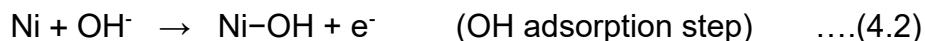
Table 4.2. OER onset potentials and corresponding Tafel slopes of various nickel electrodes measured by LSV in N_2 saturated 1 M KOH electrolyte at a scan rate of 5 mVs^{-1} .

Electrode type	Onset potential	Tafel slope
	(V)	(mV dec^{-1})
Flat Ni	1.568	92.6
Meso-Ni	1.564	86.6
One-half-layer Macro-Ni	1.563	88.9
Three-half layer Macro-Ni	1.55	88.5
One-half layer Hi-Ni	1.553	60.5
Three-half layer Hi-Ni	1.533	59.3
Five-half layer Hi-Ni	1.517	58.7

To gain insights into the mechanistic details of the OER for the different nickel materials, their electrocatalytic performance is examined by recording the

corresponding Tafel plots ($\eta = b \times \log(j/j_0)$, where b is the Tafel slope, j is current density and j_0 is the exchange current density). The overpotential was renormalized with respect to E_{RHE} and calculated based on the thermodynamic value ($\eta = E_{\text{vsAg/AgCl}} + 0.197 \text{ V} + 0.059 \text{ pH} - 1.23 \text{ V}$). Under the present experimental conditions, flat Ni, Meso-Ni, Macro-Ni and Hi-Ni exhibit Tafel slopes in the range from 58 to 93 mVdec⁻¹ (Figure 4.10a).

Typically, the OER mechanism can be divided into three elementary steps (Equations 4.2–4). The first OER step involves the OH adsorption on the nickel surface (Ni-OH, Equation 4.2). The adsorbed OH species is then transformed into adsorbed O (Ni-O, Equation 4.3) and finally, O₂ gas can be produced and released from the metal surface (Ni + O₂, Equation 4.4). From the Tafel slopes in Table 4.2, it is possible to deduce the rate-determining step (RDS) of the electrocatalytic OER if certain precautions are taken.[250] As above-mentioned, Tafel slopes for the hierarchical nickel electrodes are close to 60 mVdec⁻¹, this seems to indicate that the RDS relates to the electron transfer during the NiO formation step.[230, 245-247]



However, Tafel slopes of single pore type structures and flat Ni are above 60 mV dec⁻¹. This might result from a change in the rate controlling step and the material preparation method.[251-253] Theoretically, a lower Tafel slope represents a higher reactivity for OER. The Tafel slopes of various nickel electrodes, flat Ni, Meso- Ni, three half-layer Macro-Ni and three half-layer Hi-Ni, having a similar film thickness, are 92.6, 86.6, 88.5 and 59.3 mV dec⁻¹, respectively. The electrodeposited Hi-Ni benefits from the synergy between the two types of porosity and exhibits a lower Tafel slope compared to an electrode with a single type of porosity (Meso-Ni or Macro-Ni). Interestingly, increasing the number of electrodeposited macroporous layers allows increasing the OER performance. One could think that increasing further the thickness of the porous layer might still lead to a further improvement of the catalytic currents, however as we could show recently by modeling and by independent experiments with

electroenzymatic reactions, there is an upper limit, above which it doesn't make sense to further increase the thickness of the porous layer due to diffusion limitations.[252-254] The size of the macropores might also have an impact on the OER behavior. It is reasonable to assume that for a given number of pore layers the current should increase with the diameter of the pores. This is due to the fact that actually the active surface area of macroporous electrodes normally only depends on the number of pore layers, but not on their diameter, however the diffusional transport should be facilitated when the pores become larger.

In the **Figure 4.10b**, the Tafel slope significantly decreases to 58.7 mVdec⁻¹ for five half-layer Hi-Ni, compared to the conventional Ni electrode (92.6 mVdec⁻¹), which can show different values depending on its composition.[41] Tafel slopes can also be influenced by a low efficiency of current conduction in the solid portion of the film and in the pores. The related ohmic drop may strongly affect the characteristic catalytic features, but this doesn't seem to be the case for the present hierarchical structures.[189]

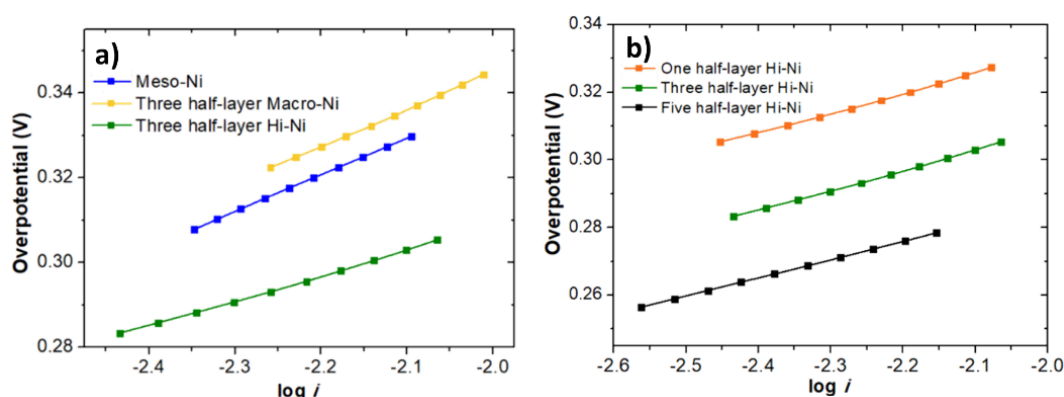


Figure 4.10 Tafel plots measured in N₂-saturated 1 M KOH solutions calculated from LSVs for (a) various types of nickel electrodes; Meso-Ni (blue), three-half layer Macro-Ni (yellow), and three half-layer Hi-Ni (green), (b) various Hi-Ni electrodes prepared with different number of deposited half-layers; one half-layer Hi-Ni (orange), three half-layer Hi-Ni (green), five half-layer Hi-Ni (black).

In addition to the reactivity, an important aspect in catalytic systems is the stability of the electrochemical activity. This was investigated by chronoamperometry in 1 M KOH at an applied potential of 1.52 and 1.72 V (vs.

RHE) for 2 h, as illustrated in [Figure 4.11](#). At 1.52 V ([Figure 4.11a](#)), the average current density of three half-layer Hi-Ni is 6.3 mA cm^{-2} , which represents the best electrochemical performance and stability, whereas the measured current densities of Meso-Ni, Macro-Ni, and flat-Ni are significantly lower; in particular, the current density of flat Ni is only 1.2 mA cm^{-2} . A structure with only five half-layers of Hi-Ni leads already to a current enhancement of around one order of magnitude compared to a flat surface. At a higher applied potential of 1.72 V, flat Ni represents unsatisfactory stability of the signal with a rapid decrease in current density already after a few seconds as shown in [Figure 4.11b](#). In contrast to this, Hi-Ni exhibits a much better current stability at the same applied potential. In addition, a gradual increase of current density was obtained for Hi-Ni as a function of the number of deposited layers ([Figures 4.11c and 4.11d](#)). The less pronounced decay in current for these latter electrodes might come from the fact that the formation of (nano)bubbles that often block the surface is less favorable on such structured interfaces, compared to a flat electrode where bubbles can stick more easily.[51] It should be noted that after the electrodes were used for the electrocatalytic reaction, their roughness factor increased ([Table 4.1](#)). We suppose that the continuous evolution of gas creates mechanical stress in the porous structures and therefore results in a further roughening of the material as can be seen from the SEM images in [Figure 4.12](#).

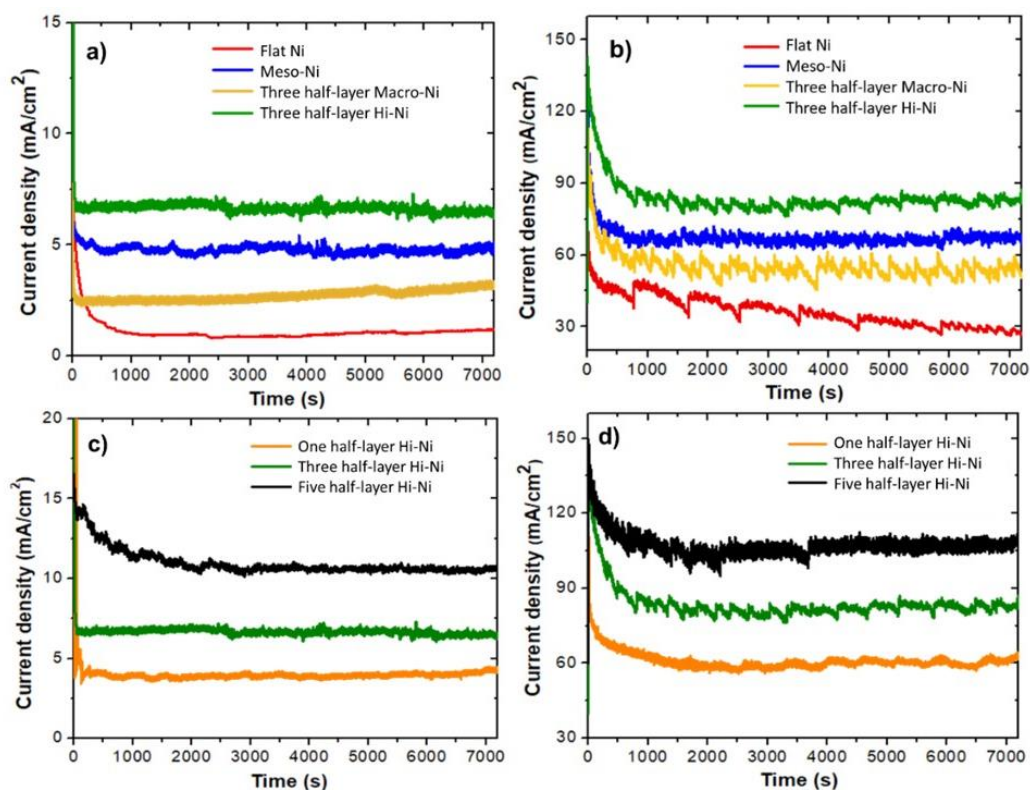


Figure 4.11 Chronoamperometry in 1 M KOH with various nickel electrodes at two different applied potentials; (a, b) Effect of the type of nickel on the electrocatalytic activity and stability, flat Ni (red); mesoporous Ni (blue); macroporous Ni (yellow) and hierarchical porous Ni (green) at an applied potential of 1.52 and 1.72 V (vs RHE), respectively. (c, d) Effect of the number of the deposited layers of hierarchical porous Ni on the electrocatalytic activity and stability; one half-layer (orange), three-half layer (green) and five-half layer (black) at a potential of 1.52 mV and 1.72 (vs Ag/AgCl), respectively.

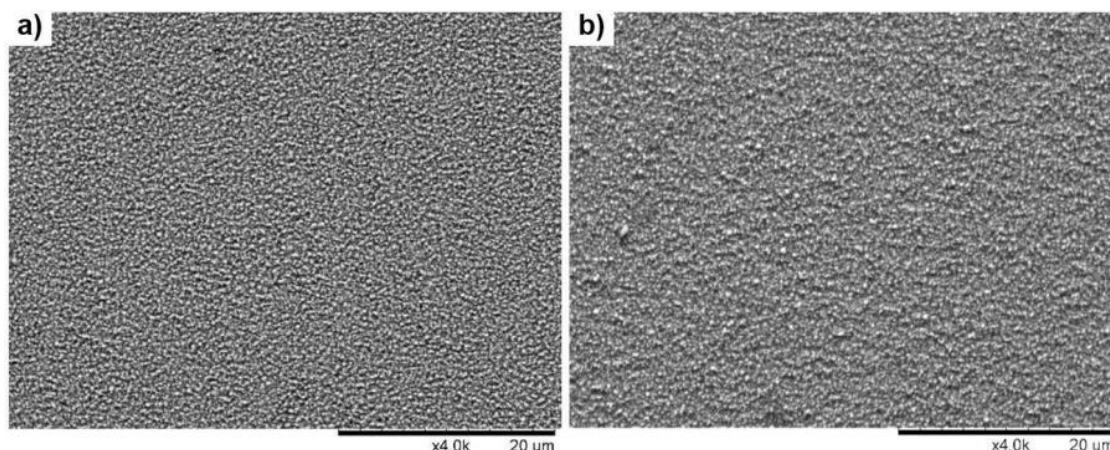


Figure 4.12 Surface morphology comparison of Meso-Ni at a) before and b) after catalytic testing.

4.4 Conclusion

In this work, we have successfully developed hierarchically structured porous nickel electrodes via a two-step electrodeposition process in the presence of silica beads and surfactant as templates to control the macro- and mesoporous structure, respectively. Highly ordered hierarchical porous structures with nanosheet morphologies improve the electrocatalytic active surface area compared to nickel with a single porosity. In addition, the synergetic effect of mesoporous and macroporous structures enhances the electrocatalytic current density by one order of magnitude and also improves the stability. This well-controlled design of multiporous structures constitutes a promising concept in the frame of the development of electrocatalysts for water splitting applications and might be also extended to other electrode materials.

Chapter 5

Thesis perspectives

The presented studies, which have been performed in this thesis, were focusing on the following aspects: (i) the enantioselective electrosynthesis of chiral compounds at chiral imprinted mesoporous noble and non-noble metals such as platinum and nickel, based on a promising strategy, namely pulsed electrochemical conversion; (ii) the chiral discrimination of racemic tryptophan, tyrosine and naproxen in the microchannel of a microfluidic device, modified with chiral-encoded platinum as a conductive stationary phase, fine-tuned by applying a potential; (iii) the enantioselective actuation of chiral imprinted platinum-polypyrrole hybrid films with dual functionality, combining polymer deformation and chiral recognition in mandelic acid solutions triggered by bipolar electrochemistry; (iv) the electrocatalytic oxygen evolution reaction in alkaline media using specifically designed hierarchical macro- and mesoporous nickel nanosheet electrodes.

As for the first work, not only noble metals such as platinum but also earth-abundant non-noble metals, such as nickel, could be used as an alternative for encoding chiral information. The chiral-encoded mesoporous nickel electrodes have been successfully electrodeposited in the presence of phenylethanol, nickel salt and a lyotropic liquid crystal as a chiral template, metal source and mesoporegen, respectively. The presence of mesopores, the elemental composition and the chiral recognition properties of the prepared electrodes were confirmed by electrochemical characterization. Moreover, asymmetric synthesis using an original technique, namely pulsed electroconversion, has been introduced to improve the enantiomeric excess with respect to conventional steady-state electrosynthesis. The promising results open up new perspectives for chiral synthesis. Firstly, this example allowed extending the concept of using earth-abundant transition metals instead of platinum. However, due to the low stability of earth-abundant metals and a lower selectivity for hydrogenation, the efficiency of monometallic non-noble metals

should be improved, for example, by combining with other metals such as platinum and palladium to produce molecularly encoded bimetallic surfaces. Such advanced materials could increase the stability and electrocatalytic performance for hydrogenation with chiral metal films. Although the use of pulsed electrochemistry for electroreduction of prochiral molecules can greatly improve the enantiomeric excess, the conditions of pulsed synthesis require a very long time for the synthesis due to a long relaxation period. Therefore, three parameters including pulse time, relaxation time and applied potential, need to be optimized in the future. Subsequently, because of diffusion limitations of reactants and products in the mesopores, the introduction of additional macropores could help to improve these transport problems. By the combination of mesoporous and macroporous structures, the synergistic effect of both porous structures would lead to a high electroactive surface area and good mass transport. Finally, in this work chiral phenylethanol was chosen as a model template, however, none of the literature reports have used pharmaceutical compounds as chiral template molecules. Therefore, the most interesting perspective of this part of the work is replacing the phenylethanol template by real pharmaceutical compounds, for example naproxen.

Concerning the second part, chiral imprinted mesoporous platinum was used for the first time as a chiral stationary phase in a microfluidic device. Interestingly, by fine-tuning the potential, complete baseline separation of two corresponding enantiomers was observed. However, in this work we also examined the chiral separation of tyrosine and naproxen using chiral platinum imprinted with tryptophan. Although complete baseline separation could not be observed in this case, the length of the stationary phase and the density of imprinted site might be optimized in order to increase the chiral separation efficiency. In addition, because the chiral stationary phase was made out of Pt, which is a precious and expensive metal, it would also be interesting to test earth-abundant metals and bimetallic materials as a stationary phase in the future. Moreover, the concept might be extended also to the separation of mixtures of non-chiral compounds. Besides, such a microfluidic device could also be used as a microreactor with a continuous flow of reactants along the

microchannel. In such a case, the advantages of chiral imprinted mesoporous platinum would allow simultaneously the enantioselective synthesis and the separation of by-products.

With respect to the third part of the work, a free-standing film of hybrid chiral imprinted Pt-PPy was electrodeposited and electropolymerized by a two-step preparation concept, and subsequently used as an enantioselective actuator. The unique features of both components, chiral recognition and wireless actuation abilities, were combined in a synergistic way. The use of such a wireless actuator might be extended to the analysis of other chiral molecules, for instance amino acids, DOPA and phenylethanol. The possibility of a direct readout with naked eyes might be advantageous for the design of a portable detector for real-time detection, which can quantitatively measure chiral compounds. However, the sensitivity of the chiral recognition still needs to be improved. For the moment, the chiral information is only in the platinum matrix, but it might be also interesting to imprint the polypyrrole part and in this way enhance the recognition efficiency.

Apart from the design of mesoporous materials with a single type of porosity, in this work we also illustrated the concept of hierarchical macro-mesoporous metals for the electrocatalytic oxygen evolution reaction in basic media. In this case, a hierarchically structured porous electrode has been successfully prepared by the two-step electrodeposition of nickel in the presence of a hard and a soft template. The electrocatalytic performance and stability of the multiporous electrode was greatly improved compared to electrodes with a single type of porosity or flat electrodes. However, with a pure nickel surface, the system requires rather high overpotential, and therefore, to overcome this drawbacks, bimetallic or trimetallic materials, such as NiFe and NiFeMo should be studied. In order to tackle real energy conversion applications, water splitting needs the combination of two reactions, oxygen evolution reaction and hydrogen evolution reaction. Therefore the results of this work might be extended to hydrogen evolution and subsequently both porous electrodes could be combined. Moreover, in order to create an advanced system for water splitting, it would be an interesting perspective to combine such a cell with a solar cell.

In summary, this thesis demonstrated that porous materials are very useful for a wide range of potential applications including catalysis, separation, synthesis and analysis. The design of porous matrices can be perfectly controlled by the use of a soft and/or hard template, leading to structures with unique and fascinating properties, that have many promising perspectives in various areas, including the pharmaceutical and medical sector and energy conversion.

Design de Matériaux Poreux pour des Applications Électrochimiques

Résumé

Sunpet Assavapanumat

La conception de matériaux poreux hautement ordonnés est l'une des stratégies cruciales qui est largement utilisée dans le domaine l'ingénierie des matériaux. La génération d'une porosité hautement contrôlée offre des avantages remarquables tels qu'une structure ordonnée, une grande surface active, une sélectivité de forme et un système de pores interconnectés en trois dimensions. Par conséquent, les efforts de recherche dans le cadre de matériaux poreux ordonnés ont été concentrés sur la conception, la synthèse et les applications, notamment dans les domaines de l'analyse, de la catalyse, de l'adsorption, de la séparation ou de la conversion et du stockage de l'énergie. Diverses stratégies de synthèse pour les matrices poreuses ont été étudiées et développées au cours des dernières décennies et on peut conclure que les stratégies les plus efficaces pour la synthèse de structures poreuses avancées sont basées sur des approches de type « template ». Elles peuvent être classées en deux familles en fonction du type de template ou moule utilisé lors de la synthèse des matériaux poreux: (i) les moules souples et (ii) les moules durs. Dans le premier cas la porosité est introduite dans la matrice en utilisant des molécules amphiphiles, qui sont composés d'une tête hydrophile et d'une queue hydrophobe pour former des micelles ou des cristaux liquides lyotropes. La structure et la porosité du matériau synthétisé peuvent être facilement contrôlées par la concentration, la température et les types de tensioactifs utilisés. De manière complémentaire, les moules durs sont également très intéressant pour obtenir des matériaux poreux avec une structure bien définie. Le matériau poreux synthétisé reproduit le moule avec une morphologie inverse. En raison des caractéristiques bénéfiques complémentaires des structures

poreuses obtenues, nous avons concentré nos travaux sur les propriétés électrochimiques et l'utilisation de matériaux poreux hautement ordonnés qui sont préparés via des méthodes utilisant des moules durs et/ou mous.

Pour la synthèse de matériaux nanostructurés, l'électrodéposition de platine mésoporeux a été largement étudiée en présence d'une phase cristalline liquide lyotrope, conduisant à une structure poreuse bien définie et une grande surface spécifique. [1] Le platine mésoporeux à empreinte chirale a été préparé par électrodéposition de platine en présence d'une certaine quantité d'un tensioactif non-ionique et de molécules chirales pour façonner la matrice, ce qui améliore significativement la surface électroactive et permet de discriminer deux énantiomères. [2] En raison des avantages de la reconnaissance asymétrique sur les surfaces poreuses, du platine mésoporeux avec une empreinte chirale a été utilisé pour la synthèse asymétrique de composés chiraux, conduisant à un excès énantiomérique des molécules chirales correspondantes d'environ 20%. [3]

Dans cette thèse, le platine mésoporeux à empreinte chirale a d'abord été utilisé comme électrocatalyseur pour la synthèse énantiomérique via des méthodes électrochimiques conventionnelles. Cependant, en raison de la présence de sites non imprimés sur les surfaces externes des électrodes et des limitations de diffusion du réactif et du produit dans les canaux mésoporeux, seul un faible excès énantiomérique a été observé. Par conséquent, un autre concept d'électrosynthèse a été proposé, appelé "électroconversion pulsée", où les limitations de diffusion des composés dans les mésopores sont minimisées en contrôlant les périodes d'électroréduction et les temps de relaxation. [4] Dans ce cas, l'électrochimie pulsée permet d'atteindre un excès énantiomérique supérieur à 90%. De plus, afin d'étendre la portée de la synthèse asymétrique, un métal alternatif qui est un métal non-noble, abondant et bon marché comme le nickel, a été étudié. [5] Les surfaces conçues permettent non seulement une discrimination énantiosélective entre deux configurations chirales en utilisant l'électrosynthèse conventionnelle, mais, plus important encore, un excès énantiomérique important allant jusqu'à 80% a été obtenu dans des conditions pulsées. Par conséquent, ces résultats représentent une extension cruciale du

concept d'électrosynthèse pulsée et d'impression chirale aux métaux non-nobles utilisés pour la synthèse de produits chiraux à haute valeur ajoutée.

De plus, nous avons également concentré nos efforts de recherche sur la possibilité d'utiliser de telles structures métalliques pour la séparation/élimination de la configuration chirale non-souhaitée après une synthèse asymétrique. En effet, certains énantiomères peuvent présenter un effet négatif sur des systèmes biologiques tels que les enzymes ou le corps humain, nécessitant la séparation et la purification des mélanges racémiques afin d'obtenir un seul énantiomère. Par conséquent, l'ajustement du potentiel électrique d'une surface chirale a été proposé pour contrôler l'énantioaffinité, permettant d'optimiser l'interaction entre les molécules chirales, telles que le tryptophane, et les surfaces de platine mésoporeuses à empreinte chirale, qui ont été utilisées comme phase stationnaire chirale dans des dispositifs microfluidiques. [6] Ce concept est basé sur une amélioration des interactions électrostatiques entre les molécules déprotonées, chargées négativement, et la surface de platine chargée positivement. Pour des potentiels appropriés, les surfaces métalliques à empreinte chirale montrent également une stabilité élevée, même après un mois. De plus, des molécules pharmaceutiques peuvent être séparées dans ces canaux de platine imprimés. Par conséquent, cette approche est une stratégie simple et prometteuse pour enrichir la panoplie des technologies basées sur la reconnaissance chirale, en raison des propriétés énantiomériques, de la stabilité élevée et de la simplicité de fabrication de ces surfaces métalliques.

Enfin, le platine mésoporeux à empreinte chirale a été combiné dans un matériau hybride avec un polymère conducteur, le polypyrrole (PPy), afin de bénéficier de la synergie des propriétés spécifiques de ces deux composants. Récemment, des films PPy ont été intégrés dans une expérience d'électrochimie bipolaire pour développer des actionneurs sans fil.[7] Les films hybrides chiraux platine-PPy ont été synthétisés par électrodéposition de platine imprimé avec une information chirale et par électropolymérisation du pyrrole. Les caractéristiques uniques des deux composants, la reconnaissance chirale et les capacités d'actionnement sans fil, ont été combinées pour développer des

actionneurs énantiosélectifs. Le concept sous-jacent d'électrochimie bipolaire permet l'oxydation sélective d'un énantiomère par le métal chirale, tandis que le polymère subit un processus de réduction correspondant, couplé à une libération d'anions. Cela conduit à une déformation contrôlée du film de polymère, agissant comme un signal de lecture des informations chirales. Cette approche polyvalente ouvre des perspectives intéressantes allant bien au-delà de simples considérations analytiques, car un tel matériau hybride peut également être considéré comme l'équivalent biomimétique d'un muscle qui n'est activé que par un stéréoisomère, représentant ainsi la version artificielle de schémas d'actionnement énantiosélectifs dans le corps.

Outre l'approche utilisant un moule souple pour créer un seul type de pores, l'emploi d'un moule dur est une autre méthode intéressante pour la synthèse de nanostructures poreuses qui reproduisent l'inverse de la structure du moule. Par conséquent, des nanofeuilles de nickel multiporeuses ont été synthétisées par une électrodéposition de nickel en deux étapes en présence de billes de silice et un assemblage de tensioactif non-ionique, afin de générer simultanément une structure macro- et mésoporeuse. Les nanofeuilles de nickel avec une porosité hiérarchique ont été utilisées pour étudier l'évolution électrocatalytique de l'oxygène, qui est d'une importance majeure dans le domaine de la conversion et du stockage de l'énergie. Fait intéressant, l'effet synergique de ces structures méso- et macroporeuses hautement ordonnées peut augmenter les performances électrocatalytiques pour la réaction de dégagement d'oxygène d'un ordre de grandeur en termes de densité de courant par rapport aux électrodes en nickel conventionnelles, combinées avec une meilleure stabilité. Ainsi, cette conception avancée de nickel multiporeux conduit à une structure remarquable et à des performances électrocatalytiques nettement améliorées et très prometteuses.

Mots clés: Impression moléculaire; Métaux mesoporeux; Reconnaissance chirale; Énantiosélectivité; Énantioaffinité; Porosité hiérarchique; Electrocatalyse

Design of Porous Materials for Electrochemical Applications

Summary

Sunpet Assavapanumat

The advanced design of highly ordered porous materials is one of the crucially important strategies that is widely used for material engineering. The controlled porosity provides remarkable advantages such as a sophisticated structure, a large interfacial area, shape selectivity and a three-dimensionally interconnected pore system. Thus, research efforts in the frame of highly ordered porous materials have been devoted to the design, synthesis and application, for instance in the field of analysis, catalysis, adsorption, separation and energy conversion or storage. Various synthesis strategies for porous matrices have been studied and developed over the last decades, and it can be concluded that the most efficient strategies for advanced synthesis of porous frameworks are templating methods. They can be categorized into two families: (i) soft templating approach and (ii) hard templating approach, which are classified by the type of template used during the porous material synthesis. Firstly, a soft template introduces porous structures in the matrix by using amphiphilic molecules, composed of a hydrophilic head and a hydrophobic tail, to form micelles or lyotropic liquid crystals. The structure and porosity of the synthesized material can be easily controlled by concentration, temperature and types of surfactants. Secondly, a hard template is a convenient preparation method to obtain porous materials with a well-defined structure. The synthesized porous material replicates the template with the inverse morphology of the mold. Due to the complementary beneficial features of the obtained porous structures, we have focused our work on the electrochemical utility of highly ordered porous materials that are prepared via soft and/or hard templating methods.

For the synthesis of nanostructured materials, the electrodeposition of mesoporous platinum has been extensively studied in the presence of a

lyotropic liquid crystalline phase with a well-defined mesoporous structure and high specific surface area.[1] Chiral imprinted mesoporous platinum has been prepared via electrodeposition of platinum salt in the presence of a certain amount of a non-ionic surfactant and chiral template molecules, resulting in significantly enhanced electroactive surface area and discrimination between two enantiomers. [2] Due to the benefits of asymmetric recognition on the porous surfaces, chiral encoded mesoporous platinum has been employed for the asymmetric synthesis of chiral compounds, leading to an enantiomeric excess of the corresponding chiral molecules of about 20%. [3]

In this thesis, chiral encoded mesoporous platinum has been first used as electrocatalyst for enantiomeric synthesis with conventional electrochemistry. However, because of the non-imprinted site at the external electrode surfaces and diffusion limitations of reactant and product in the mesoporous channels, only low enantiomeric excess has been observed. Therefore, a new concept of electrosynthesis has been proposed which is called “pulsed electroconversion”, in which the diffusion limitations of the compounds in the mesoporous framework are minimized by controlling the electroreduction time and relaxation time.[4] In strong contrast, pulse electrochemistry allows reaching an enantiomeric excess of above 90%. Moreover, in order to extend the scope of asymmetric synthesis, an alternative metal which is a non-noble, abundant and cheap metal, such as nickel, has been investigated.[5] The designed surface layers not only allow the enantioselective discrimination between two chiral configurations using conventional electrosynthesis, but also a very significant enantiomeric excess of up to 80% has been obtained when using pulsed synthesis. Therefore, these results are a crucial extension of the concept of pulsed electrosynthesis and chiral imprinting to non-noble metals employed for the chiral synthesis of high-added-value products.

In addition, we were also focusing our research efforts on the possibility to use such metal structures for the separation/removal of the undesired chiral configuration after asymmetric synthesis. As some enantiomers can exhibit a negative effect on biological systems such as enzymes or the human body, racemic mixtures need to be separated and purified in order to obtain a single

enantiomer. Therefore, the concept of potential induced fine-tuning of the enantioaffinity has been proposed, allowing to improve the binding affinity of chiral molecules, such as tryptophan, on chiral imprinted mesoporous platinum surfaces which has been employed as a chiral stationary phase of microfluidic devices.[6] This concept is based on the additional electrostatic interactions between deprotonated, negatively charged, molecules and the positively charged platinum surface. Consequently, the binding affinity can be fine-tuned by controlling the external potential. At a suitable applied potential, the chiral imprinted metal surfaces also present a high stability even after operating for a month. Furthermore, even pharmaceutically relevant molecules can be separated in these imprinted platinum channels. Therefore, this approach is a straightforward and promising strategy for chiral technologies due to the tunable enantiomeric properties, high stability and facile fabrication.

Finally, chiral encoded mesoporous platinum has been combined in a hybrid material together with conductive polypyrrole (PPy) in order to benefit in a synergistic way from the specific properties of these two components. Recently, PPy free-standing films have been integrated in a bipolar electrochemical set-up which can be used for the developing wireless actuators.[7] The chiral platinum-PPy hybrid films have been synthesized by electrodeposition of chiral encoded platinum and electropolymerization of pyrrole. The unique features of both components, chiral recognition and wireless actuation abilities, are combined in a synergistic way for developing enantioselective actuators. The underlying concept of bipolar electrochemistry allows the selective oxidation of one enantiomer at the chiral metal, whereas the polymer undergoes a corresponding reduction process, coupled with a release of anions. This leads to a controlled deformation of the polymer film, acting as a readout signal of the chiral information. This versatile approach opens up interesting perspectives going far beyond pure analytical considerations, because such a hybrid material can be considered as the biomimetic equivalent of a muscle, which is activated only by one stereoisomer, thus representing the artificial version of enantioselective actuation schemes in the body.

Apart from the soft templating approach for creating a single type of pore structures, hard templating is another interesting method for the synthesis of porous nanostructures which inversely replicate the structure of the hard template. Hence, multiporous nickel nanosheets have been synthesized by a templated two-step electrodeposition of nickel in the presence of silica beads and an assembly of nonionic surfactant in order to generate a combined macro- and mesoporous structure. The hierarchical multiporous nickel nanosheets have been used for electrocatalytic oxygen evolution (OER), which is a crucially important ingredient for energy conversion and storage. Interestingly, the synergistic effect of these highly ordered meso- and macroporous structures can increase the electrocatalytic performance for oxygen evolution reaction by one order of magnitude in terms of current density compared to conventional nickel electrodes, combined with a better stability. This advanced design of multiporous nickel leads to a remarkable structure and significantly improved electrocatalytic performance in various electrochemical applications.

Keywords: Molecular imprinting, Mesoporous metals, Chiral recognition, Enantioselectivity, Enantioaffinity, Hierarchical porosity, multiporous nickel nanosheets, Electrocatalysis

References

1. Attard GS, Bartlett PN, Coleman NRB, Elliott JM, Owen JR, Wang JH. Mesoporous platinum films from lyotropic liquid crystalline phases. **Science**. 1997;278(5339):1997.
2. Wattanakit C, Come YB, Lapeyre V, Bopp PA, Heim M, Yadnum S, Nokbin S, Warakulwit C, Limtrakul, Kuhn A. Enantioselective recognition at mesoporous chiral metal surfaces. **Nature Communications**. 2014;5:3325.
3. Yutthalekha T, Wattanakit C, Lapeyre V, Nokbin S, Warakulwit C, Limtrakul J, Kuhn A. Asymmetric synthesis using chiral-encoded metal. **Nature Communications**. 2016;7:12678.
4. Wattanakit C, Yutthalekha T, Assavapanumat S, Lapeyre V, Kuhn A. Pulsed electroconversion for highly selective enantiomer synthesis. **Nature Communications**. 2017;8(1):2087.
5. Assavapanumat S, Ketkaew M, Kuhn A, Wattanakit C. Synthesis, characterization and electrochemical applications of chiral imprinted mesoporous Ni surfaces. **Journal of the American Chemical Society**. 2019;141(47):18870-18876.
6. Assavapanumat S, Yutthalekha T, Garrigue P, Goudeau B, Lapeyre V, Perro A, et al. Potential-induced fine-tuning of the enantioaffinity of chiral metal phases. **Angewandte Chemie International Edition**. 2019;58(11):3471-3475.
7. Gupta B, Goudeau B, Kuhn A. Wireless electrochemical actuation of Conducting Polymers. **Angewandte Chemie International Edition**. 2017;56(45):14183-14186.
8. Yaghi OM, O'Keeffe M, Ockwig NW, Chae HK, Eddaoudi M, Kim J. Reticular synthesis and the design of new materials. **Nature**. 2003;423:705-714.
9. Zhou M, Shen L, Lin X, Hong Y, Feng Y. Design and pharmaceutical applications of porous particles. **RSC Advances**. 2017;7(63):39490-39501.
10. Xue S, Wang Y, Wu D, Shen J, Wei Y, Wang C. Core-shell structured magnetic mesoporous carbon nanospheres derived from metal-polyphenol coordination polymer-coated Fe₃O₄ and its application in the enrichment of phthalates from water samples. **Journal of Separation Science**. 2019;42(23):3512-3520.

11. Jiang SP. Functionalized mesoporous structured inorganic materials as high temperature proton exchange membranes for fuel cells. **Journal of Materials Chemistry A**. 2014;2(21):7637-7655.
12. Halim W, Coste S, Zeroual S, Kassiba A, Ouaskit S. Latex copolymer-assisted synthesis of metal-doped TiO₂ mesoporous structures for photocatalytic applications under solar simulator. **Journal of Materials Science: Materials in Electronics**. 2020;31(5):4161-4169.
13. Omkaramurthy BM, Krishnamurthy G, Foro S. Synthesis and characterization of mesoporous crystalline copper metal–organic frameworks for electrochemical energy storage application. **SN Applied Sciences**. 2020;2(342).
14. Yao RQ, Lang XY, Jiang Q. Recent advances of nanoporous metal-based catalyst: synthesis, application and perspectives. **Journal of Iron and Steel Research International**. 2019;26(8):779-795.
15. Qiu HJ, Kang JL, Liu P, Hirata A, Fujita T, Chen MW. Fabrication of large-scale nanoporous nickel with a tunable pore size for energy storage. **Journal of Power Sources**. 2014;247:896-905.
16. Marcos-Hernández M, Villagrán D. Mesoporous composite nanomaterials for dye removal and other applications. **Composite Nanoadsorbents**. 2019:265-293.
17. Yamauchi Y, Kuroda K. Rational design of mesoporous metals and related nanomaterials by a soft-template approach. **ChemPlusChem**. 2008;3(4):664-676.
18. Letchford K, Burt H. A review of the formation and classification of amphiphilic block copolymer nanoparticulate structures: micelles, nanospheres, nanocapsules and polymersomes. **European Journal of Pharmaceuticals and Biopharmaceuticals**. 2007;65(3):259-269.
19. Coleman NRB, Attard GS. Ordered mesoporous silicas prepared from both micellar solutions and liquid crystal phases. **Microporous and Mesoporous Materials**. 2001;44:73-80.
20. Fan J, Boettcher SW, Tsung CK, Shi Q, Schierhorn M, Stucky GD. Field-directed and confined molecular assembly of mesostructured materials: basic principles and new opportunities. **Chemistry of Materials**. 2008;20:909-921.

21. Soler-Illia GJAA, Azzaroni O. Multifunctional hybrids by combining ordered mesoporous materials and macromolecular building blocks. **Chemical Society Review**. 2011;40(2):1107-1150.
22. Attard GS., Glyde JC, Göltner G. Liquid-crystalline phases as template for the synthesis of mesoporous silica. **Nature**. 1995;378:366-368.
23. Petkovich ND, Stein A. Controlling macro- and mesostructures with hierarchical porosity through combined hard and soft templating. **Chemical Society Review**. 2013;42(9):3721-3739.
24. Attard GS, Corker JM, Goltner CG, Henke S, H.Templer R. Liquid-crystal templates for nanostructured metals. **Angewandte Chemie International Edition**. 1997;109:1372-1374.
25. Sugimoto W, Makino S, Mukai R, Tatsumi Y, Fukuda K, Takasu Y, Yamauchi Y. Synthesis of ordered mesoporous ruthenium by lyotropic liquid crystals and its electrochemical conversion to mesoporous ruthenium oxide with high surface area. **Journal of Power Sources**. 2012;204:244-248.
26. Bartlett PN, Gollas B, Guerin S, Marwan J. The preparation and characterisation of H1-e palladium films with a regular hexagonal nanostructure formed by electrochemical deposition from lyotropic liquid crystalline phases. **Physical Chemistry Chemical Physics**. 2002;4:3835-3842.
27. Nelson PA, Elliott JM, Attard GS, Owen JR. Mesoporous nickel/nickel oxides a nanoarchitected electrode. **Chemistry of Materials**. 2002;14:524-529.
28. Whitehead AH, Elliott JM, Owen JR, Attard GS. Electrodeposition of mesoporous tin films. **Chemical Communications**. 1999;8:331-332.
29. Kijima T, Yoshimura T, Uota M, Ikeda T, Fujikawa D, Mouri S, Uoyama S. Noble-metal nanotubes (Pt, Pd, Ag) from lyotropic mixed-surfactant liquid-crystal templates. **Angewandte Chemie International Edition**. 2004;43(2):228-232.
30. Yamauchi Y, Momma T, Yokoshima T, Kuroda K, Osaka T. Highly ordered mesostructured Ni particles prepared from lyotropic liquid crystals by electroless deposition: the effect of reducing agents on the ordering of mesostructure. **Journal of Materials Chemistry**. 2005;15(20):1987-1994.
31. Guerin S, Attard GS. Electrochemical behavior of electrodeposited nanostructured palladium+platinum films in 2 M H₂SO₄. **Electrochemistry Communications**. 2001;3:544-548.

32. Yamauchi Y, Nair SS, Momma T, Ohsuna T, Osaka T, Kuroda K. Synthesis and characterization of mesoporous Pt–Ni (HI–Pt/Ni) alloy particles prepared from lyotropic liquid crystalline media. **Journal of Materials Chemistry**. 2006;16(23):2229-2234.
33. Yamauchi Y, Yokoshima T, Momma T, Osaka T, Kuroda K. Fabrication of magnetic mesostructured nickel–cobalt alloys from lyotropic liquid crystalline media by electroless deposition. **Journal of Materials Chemistry**. 2004;14(19):2935-2940.
34. Attard GS, Leclerc SAA, Maniquet S, Russell AE, Nandhakumar IS, Bartlett PN. Mesoporous Pt/Ru alloy from the hexagonal lyotropic liquid crystalline phase of a nonionic surfactant. **Chemistry of Materials**. 2001;13:1444-1446.
35. Nandhakumar IS, Gabriel T, Li X, Attard GS, Markham M, Smith DC, Baumberg JJ. Optical properties of mesoporous II–VI semiconductor compound films. **Chemical Communications**. 2004(12):1374-1375.
36. Yamauchi Y, Momma T, Kitoh H, Osaka T, Kuroda K. Fabrication of mesoporous Pt inside micrometer channels via “solvent-evaporation-mediated direct physical casting”. **Electrochemistry Communications**. 2005;7(12):1364-1370.
37. Takai A, Saida T, Sugimoto W, Wang L, Yamauchi Y, Kuroda K. Preparation of mesoporous Pt–Ru alloy fibers with tunable compositions via evaporation-mediated direct templating (EDIT) method utilizing porous anodic alumina membranes. **Chemistry of Materials**. 2009;21(14):3414-3423.
38. Wan Y, Yang H, Zhao D. “Host-Guest” chemistry in the synthesis of ordered nonsiliceous mesoporous materials. **Accounts of Chemical Research**. 2006;39(7):423-432.
39. Yutthalekha T, Warakulwit C, Limtrakul J, Kuhn A. Enantioselective recognition of DOPA by mesoporous platinum imprinted with mandelic acid. **Electroanalysis**. 2015;27(9):2209-2213.
40. Lu AH, Schüth F. Nanocasting: a versatile strategy for creating nanostructured porous materials. **Advanced Materials**. 2006;18(14):1793-1805.
41. Reculosa S, Heim M, Gao F, Mano N, Ravaine S, Kuhn A. Design of catalytically active cylindrical and macroporous gold microelectrodes. **Advanced Functional Materials**. 2011;21(4):691-698.

42. Heim M, Wattanakit C, Reculosa S, Warakulwit C, Limtrakul J, Ravaine S, Kuhn A. Hierarchical macro-mesoporous Pt deposits on gold microwires for efficient methanol oxidation. **Electroanalysis**. 2013;25(4):888-894.
43. Heim M, Rousseau L, Reculosa S, Urbanova V, Mazzocco C, Joucla S, Bouffier L, Bartlett P, Kuhn A, Yvert, B. Combined macro-/mesoporous microelectrode arrays for low-noise extracellular recording of neural networks. **Journal of Neurophysiology**. 2012;108(6):1793-1803.
44. Hu Y, Gu M, Liu X, Zhang J, Huang S, Liu B. Fabrication and performance of Lu₂O₃:Eu³⁺ nanowire arrays with different nanowire diameters. **Optical Materials**. 2019;88:91-96.
45. Reculosa S, Ravaine S. Synthesis of colloidal crystals of controllable thickness through the Langmuir-Blodgett technique. **Chemistry of Materials**. 2003;15(2):598-605.
46. Yang R, Sui C, Gong J, Qu L. Silver nanowires prepared by modified AAO template method. **Materials Letters**. 2007;61(3):900-903.
47. Wirtz M, Martin CR. Template-Fabricated gold nanowires and nanotubes. **Advanced Materials**. 2003;15(5):455-458.
48. Shi ZG, Feng YQ, Xu L, Da SL, Zhang M. A template method to control the shape and porosity of carbon materials. **Carbon**. 2004;42(8-9):1677-1682.
49. Falcaro P, Malfatti L, Kidchob T, Giannini G, Falqui A, Casula MF, Amenitsch H, Marmiroli B, Greci G, Innocenzi. Hierarchical porous silica films with ultralow refractive index. **Chemistry of Materials**. 2009;21(10):2055-2061.
50. Drisko GL, Zelcer A, Luca V, Caruso RA, Soler-Illia GJdAA. One-pot synthesis of hierarchically structured ceramic monoliths with adjustable porosity. **Chemistry of Materials**. 2010;22(15):4379-4385.
51. Ahmed A, Clowes R, Myers P, Zhang H. Hierarchically porous silica monoliths with tuneable morphology, porosity, and mechanical stability. **Journal of Materials Chemistry**. 2011;21(15):5753-5763.
52. Drisko GL, Zelcer A, Caruso RA, Soler-Illia GJdAA. One-pot synthesis of silica monoliths with hierarchically porous structure. **Microporous and Mesoporous Materials**. 2012;148(1):137-144.
53. Parkhomchuk EV, Semeykina VS, Sashkina KA, Okunev AG, Lysikov AI, Parmon VN. Synthesis of polystyrene beads for hard-templating of three-

- dimensionally ordered macroporosity and hierarchical texture of adsorbents and catalysts. **Topics in Catalysis**. 2016;60(1-2):178-189.
54. Bartlett PN, Ghanem MA, El Hallag IS, de Groot P, Zhukov A. Electrochemical deposition of macroporous magnetic networks using colloidal templates. **Journal of Materials Chemistry**. 2003;13(10):2596-2602.
 55. Hussain SA, Dey B, Bhattacharjee D, Mehta N. Unique supramolecular assembly through Langmuir - Blodgett (LB) technique. **Heliyon**. 2018;4(12):e01038.
 56. Heim M, Reculosa S, Ravaine S, Kuhn A. Engineering of complex macroporous materials through controlled electrodeposition in colloidal superstructures. **Advanced Functional Materials**. 2012;22(3):538-545.
 57. Urbanová V, Vytřas K, Kuhn A. Macroporous antimony film electrodes for stripping analysis of trace heavy metals. **Electrochemistry Communications**. 2010;12(1):114-117.
 58. Lu Q, Hutchings GS, Yu W, Zhou Y, Forest RV, Tao R, et al. Highly porous non-precious bimetallic electrocatalysts for efficient hydrogen evolution. **Nature Communications**. 2015;6:6567.
 59. Mandlmeier B, Szeifert JM, Fattakhova-Rohlfing D, Amenitsch H, Bein T. Formation of interpenetrating hierarchical titania structures by confined synthesis in inverse opal. **Journal of the American Chemical Society**. 2011;133(43):17274-17282.
 60. Zhu Y, Li X, Yang J, Wang S, Gao H, Hanagata N. Composition–structure–property relationships of the CaO–MxOy–SiO₂–P₂O₅ (M = Zr, Mg, Sr) mesoporous bioactive glass (MBG) scaffolds. **Journal of Materials Chemistry**. 2011;21(25):9208-9218.
 61. Attard GA. Electrochemical studies of enantioselectivity at chiral metal surfaces. **The Journal of Physical Chemistry B**. 2001;105:3158-3167.
 62. Sannicolò F, Arnaboldi S, Benincori T, Bonometti V, Cirilli R, Dunsch L, Kutner W, Longhih G, Mussini PR, Panigati M, Pierini M, Rizzo S. Potential-driven chirality manifestations and impressive enantioselectivity by inherently chiral electroactive organic films. **Angewandte Chemie International Edition**. 2014;53(10):2623-2627.
 63. Gellman AJ. Chiral surfaces: accomplishments and challenges. **ACS Nano**. 2010;4(1):5-10.

64. Horvath JD, Koritnik A, Kamakoti P, Sholl DS, Gellman AJ. Enantioselective separation on a naturally chiral surface. **Journal of the American Chemical Society**. 2004;126(45):14988-14994.
65. Chen W, Bian A, Agarwal A, Liu L, Shen H, Wang L, Xu C, Kotov NA. Nanoparticle superstructures made by polymerase chain reaction: collective interactions of nanoparticles and a new principle for chiral materials. **Nano Letters**. 2009;9(5):2153-2159.
66. Xiang S, Zhang Y, Xin Q, Li C. Asymmetric epoxidation of allyl alcohol on organic-inorganic hybrid chiral catalysts grafted onto the surface of silica and in the mesopores of MCM-41. **Angewante Chemie International Edition**. 2002;41(5):821-824.
67. Mallat T, Orglmeister E, Baiker A. Asymmetric catalysis at chiral metal surfaces. **Chemical Reviews**. 2007;107(11):4863-4890.
68. Kupai J, Rojik E, Huszthy P, Szekely G. Role of chirality and macroring in imprinted polymers with enantiodiscriminative power. **ACS Applied Materials and Interfaces**. 2015;7(18):9516-9525.
69. Xue YP, Cao CH, Zheng YG. Enzymatic asymmetric synthesis of chiral amino acids. **Chemical Society Reviews**. 2018;47(4):1516-1561.
70. Pavlidis IV, Weiß MS, Genz M, Spurr P, Hanlon SP, Wirz B, Iding H, Bonscheuer UT. Identification of (S)-selective transaminases for the asymmetric synthesis of bulky chiral amines. **Nature Chemistry**. 2016;8(11):1076-1082.
71. Wang D-W, Song C, Feng W, Cai H, Xu D, Deng H, Li H, Zheng D, Zhu X, Wang H, Zhu S-Y, Scully MO. Synthesis of antisymmetric spin exchange interaction and chiral spin clusters in superconducting circuits. **Nature Physics**. 2019;15(4):382-386.
72. Webb G, Wells PB. Asymmetric hydrogenation. **Catalysis Today**. 1992;12(2-3):319-337.
73. Izumi Y. Modified raney nickel (MRNi) catalyst: heterogeneous enantio-differentiating (asymmetric) catalyst. **Advances in Catalysis** 1983;32:215-271.
74. Lorenzo MO, Haq S, Bertrams T, Murray P, Raval R, Baddeley CJ. Creating chiral surfaces for enantioselective heterogeneous catalysis: R,R-tartaric acid on Cu(110). **The Journal of Physical Chemistry B**. 1999;103(48):10661-10669.

75. Akira T, Tadao H, Yuji H, Sigeki M. Stereochemical investigation on asymmetrically modified raney nickel catalyst. mode of interaction between modifying reagent and substrate in the enantioface-differentiating process **Bulletin Chemical Society of Japan**. 1983;56(5):1414-1419.
76. Keane MA, Webb G. The Enantioselective hydrogenation of methyl acetoacetate over supported nickel catalysts. **Journal of Catalysis**. 1992;136:1-15.
77. Christmann M, Bräse S. Asymmetric synthesis more methods and applications. **Wiley-VCH John Wiley & Sons, Hoboken**. 2012.
78. Busacca CA, Fandrick DR, Song JJ, Senanayake CH. The growing impact of catalysis in the pharmaceutical industry. **Advanced Synthesis and Catalysis**. 2011;353:1825-1864.
79. Johnson NB, Lennon IC, Moran PH, Ramsden JA. Industrial-scale synthesis and applications of asymmetric hydrogenation catalysts. **Accounts of Chemical Research**. 2007;40(12):1291-1299.
80. Barbaro P, Liguori F, Linares N, Marrodan CM. Heterogeneous bifunctional metal/acid catalysts for selective chemical processes. **European Journal of Inorganic Chemistry**. 2012;2012(24):3807-3823.
81. Zhao D, Ding K. Recent advances in asymmetric catalysis in flow. **ACS Catalysis**. 2013;3(5):928-944.
82. Yan N, Xiao C, Kou Y. Transition metal nanoparticle catalysis in green solvents. **Coordination Chemistry Reviews**. 2010;254(9-10):1179-1218.
83. Akabori S, Sakurai S, Izumi Y, Fujii Y. An asymmetric catalyst. **Nature**. 1956;178:323-324.
84. Orito Y, Imai S, Niwa S, Nguyen GH. Asymmetric hydrogenation of ethylbenzoylformate using platinum-carbon catalysis modified with cinchonidine. **Journal of Synthetic Organic Chemistry, Japan**. 1979;37:173-174.
85. Molvenger K, Lopez M, Court J. Enantioselective borane reduction of ketones with oxazaborolidines boron-bound to nickel boride nanoparticles. **Tetrahedron Letters**. 1999;40:8375-8378.
86. Makra Z, Szöllősi G, Bartók M. Achiral amine additives in the enantioselective hydrogenation of aliphatic α,β -unsaturated acids over cinchonidine-modified Pd/Al₂O₃ catalyst. **Catalysis Today**. 2012;181(1):56-61.

87. Ye L, Lin H, Zhou H, Yuan Y. Support and size effects of ruthenium catalysts with a chiral modifier for asymmetric hydrogenation of aromatic ketones. **Journal of Physical Chemistry C**. 2010;114(46):19752–19760.
88. Jiang H-Y, Sun B, Zheng X-X, Chen H. Heterogeneous selective hydrogenation of trans-4-phenyl-3-butene-2-one to allylic alcohol over modified Ir/SiO₂ catalyst. **Applied Catalysis A: General**. 2012;421-422:86-90.
89. Gual A, Godard C, Philippot K, Chaudret B, Denicourt-Nowicki A, Roucoux A, Castillón S, Claver C. Carbohydrate-derived 1,3-diphosphite ligands as chiral nanoparticle stabilizers: promising catalytic systems for asymmetric hydrogenation. **ChemSusChem**. 2009;2(8):769-779.
90. Sonnenberg JF, Coombs N, Dube PA, Morris RH. Iron nanoparticles catalyzing the asymmetric transfer hydrogenation of ketones. **Journal of American Chemical Society**. 2012;134(13):5893-5899.
91. Yasukawa T, Miyamura H, Kobayashi S. Chiral metal nanoparticle-catalyzed asymmetric C-C bond formation reactions. **Chemical Society Reviews**. 2014;43(5):1450-1461.
92. McFadden CF, Cremer PS, Gellman AJ. Adsorption of chiral alcohols on “chiral” metal surfaces. **Langmuir**. 1996;12:2483-2487.
93. Ahmadi A, Attard GS. Surface reactivity at “chiral” platinum surfaces. **Langmuir**. 1999;15:2420-2424
94. Sholl DS, Asthagiri A, Power TD. Naturally Chiral Metal Surfaces as enantiospecific adsorbents. **Journal of Physical Chem B**. 2001;105:4771-82.
95. Perez GB, Garzon IL, Novaro O. Ab initio study of small gold clusters. **Journal of Molecular Structure**. 1999;493:225-231.
96. Soler JM, Beltrán MR, Michaelian K, Garzón IL, Ordejón P, Sánchez-Portal D, Artacho E. Metallic bonding and cluster structure. **Physical Review B**. 2000;61:5771.
97. Bravo-Perez G, Garzón IL. Ab initio study of small Au_nS, (n = 1–5) and Au_nS₂, (n = 1–4) clusters. **Journal of Molecular Structure: (THEOCHEM)**. 2002;619:79-89.
98. Chrzanowska AM, Poliwoda A, Wieczorek PP. Surface molecularly imprinted silica for selective solid-phase extraction of biochanin A, daidzein and genistein from urine samples. **Journal of Chromatography A**. 2015;1392:1-9.

99. Alexander C, Davidson L, Hayes W. Imprinted polymers: artificial molecular recognition materials with applications in synthesis and catalysis. **Tetrahedron**. 2003;59(12):2025-2057.
100. Morris RH. Asymmetric hydrogenation, transfer hydrogenation and hydrosilylation of ketones catalyzed by iron complexes. **Chemical Society Reviews**. 2009;38(8):2282-2291.
101. Vasapollo G, Sole RD, Mergola L, Lazzoi MR, Scardino A, Scorrano S, Mele G. Molecularly imprinted polymers: present and future prospective. **International Journal of Molecular Sciences**. 2011;12(9):5908-5945.
102. Turiel E, Martin-Esteban A. Molecularly imprinted polymers for sample preparation: a review. **Analytica Chimica Acta**. 2010;668(2):87-99.
103. Yilmaz E. Improving the application of microbial lipase by bio-imprinting at substrate-interfaces. **World Journal of Microbiology and Biotechnology**. 2002;18:37-40.
104. Khajeh M, Heidari ZS, Sanchooli E. Synthesis, characterization and removal of lead from water samples using lead-ion imprinted polymer. **Chemical Engineering Journal**. 2011;166(3):1158-1163.
105. Attard GS, Glyde JC, Göltner G. Liquid-crystalline phase as templates for the synthesis of mesoporous silica. **Nature**. 1995;378:366-369.
106. Xiao C, Li Y, Lu X, Zhao C. Bifunctional Porous NiFe/NiCo₂O₄/Ni foam electrodes with triple hierarchy and double synergies for efficient whole cell water splitting. **Advanced Functional Materials**. 2016;26(20):3515-3523.
107. Rouya E, Cattarin S, Reed ML, Kelly RG, Zangari G. Electrochemical characterization of the surface area of nanoporous gold films. **Journal of The Electrochemical Society**. 2012;159(4):K97-K102.
108. Kresge CT, Leonowicz ME, Roth WJ, Vartuli JC, Beck JS. Ordered mesoporous molecular sieves synthesized by a liquid crystal template mechanism. **Nature**. 1992;359:710-712.
109. Wattanakit C, Kuhn A. Encoding chiral molecular information in metal structures. **Chemistry**. 2019;26(14):2993-3003.
110. Saurat M, Bringezu S. Platinum group metal flows of Europe, part 1. **Journal of Industrial Ecology**. 2008;12(5-6):754-767.
111. Bullock RM. Abundant metals give precious hydrogenation performance. **Science**. 2013;342:1054-1055.

112. Yang B, Burch R, Hardacre C, Headdock G, Hu P. Origin of the increase of activity and selectivity of nickel doped by Au, Ag, and Cu for acetylene hydrogenation. **ACS Catalysis**. 2012;2(6):1027-1032.
113. Kilgore UJ, Roberts JA, Pool DH, Appel AM, Stewart MP, DuBois MR, et al. $[\text{Ni}(\text{P}(\text{Ph})_2\text{N}(\text{C}_6\text{H}_4\text{X})_2)_2]^{2+}$ complexes as electrocatalysts for H_2 production: effect of substituents, acids, and water on catalytic rates. **Journal of the American Chemical Society**. 2011;133(15):5861-5872.
114. Roche I, Chaînet M, Vondrák J. Carbon-supported manganese oxide nanoparticles as electrocatalysts for the oxygen reduction reaction (ORR) in alkaline medium: physical characterizations and ORR mechanism. **Journal of Physical Chemistry C**. 2007;111(3):1434-1443.
115. Guan YQ, Han Z, Li X, You C, Tan X, Lv H, Zhang X. A cheap metal for a challenging task: nickel-catalyzed highly diastereo- and enantioselective hydrogenation of tetrasubstituted fluorinated enamides. **Chemical Science**. 2019;10(1):252-256.
116. Talmadge MS, Baldwin RM, Biddy MJ, McCormick RL, Beckham GT, Ferguson GA, Czernik S, Magrini-Bair KA, Foust TD, Metelski PD, Hetrick C, Nimlos MR. A perspective on oxygenated species in the refinery integration of pyrolysis oil. **Green Chem**. 2014;16(2):407-453.
117. Sun L, Pei W, Shen C. Synthesis of functionalised acetophenone. **Journal of Chemical Research** 2006;2006(6):388-399.
118. Inoue A. Stabilization of metallic supercooled liquid and bulk amorphous alloys. **Acta Materialia**. 2000;48(1):279-306.
119. Bates JF. Cathodic protection to prevent crevice corrosion of stainless steels in halide media. **Corrosion**. 1973;29:28-32.
120. Pedferri P. Cathodic protection and cathodic prevention. **Construction and Building Materials**. 1996;10(5):391-402.
121. Fanali S. Enantioselective determination by capillary electrophoresis with cyclodextrins as chiral selectors. **Journal of Chromatography A**. 2000;875:89-122.
122. Francotte ER. Enantioselective chromatography as a powerful alternative for the preparation of drug enantiomers. **Journal of Chromatography A**. 2001;906(1-2):379-397.

123. Cheng D, Ishihara Y, Tan B, Barbas CF. Organocatalytic asymmetric assembly reactions: synthesis of spirooxindoles via organocascade strategies. **ACS Catalysis**. 2014;4(3):743-762.
124. Caner H, Groner E, Levy L, Agranat I. Trends in the development of chiral drugs. **Drug Discovery Today**. 2004;9:105-110.
125. Haupt K. Molecularly imprinted polymers in analytical chemistry. **Analyst**. 2001;126(6):747-756.
126. Mogi I, Watanabe K. Enantioselective recognition of tartaric acid on magnetoelectrodeposited copper film electrodes. **Chemistry Letters**. 2012;41(11):1439-1441.
127. Petrie B, Barden R, Kasprzyk-Hordern B. A review on emerging contaminants in wastewaters and the environment: current knowledge, understudied areas and recommendations for future monitoring. **Water Research**. 2015;72:3-27.
128. Ma W, Kuang H, Xu L, Ding L, Xu C, Wang L, Kotov NA. Attomolar DNA detection with chiral nanorod assemblies. **Nature Communications**. 2013;4:2689.
129. Berova N, Bari LD, Pescitelli G. Application of electronic circular dichroism in configurational and conformational analysis of organic compounds. **Chemical Society Reviews**. 2007;36(6):914-931.
130. Blanco-López MC, Lobo-Castañón MJ, Miranda-Ordieres AJ, Tuñón-Blanco P. Voltammetric sensor for vanillylmandelic acid based on molecularly imprinted polymer-modified electrodes. **Biosensors and Bioelectronics**. 2003;18(4):353-362.
131. Arnaboldi S, Magni M, Mussini PR. Enantioselective selectors for chiral electrochemistry and electroanalysis: Stereogenic elements and enantioselection performance. **Current Opinion in Electrochemistry**. 2018;8:60-72.
132. Corey EJ, Helal CJ. Reduction of carbonyl compounds with chiral oxazaborolidine catalysts: A new paradigm for enantioselective catalysis and a powerful new synthetic method. **Angewandte Chemie International Edition**. 1998;37:1986-2012.
133. Sinou D. Asymmetric organometallic-catalyzed reactions in aqueous media. **Advanced Synthetis & Catalysis**. 2002;344:221-237.

134. Ramstrom O, Ansell RJ. Molecular imprinting technology: challenges and prospects for the future. **Chirality**. 1998;10:195-209.
135. Akiyama T, Itoh J, Fuchibe K. Recent progress in chiral brønsted acid catalysis. **Advanced Synthesis & Catalysis**. 2006;348(9):999-1010.
136. Giri R, Shi BF, Engle KM, Maugel N, Yu JQ. Transition metal-catalyzed C-H activation reactions: diastereoselectivity and enantioselectivity. **Chemical Society Reviews**. 2009;38(11):3242-3272.
137. Chen D, Wang Y, Klankermayer J. Enantioselective hydrogenation with chiral frustrated Lewis pairs. **Angewandte Chemie International Edition**. 2010;49(49):9475-9478.
138. Kempe M, Mosbach K. Separation of amino acids, peptides and proteins on molecularly imprinted stationary phases. **Journal of Chromatography A**. 1995;691:317-323.
139. Schweitz L, Andersson LI, Nilsson S. Capillary electrochromatography with predetermined selectivity obtained through molecular imprinting. **Analytical Chemistry**. 1997;69:1179-1183.
140. Ward TJ, Ward KD. Chiral separations: fundamental review 2010. **Analytical Chemistry**. 2010;82:4712-4722.
141. Banerjee-Ghosh K, Dor OB, Tassinari F, Capua E, Yochelis S, Capua A, Yang SH, Parkin SSP, Sarkar S, Kronik L, Baczewski T, Naaman, Paltiel Y. Separation of enantiomers by their enantiospecific interaction with achiral magnetic substrates. **Science**. 2018;360:1331-1334.
142. Hart HR, Rush DJ, Shea KJ. Discrimination between enantiomers of structurally related molecules: separation of benzodiazepines by molecularly imprinted polymers. **Journal of American Chemical Society**. 2000;122:460-465.
143. Maier NB, Franco P, Lindner W. Separation of enantiomers: needs, challenges, perspectives. **Journal of Chromatography A**. 2001;906:3-33.
144. Gübitz G, Schmid MG. Chiral separation by capillary electromigration techniques. **Journal of Chromatography A**. 2008;1204(2):140-156.
145. Zhang Z, Zhang X, Liu B, Liu J. Molecular imprinting on inorganic nanozymes for hundred-fold enzyme specificity. **Journal of American Chemical Society**. 2017;139(15):5412-5419.
146. Wattanakit C. Chiral metals as electrodes. **Current Opinion in Electrochemistry**. 2018;7:54-60.

147. Pachón LD, Yosef I, Markus TZ, Naaman R, Avnir D, Rothenberg G. Chiral imprinting of palladium with cinchona alkaloids. **Nature Chemistry**. 2009;1(2):160-164.
148. Pernites RB, Venkata SK, Tiu BD, Yago ACC, Advincula RC. Nanostructured, molecularly imprinted, and template-patterned polythiophenes for chiral sensing and differentiation. **Small**. 2012;8(11):1669-1674.
149. Attard G, Casadesus M, Macaskie LE, Deplanche K. Biosynthesis of platinum nanoparticles by *Escherichia coli* MC4100: can such nanoparticles exhibit intrinsic surface enantioselectivity? **Langmuir**. 2012;28(11):5267-5274.
150. Padmanaban M, Müller P, Lieder C, Gedrich K, Grönker R, Bon V, Senkovska I, Baumgärtner S, Opelt S, Paasch S, Brunner E, Glorius F, Klemm E, Kaskel. Application of a chiral metal-organic framework in enantioselective separation. **Chemical Communications**. 2011;47(44):12089-12091.
151. Mondal PC, Fontanesi C, Waldeck DH, Naaman R. Field and chirality effects on electrochemical charge transfer rates: spin dependent electrochemistry. **Chemical Society Reviews**. 2015;9:3377-3384.
152. Edmondson S, Osborne VL, Huck WT. Polymer brushes via surface-initiated polymerizations. **Chemical Society Reviews**. 2004;33(1):14-22.
153. Puoci F, Iemma F, Picci N. Stimuli-responsive molecularly imprinted polymers for drug delivery: a review. **Current Drug Delivery**. 2008;5:85-96.
154. Wulff G, Vesper W. Preparation of chromatography sorbents with chiral cavities for racemic resolution. **Journal of Chromatography A**. 1978;167:171-186.
155. Turiel E, Martin-Esteban A. Molecularly imprinted polymers: towards highly selective stationary phases in liquid chromatography and capillary electrophoresis. **Analytical Bioanalytical Chemistry**. 2004;378(8):1876-1886.
156. Maier NM, Lindner W. Chiral recognition applications of molecularly imprinted polymers: a critical review. **Analytical Bioanalytical Chemistry**. 2007;389(2):377-397.
157. Yin J, Yang G, Chen Y. Rapid and efficient chiral separation of nateglinide and its L-enantiomer on monolithic molecularly imprinted polymers. **Journal of Chromatography A**. 2005;1090(1-2):68-75.
158. Qu P, Lei J, Ouyang R, Ju H. Enantioseparation and amperometric detection of chiral compounds by in situ molecular imprinting on the microchannel wall. **Analytical Chemistry**. 2009;81(23):8651-8656.

159. Chen J, Liang RP, Wang XN, Qiu JD. A norepinephrine coated magnetic molecularly imprinted polymer for simultaneous multiple chiral recognition. **Journal of Chromatography A**. 2015;1409:268-276.
160. Lee WC, Cheng CH, Pan HH, Chung TH, Hwang CC. Chromatographic characterization of molecularly imprinted polymers. **Analytical Bioanalytical Chemistry**. 2008;390(4):1101-1109.
161. Chen L, Xu S, Li J. Recent advances in molecular imprinting technology: current status, challenges and highlighted applications. **Chemical Society Reviews**. 2011;40(5):2922-2942.
162. Dabrowski M, Cieplak M, Sharma PS, Borowicz P, Noworyta K, Lisowski W, D'Souza F, Kuhn A, Kutner W. Hierarchical templating in deposition of semi-covalently imprinted inverse opal polythiophene film for femtomolar determination of human serum albumin. **Biosensor and Bioelectronics**. 2017;94:155-161.
163. Dabrowski M, Cieplak M, Noworyta K, Heim M, Adamkiewicz W, Kuhn A, Sharma PS, Kutner W. Surface enhancement of a molecularly imprinted polymer film using sacrificial silica beads for increasing l-arabitol chemosensor sensitivity and detectability. **Journal of Materials Chemistry B**. 2017;5(31):6292-6299.
164. Lord GA, Gordon DB, Teiler LW, Carr CM. Electrochromatography-electrospray mass spectrometry of textile dyes. **Journal of Chromatography A**. 1995;700(1-2):27-33.
165. Gordon DB, Lord GA. Development of packed capillary column electrochromatography/mass spectrometry. **Rapid Communications in Mass Spectrometry**. 1994;8:544-548.
166. Yang L, Chen C, Liu X, Shi J, Wang G, Zhu L, Guo L, Glennon JD, Scully NM, Doherty BE. Use of cyclodextrin-modified gold nanoparticles for enantioseparations of drugs and amino acids based on pseudostationary phase-capillary electrochromatography. **Electrophoresis**. 2010;31(10):1697-1705.
167. Breadmore MC, Tubaon RM, Shallan AI, Phung SC, Abdul Keyon AS, Gstoettenmayr D, Prapatpong P, Alhusban AA, Ranjbar L, See HH, Dawod M, Quirino JP. Recent advances in enhancing the sensitivity of electrophoresis and

- electrochromatography in capillaries and microchips (2012-2014). **Electrophoresis**. 2015;36(1):36-61.
168. Castellani L, Flieger M, Sinibaldi M. Enantiomer separation of 2-arylpropionic acids on an ergot alkaloid-based stationary phase microbore column application. **Journal of Liquid Chromatography**. 1994;17(17):3695-3703.
 169. Yoshikawa M, Tharpa K, Dima ŞO. Molecularly imprinted membranes: past, present, and future. **Chemical Reviews**. 2016;116(19):11500-11528.
 170. Stinson SC. Chiral drugs. **Chemical & Engineering News Archive**. 1992;70(39):46-79.
 171. Takagishi T, Klotz IM. Macromolecule-small molecule interactions; introduction of additional binding sites in polyethyleneimine by disulfide cross-linkages. **Biopolymers**. 1972;11(2):483-491.
 172. Arshady R, Mosbach K. Synthesis of substrate-selective polymers by host-guest polymerization. **Die Makromolekulare Chemie**. 1981;182(2):687-692.
 173. Son SH, Jegal J. Chiral separation of D,L-serine racemate using a molecularly imprinted polymer composite membrane. **Journal of Applied Polymer Science**. 2007;104(3):1866-1872.
 174. Marchetti P, Solomon MFJ, Szekely G, Livingston AG. Molecular separation with organic solvent nanofiltration: a critical review. **Chemical Reviews**. 2014;114(21):10735-10806.
 175. Jiang H, Ma J, Li C. Mesoporous carbon incorporated metal oxide nanomaterials as supercapacitor electrodes. **Advanced Materials**. 2012;24(30):4197-4202.
 176. Abdi-Jalebi M, Dar MI, Sadhanala A, Senanayak SP, Giordano F, Zakeeruddin SM, Grätzel M, Friend RH. Impact of a mesoporous titania-perovskite interface on the performance of hybrid organic-inorganic perovskite solar cells. **The Journal of Physical Chemistry Letters**. 2016;7(16):3264-3269.
 177. Melvin AA, Illath K, Das T, Raja T, Bhattacharyya S, Gopinath CS. M-Au/TiO₂ (M = Ag, Pd, and Pt) nanophotocatalyst for overall solar water splitting: role of interfaces. **Nanoscale**. 2015;7(32):13477-13488.
 178. Nyein HYY, Gao W, Shahpar Z, Emaminejad S, Challa S, Chen K, Fahad HM, Tai LC, Ota H, Davis RW, Javey A. A Wearable electrochemical platform for noninvasive simultaneous monitoring of Ca²⁺ and pH. **ACS Nano**. 2016;10(7):7216-7224.

179. Mishra RK, Hubble LJ, Martín A, Kumar R, Barfidokht A, Kim J, Musameh MM, Kyratzis IL, Wang J. Wearable flexible and stretchable glove biosensor for on-site detection of organophosphorus chemical threats. **ACS Sensors**. 2017;2(4):553-561.
180. Ma Z, Chen P, Cheng W, Yan K, Pan L, Shi Y, Yu G. Highly sensitive, printable nanostructured conductive polymer wireless sensor for food Spoilage detection. **Nano Letters**. 2018;18(7):4570-4575.
181. Zhu R, Desroches M, Yoon B, Swager TM. Wireless oxygen sensors enabled by Fe(II)-polymer wrapped carbon nanotubes. **ACS Sensors**. 2017;2(7):1044-1050.
182. Paxton WF, Baker PT, Kline TR, Wang Y, Mallouk TE, Sen A. Catalytically induced electrokinetics for motors and micropumps. **Journal of the American Chemical Society**. 2006;128(46):14881-14888.
183. Loget G, Zigah D, Bouffier L, Sojic N, Kuhn A. Bipolar electrochemistry: from materials science to motion and beyond. **Accounts of Chemical Research**. 2013;46(11):2513-2523.
184. Loget G, Kuhn A. Propulsion of microobjects by dynamic bipolar self-regeneration. **Journal of the American Chemical Society**. 2010;132(45):15918-15919.
185. Loget G, Roche J, Gianessi E, Bouffier L, Kuhn A. Indirect Bipolar electrodeposition. **Journal of the American Chemical Society**. 2012;134(49):20033-20036.
186. Malytska I, Doneux T, Bougouma M, Kuhn A, Bouffier L. Wireless addressing of freestanding MoSe₂ macro- and microparticles by bipolar electrochemistry. **The Journal of Physical Chemistry C**. 2019;123(9):5647-5652.
187. Inagi S, Ishiguro Y, Atobe M, Fuchigami T. Bipolar patterning of conducting polymers by electrochemical doping and reaction. **Angewandte Chemie International Edition**. 2010;49(52):10136-10139.
188. Ishiguro Y, Inagi S, Fuchigami T. Site-controlled application of electric potential on a conducting polymer "Canvas". **Journal of the American Chemical Society**. 2012;134(9):4034-4036.
189. Zhang L, Gupta B, Goudeau B, Mano N, Kuhn A. Wireless electromechanical readout of chemical information. **Journal of the American Chemical Society**. 2018;140(45):15501-15506.

190. Parmar J, Vilela D, Villa K, Wang J, Sánchez S. Micro- and nanomotors as active environmental microcleaners and sensors. **Journal of the American Chemical Society**. 2018;140(30):9317-9331.
191. Jacobson GA, Raidal S, Robson K, Narkowicz CK, Nichols DS, Walters EH. Bronchopulmonary pharmacokinetics of (R)-salbutamol and (S)-salbutamol enantiomers in pulmonary epithelial lining fluid and lung tissue of horses. **British Journal of Clinical Pharmacology**. 2017;83(7):1436-1445.
192. Larcher D, Tarascon JM. Towards greener and more sustainable batteries for electrical energy storage. **Nature Chemistry**. 2015;7(1):19-29.
193. Polshettiwar V, Varma RS. Green chemistry by nano-catalysis. **Green Chemistry**. 2010;12(5):743-754.
194. Su DS, Zhang J, Frank B, Thomas A, Wang X, Paraknowitsch J, Schlögl R. Metal-free heterogeneous catalysis for sustainable chemistry. **ChemSusChem**. 2010;3(2):169-180.
195. Chu S, Majumdar A. Opportunities and challenges for a sustainable energy future. **Nature**. 2012;488:294-303.
196. Liu J, Liu Y, Liu N, Han Y, Zhang XH, H., Lifshitz Y, Lee ST, Zhong J, Kang Z. Metal-free efficient photocatalyst for stable visible water splitting via a two-electron pathway. **Science**. 2015;347:970-974.
197. Liang Y, Li Y, Wang H, Dai H. Strongly coupled inorganic/nanocarbon hybrid materials for advanced electrocatalysis. **Journal of American Chemical Society**. 2013;135(6):2013-2036.
198. Wang Z, Li C, Domen K. Recent developments in heterogeneous photocatalysts for solar-driven overall water splitting. **Chemical Society Reviews**. 2019;48(7):2109-2125.
199. Ding C, Shi J, Wang Z, Li C. Photoelectrocatalytic water splitting: significance of cocatalysts, electrolyte, and interfaces. **ACS Catalysis**. 2016;7(1):675-688.
200. Kim JH, Jang JW, Jo YH, Abdi FF, Lee YH, van de Krol R, et al. Hetero-type dual photoanodes for unbiased solar water splitting with extended light harvesting. **Nature Communications**. 2016;7:13380.
201. Zhang X, Zhang X, Xu H, Wu Z, Wang H, Liang Y. Iron-doped cobalt monophosphide nanosheet/carbon nanotube hybrids as active and stable electrocatalysts for water splitting. **Advanced Functional Materials**. 2017;27(24):1606635.

202. McCrory CC, Jung S, Ferrer IM, Chatman SM, Peters JC, Jaramillo TF. Benchmarking hydrogen evolving reaction and oxygen evolving reaction electrocatalysts for solar water splitting devices. **Journal of the American Chemical Society**. 2015;137(13):4347-4357.
203. Lu X, Zhao C. Electrodeposition of hierarchically structured three-dimensional nickel-iron electrodes for efficient oxygen evolution at high current densities. **Nature Communications**. 2015;6:6616.
204. Hoang TTH, Gewirth AA. High activity oxygen evolution reaction catalysts from additive-controlled electrodeposited Ni and NiFe films. **ACS Catalysis**. 2016;6(2):1159-1164.
205. McCrory CC, Jung S, Peters JC, Jaramillo TF. Benchmarking heterogeneous electrocatalysts for the oxygen evolution reaction. **Journal of the American Chemical Society**. 2013;135(45):16977-16987.
206. Lee Y, Suntivich J, May KJ, Perry EE, Shao-Horn Y. Synthesis and activities of rutile IrO₂ and RuO₂ nanoparticles for oxygen evolution in acid and alkaline solutions. **Journal of Physical Chemistry Letters**. 2012;3(3):399-404.
207. Reier T, Oezaslan M, Strasser P. Electrocatalytic Oxygen Evolution Reaction (OER) on Ru, Ir, and Pt Catalysts: A Comparative Study of Nanoparticles and Bulk Materials. **ACS Catalysis**. 2012;2(8):1765-1772.
208. Kötz R, Stucki S, Scherson D, Kolb DM. In-situ identification of RuO₄, as the corrosion product during oxygen evolution on ruthenium in acid media. **Journal of Electroanalytical Chemistry and Interfacial Electrochemistry**. 1984;172:211-219.
209. Cherevko S, Geiger S, Kasian O, Kulyk N, Grote J-P, Savan A, Shrestha BR, Merzlikin S, Breitbach B, Ludwig A, Mayrhofer KJJ. Oxygen and hydrogen evolution reactions on Ru, RuO₂, Ir, and IrO₂ thin film electrodes in acidic and alkaline electrolytes: A comparative study on activity and stability. **Catalysis Today**. 2016;262:170-180.
210. Roger I, Shipman MA, Symes MD. Earth-abundant catalysts for electrochemical and photoelectrochemical water splitting. **Nature Reviews Chemistry**. 2017;1(1):0003.
211. Wang X, Li W, Xiong D, Liu L. Fast fabrication of self-supported porous nickel phosphide foam for efficient, durable oxygen evolution and overall water splitting. **Journal of Materials Chemistry A**. 2016;4(15):5639-5646.

212. Tang C, Cheng N, Pu Z, Xing W, Sun X. NiSe nanowire film supported on nickel foam: an efficient and stable 3D bifunctional electrode for full water splitting. **Angewandte Chemie International Edition**. 2015;54(32):9351-9355.
213. Wu L-K, Wu W-Y, Xia J, Cao H-Z, Hou G-Y, Tang Y-P, Zheng G-Q. A nanostructured nickel–cobalt alloy with an oxide layer for an efficient oxygen evolution reaction. **Journal of Materials Chemistry A**. 2017;5(21):10669-10677.
214. Chen L, Guo H, Fujita T, Hirata A, Zhang W, Inoue A, Chen M. Nanoporous PdNi bimetallic catalyst with enhanced electrocatalytic performances for electro-oxidation and oxygen reduction reactions. **Advanced Functional Materials**. 2011;21(22):4364-4370.
215. Shalom M, Ressnig D, Yang X, Clavel G, Feller TP, Antonietti M. Nickel nitride as an efficient electrocatalyst for water splitting. **Journal of Materials Chemistry A**. 2015;3(15):8171-8177.
216. Dong T, Zhang X, Wang P, Chen H-S, Yang P. Hierarchical nickel-cobalt phosphide hollow spheres embedded in P-doped reduced graphene oxide towards superior electrochemistry activity. **Carbon**. 2019;149:222-233.
217. Chang J, Li K, Wu Z, Ge J, Liu C, Xing W. Sulfur-doped nickel phosphide nanoplates arrays: a monolithic electrocatalyst for efficient hydrogen evolution reactions. **ACS Applied Materials & Interfaces**. 2018;10(31):26303-26311.
218. Sun H, Xu X, Yan Z, Chen X, Cheng F, Weiss PS, Chen J. Porous multishelled Ni₂P hollow microspheres as an active electrocatalyst for hydrogen and oxygen evolution. **Chemistry of Materials**. 2017;29(19):8539-8547.
219. Swesi AT, Masud J, Nath M. Nickel selenide as a high-efficiency catalyst for oxygen evolution reaction. **Energy & Environmental Science**. 2016;9(5):1771-1782.
220. Sivanantham A, Shanmugam S. Nickel selenide supported on nickel foam as an efficient and durable non-precious electrocatalyst for the alkaline water electrolysis. **Applied Catalysis B: Environmental**. 2017;203:485-493.
221. Tian T, Gao H, Zhou X, Zheng L, Wu J, Li K, Ding Y. Study of the active sites in porous nickel oxide nanosheets by manganese modulation for enhanced oxygen evolution catalysis. **ACS Energy Letters**. 2018;3(9):2150-2158.

222. Arciga-Duran E, Meas Y, Pérez-Bueno JJ, Ballesteros JC, Trejo G. Effect of oxygen vacancies in electrodeposited NiO towards the oxygen evolution reaction: Role of Ni-Glycine complexes. **Electrochimica Acta**. 2018;268:49-58.
223. Dong T, Zhang X, Li M, Wang P, Yang P. Hierarchical flower-like Ni–Co layered double hydroxide nanostructures: synthesis and super performance. **Inorganic Chemistry Frontiers**. 2018;5(12):3033-3041.
224. Vij V, Sultan S, Harzandi AM, Meena A, Tiwari JN, Lee WG, Yoon T, Kim KS. Nickel-based electrocatalysts for energy-related applications: oxygen reduction, oxygen evolution, and hydrogen evolution reactions. **ACS Catalysis**. 2017;7(10):7196-7225.
225. Hercule KM, Wei Q, Khan AM, Zhao Y, Tian X, Mai L. Synergistic effect of hierarchical nanostructured MoO₂/Co(OH)₂ with largely enhanced pseudocapacitor cyclability. **Nano Letters**. 2013;13(11):5685-5691.
226. Du G, Bian Q, Zhang J, Yang X. Facile fabrication of hierarchical porous carbon for a high-performance electrochemical capacitor. **RSC Advances**. 2017;7(73):46329-46335.
227. Szamocki R, Reculosa S, Ravaine S, Bartlett PN, Kuhn A, Hempelmann R. Tailored mesostructuring and biofunctionalization of gold for increased electroactivity. **Angewandte Chemie International Edition**. 2006;45(8):1317-1321.
228. Guldi DM, Zilbermann I, Anderson GA, Kordatos K, Prato M, Tafuro R, Valli L. Langmuir–Blodgett and layer-by-layer films of photoactive fullerene–porphyrin dyads. **Journal Materials Chemistry**. 2004;14(3):303-309.
229. Li X, Zhang G, Bai X, Sun X, Wang X, Wang E, Dai H. Highly conducting graphene sheets and Langmuir-Blodgett films. **Nature Nanotechnology**. 2008;3(9):538-542.
230. Szamocki R, Velichko A, Holzapfel C, Mücklich F, Ravaine S, Garrigue P, Sojic N, Hempelmann R, Kuhn A. Macroporous ultramicroelectrodes for improved electroanalytical measurements. **Analytical Chemistry** 2007;79(2):533-539.
231. Tiede B. Langmuir-Blodgett Membranes for Separation and Sensing. **AdvanceMaterials**. 1991;3(11):532-541.
232. Lenz J, Trieu V, Kuhn A, Hempelmann R. Macroporous ruthenium oxide electrodes for electrochemical application. **ECS Transactions**. 2011;33(32):19-25.

233. Kim MS, Ma L, Choudhury S, Moganty SS, Wei S, Archer LA. Fabricating multifunctional nanoparticle membranes by a fast layer-by-layer Langmuir–Blodgett process: application in lithium–sulfur batteries. **Journal of Materials Chemistry A**. 2016;4(38):14709-14719.
234. Choi KS, Lichtenegger HC, Stucky GD, McFarland EW. Electrochemical synthesis of nanostructured ZnO films utilizing self-assembly of surfactant molecules at solid-liquid interfaces. **Journal of the American Chemical Society**. 2002;124(42):12402-12403.
235. Walcarius A, Sibottier E, Etienne M, Ghanbaja J. Electrochemically assisted self-assembly of mesoporous silica thin films. **Nature Materials**. 2007;6(8):602-608.
236. Burgess I, Jeffrey CA, Cai X, Szymanski G, Galus Z, Lipkowski J. Direct visualization of the potential-controlled transformation of hemimicellar aggregates of dodecyl Sulfate into a condensed monolayer at the Au(111) electrode surface. **Langmuir**. 1999;15(8):2607–2616;.
237. Kobayashi N, Saitoh H, Kawamura R, Yoshikawa HY, Nakabayashi S. Structural change of nonionic surfactant self-assembling at electrochemically controlled HOPG/electrolyte interface. **Journal of Electroanalytical Chemistry**. 2017;799:444-450.
238. Pérez-Ramírez J, Christensen CH, Egeblad K, Christensen CH, Groen JC. Hierarchical zeolites: enhanced utilisation of microporous crystals in catalysis by advances in materials design. **Chemical Society Reviews**. 2008;37(11):2530-2542.
239. Li Y, Fu ZY, Su BL. Hierarchically structured porous materials for energy conversion and storage. **Advanced Functional Materials**. 2012;22(22):4634-4667.
240. Pavasupree S, Ngamsinlapasathian S, Suzuki Y, Yoshikawa S. Preparation and characterization of high surface area nanosheet titania with mesoporous structure. **Materials Letters**. 2007;61(14-15):2973-2977.
241. Burgess I, Jeffrey CA, Cai X, Szymanski G, Galus Z, Lipkowski J. Direct visualization of the potential-controlled transformation of hemimicellar aggregates of dodecyl Sulfate into a condensed monolayer at the Au(111) electrode surface. **Langmuir**. 1999;15(8):2607-2616.

242. Liang HW, Wei W, Wu ZS, Feng X, Müllen K. Mesoporous metal-nitrogen-doped carbon electrocatalysts for highly efficient oxygen reduction reaction. **Journal of the American Chemical Society**. 2013;135(43):16002-16005.
243. Sharma AK, Desnavi S, Dixit C, Varshney U, Sharma A. Extraction of nickel nanoparticles from electroplating waste and their application in production of bio-diesel from biowaste. **International Journal of Chemical Engineering and Applications**. 2015;6(3):156-159.
244. Yan H, Zhang D, Xu J, Lu Y, Qiu K, Zhang Y, Luo Y. Solution growth of NiO nanosheets supported on Ni foam as high-performance electrodes for supercapacitors. **Nanoscale Research Letters** 2014;9(1):424.
245. Fang YH, Liu ZP. Mechanism and Tafel Lines of Electro-Oxidation of Water to Oxygen on RuO₂(110). **Journal of the American Chemical Society**. 2010;132:18214-18222.
246. Tientong J, Garcia S, Thurber CR, Golden TD. Synthesis of nickel and nickel Hydroxide nanopowders by simplified chemical reduction. **Journal of Nanotechnology**. 2014;2014:1-6.
247. Kauffman DR, Alfonso D, Tafen DN, Lekse J, Wang C, Deng X, Lee J, Jang H, Lee JS, Kumar S, Matranga C. Electrocatalytic oxygen evolution with an atomically precise nickel catalyst. **ACS Catalysis**. 2016;6(2):1225-1234.
248. Juodkazis K, Juodkazytė J, Vilkauskaitė R, Jasulaitienė V. Nickel surface anodic oxidation and electrocatalysis of oxygen evolution. **Journal of Solid State Electrochemistry**. 2008;12(11):1469-1479.
249. Stern LA, Hu X. Enhanced oxygen evolution activity by NiOx and Ni(OH)₂ nanoparticles. **Faraday Discussions**. 2014;176:363-379.
250. Łukaszewski M, Soszko M, Czerwiński A. Electrochemical methods of real surface area determination of noble metal electrodes – an overview. **International Journal of Electrochemical Science**. 2016:4442-4469.
251. Castro EB, Gervasi CA. Electrodeposited Ni–Co-oxide electrodes: characterization and kinetics of the oxygen evolution reaction. **International Journal of Hydrogen Energy**. 2000;25(12):1163-1170.
252. Le TD, Zhang L, Reculosa S, Vignoles G, Mano N, Kuhn A, Laseux D. Optimal thickness of a porous micro-electrode operating a single redox reaction. **ChemElectroChem** 2019;6(1):173-180.

253. Le TD, Lasseux D, Nguyen XP, Vignoles G, Mano N, Kuhn A. Multi-scale modeling of diffusion and electrochemical reactions in porous micro-electrodes. **Chemical Engineering Science**. 2017;173:153-167.
254. Assavapanumat S, Ketkaew M, Garrigue P, Lapeyre V, Reculosa S, Wattanakit C, Kuhn A. Hierarchical multiporous nickel for oxygen evolution reaction in alkaline media. **ChemCatChem**. 2019;11(24):5951-5960.

Author's biography

Name:	Sunpet Assavapanumat
Date of birth:	February 25 th 1993
Place of birth:	Bangkok, Thailand
Current address:	320/83, Klong Song Ton Noon, Ladkrabang, Bangkok, 10520
Education:	Bachelor's Degree in Chemistry, Kasetsart University, Bangkok, Thailand (201-2014)
Scholarship:	<ul style="list-style-type: none">-Recipient of the full scholarship from Vidyasirimedhi Institute of Science and Technology (VISTEC)-Recipient of the Franco-Thai scholarship from France embassy.
Academic publication:	<p>Assavapanumat S, Ketkaew M, Kuhn A, Wattanakit C. Synthesis, Characterization, and Electrochemical Applications of Chiral Imprinted Mesoporous Ni Surfaces. <i>Journal of the American Chemical Society</i>. 2019; 141: 18870-18876.</p> <p>Assavapanumat S, Ketkaew M, Garrigue P, Lapeyre V, Reculosa S, Wattanakit C, Kuhn A. Hierarchical Multiporous Nickel for Oxygen Evolution Reaction in Alkaline Media. <i>ChemCatChem</i>. 2019; 11: 1-11.</p> <p>Assavapanumat S, Gupta B, Salinas, G, Goudeau B, Wattanakit C, Kuhn A. Chiral Platinum–Polypyrrole Hybrid Films as Efficient Enantioselective Actuators. <i>Chemical Communications</i>, 2019; 55: 10956-10959.</p> <p>Assavapanumat S, Yutthalekha T, Garrigue P, Goudeau B, Lapeyre V, Perro A, Sojic N, Wattanakit C, Kuhn A. Potential-Induced Fine Tuning of the Enantioaffinity of Chiral Metal</p>

Phases. *Angewandte Chemie International Edition*, 2019; 58: 3471-3475.

Wattanakit C, Yutthalekha T, Assavapanumat S, Lapeyre V, Kuhn A. Pulsed Electroconversion for highly selective enantiomer synthesis. *Nature Communications*, 2017; 18: 2087.

Rodponthukwaji K, Wattanakit C, Yutthalekha T, Assavapanumat S, Warakulwit C, Wannapakdee W, Limtrakul J. Catalytic upgrading of carboxylic acids as bio-oil models over hierarchical ZSM-5 obtained via an organosilane approach. *RSC Advances*, 2017; 7: 35581.